HIGH-FREQUENCY OSCILLATIONS IN GRAPHENE RESONANT TUNNELLING HETEROSTRUCTURES

JENNIFER GASKELL, MSci.(Hons)

Thesis submitted to the University of Nottingham
for the degree of Doctor of Philosophy

JULY 2016

Abstract

In this thesis, the form of the current-voltage characteristics and the resulting current oscillations in graphene-hexagonal boron nitride heterostructures are explored by means of theoretical investigation and are supported by experimental observations. The conditions for resonant tunnelling and the effect of device and circuit parameters are examined through simulation of the charge dynamics using the Bardeen Transfer Hamiltonian method. Studies of the effect of induced moiré patterns between the crystallographically aligned graphene and the boron nitride lattices are also undertaken, with recommendations for future investigation. It is theoretically shown that samples containing two layers of graphene, separated by hexagonal boron nitride tunnel barriers, produced higher frequency oscillations when the graphene lattices are aligned. This was found to be due to the decrease in wavefunction overlap in the misaligned samples, which is not compensated by the higher density of states available for tunnelling. Chemical doping of the graphene layers are also found to increase the frequency, as it allows the Dirac cones to be brought into alignment for resonant tunnelling with a higher number of states available. It is known that the mismatch in lattice constant between the graphene lattice and the hexagonal boron nitride lattice creates a moiré pattern. This, in turn, induces additional Dirac points in the band structure and thus leads to new features in the current-voltage characteristics. The theoretical simulations presented in this thesis are substantiated by recently-published experimental results, and provide insight into possible future high-frequency, room-temperature solid state oscillators and amplifiers. In conclusion, the mechanisms for resonant tunnelling in multiple graphene heterostructures are identified and demonstrated in this work, and provide promising evidence for novel high frequency technologies and further research.

It doesn't matter whether you're a lion or a gazelle, when the sun comes up, you'd better be running - Sir Roger Bannister

A million thanks to my three wise supervisors - it has been a complete pleasure to work you on such exciting projects built upon your own PhD work. Professor Mark Fromhold, Big Chief, thanks for sharing your knowledge on so many areas of physics and beyond, and for your love of the beauty of science. Professor Laurence Eaves, thanks for your never-ending enthusiasm, direct advice and humour. Dr Mark Greenaway, thanks for everything - from sharing your skills and answering all of my questions to being an awesome mate.

Thanks to all of my ultra-running friends who quizzed me on quantum physics through long nights across the mountains, always reigniting my enthusiasm for science along the way. Thanks to Montane for supporting my adventures away from physics throughout my PhD. Thanks to the squash club for all the great games. And so many thanks to my amazing office mates, tea room friends and encouraging family.

Publications

- Graphene-hexagonal boron nitride resonant tunneling diodes as high-frequency oscillators. J. Gaskell, L. Eaves, K. S. Novoselov, A. Mishchenko, A. K. Geim, T. M. Fromhold, and M. T. Greenaway *Appl. Phys. Lett.* **107**, 103105 (2015).

- Moiré effects on conduction in graphene resonant tunnelling heterostructures. J. Gaskell, L. Eaves, T. M. Fromhold, and M. T. Greenaway (in preparation).

Conferences

- Graphene Week 2014, Gothenburg, Sweden (poster presentation).

- UK Semiconductors 2015, Sheffield, UK (oral presentation).

- EP2DS 2015, Sendai, Japan (poster presented by M. Greenaway).

- Edison 2015, Salamanca, Spain (poster presented by L. Eaves).

- APS March Meeting 2016 (oral presentation by M. Greenaway).

Contents

Chapter 1

Resonant Tunnelling and Graphene Heterostructures

1.1 Introduction

Resonant tunnelling is a quantum mechanical process that has long attracted both scientific and technological attention owing to its intriguing and fundamental underlying physics and potential applications for high-speed electronics. The materials systems exhibiting resonant tunnelling, however, have been largely limited to conventional semiconductors such as GaAs, partially due to their excellent crystalline quality [1, 2] and high mobility. In recent years, there has been an explosion of research using the novel two-dimensional (2D) material graphene [3], as it potentially has even higher mobility. The work presented in this thesis explores how graphene's excellent electrical properties can be harnessed in novel graphene-based van der Waals heterostructures that exhibit resonant tunnelling. The resulting current-voltage characteristics and high-frequency operation in these devices are explored, leading to a discussion of potential new device designs. This introductory chapter provides an outline of the previous contributions to the field of both III-V semiconducting tunnel devices and graphene research, starting with a general description of quantum mechanical tunnelling and leading to the introduction of the graphene heterostructure device discussed in this thesis.

1.2 Quantum Tunnelling

The graphene-based devices considered in this thesis will harness the effect of resonant quantum-mechanical tunnelling through a boron nitride potential barrier. Here, a short outline to quantum tunnelling is given, followed by an explanation of resonant conditions.

Classically, if a particle, such as an electron, with energy E is incident on a potential barrier of any thickness with energy $E < E_B$, the electron cannot pass and is thus reflected. If $E > E_B$, the electron will pass over the barrier, resulting in current. Both cases are schematically shown in Fig. 1.1(a). Quantum mechanically, the result is practically equivalent to the classical case for a wide tunnel barrier, as the wavefunction (the probability distribution function) of the electron will decay before leaving the barrier, and thus there is a very low probability of tunnelling. However, if the barrier is thin enough, it is possible that an electron with $E < E_B$ can undergo quantum tunnelling through it, as seen in Fig. 1.1(b). This is a result of the wave-like nature of the electrons, as the wavefunction and its derivative must be continuous at the barrier boundary, so there is a finite probability of finding the electron on either side of the boundary [4]. Such a potential barrier can be formed by sandwiching an insulator, with large enough band gap, between two metal regions, as seen in Fig.1.1(c).

1.2.1 Reflection and Transmission Coefficients

The probability of tunnelling can be calculated by considering the simple example of a plane wave incident on a barrier. Taking the potential barrier to be of height, V_0, as seen in Fig.1.2, where the wavefunction is plotted for an electron of $E > V_0$, the wavefunction in each region can be written as:

$$\psi_A(x) = A_R e^{ik_0 x} + A_L e^{-ik_0 x}, \qquad (x < 0) \tag{1.1}$$

$$\psi_B(x) = B_R e^{ik_1 x} + B_L e^{-ik_1 x}, \qquad (0 < x < a) \tag{1.2}$$

$$\psi_C(x) = C_R e^{ik_0 x} + C_L e^{-ik_0 x}. \qquad (x > a) \tag{1.3}$$

Here, $A_{R,L}, B_{R,L}$ and $C_{R,L}$ are coefficents of the waves in the corresponding regions, $A - C$, and R and L represent the direction of travel, right and

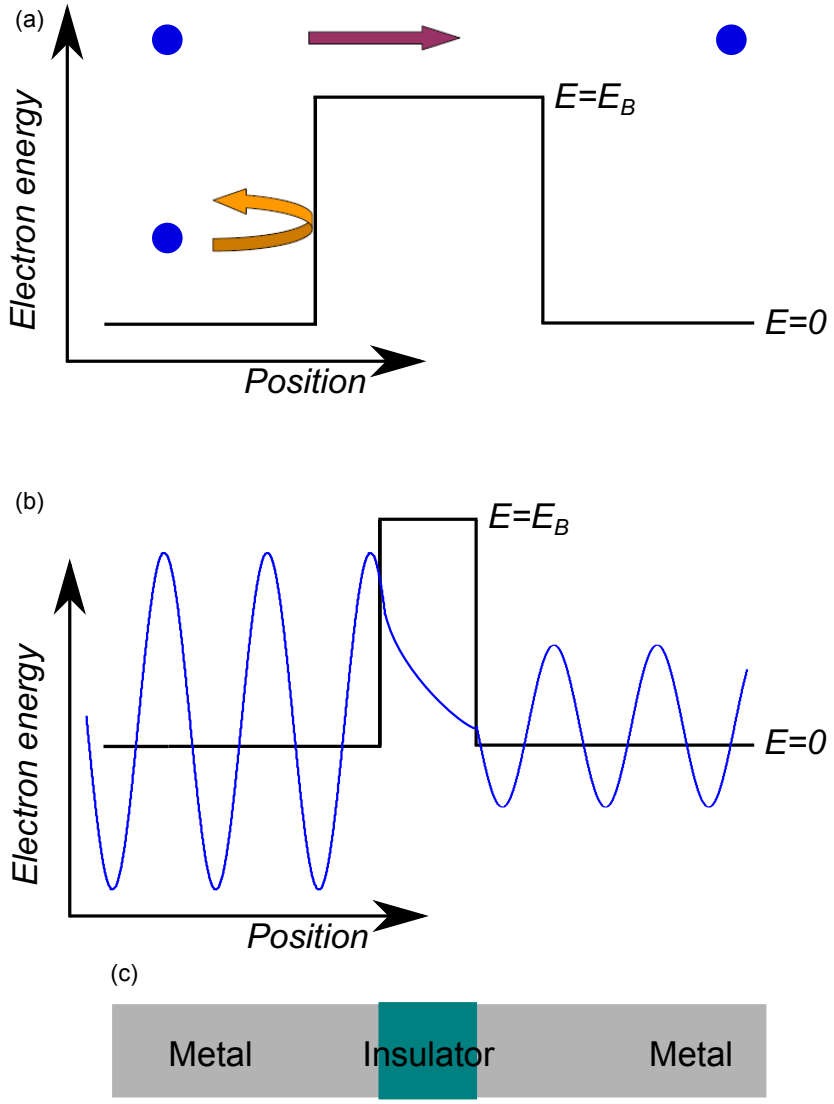

Figure 1.1: (a) Classically, electrons with $E > E_B$ can pass over a thick barrier and any electrons with $E < E_B$ will be reflected. (b) Quantum mechanically, electrons with $E > E_B$ can pass over a thin barrier and electrons with $E < E_B$ will be either be reflected or undergo tunnelling through the barrier. (c) Schematic layer diagram of a metal-insulator-metal tunnel device.

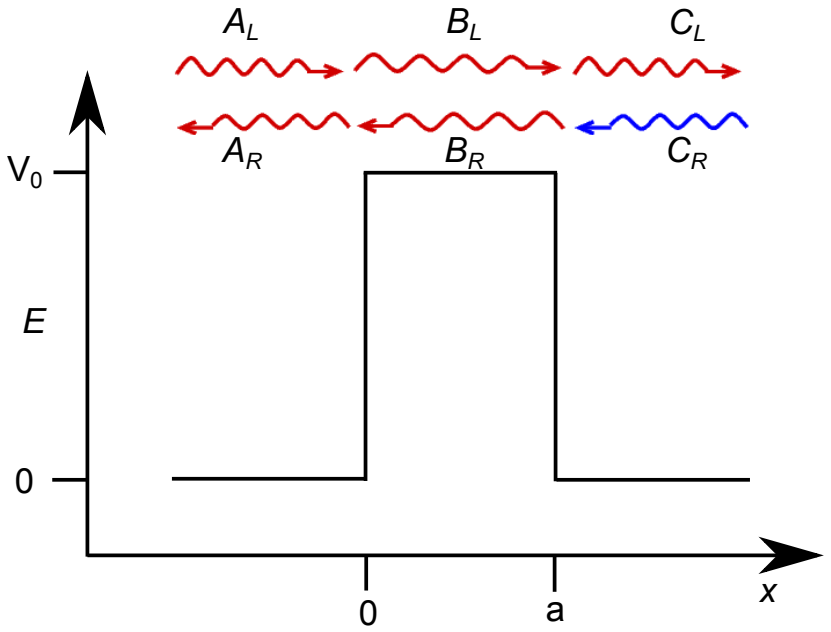

Figure 1.2: Plane waves on the left and right (L and R, in regions A and C, respectively) of the barrier, in region B, for $E > V_0$. Note the wavelength is longer in the barrier region due to the change in potential. For $E < V_0$, the wavefunction will be evanescent in the barrier.

left, respectively. From the time-independent Schrödinger equation,

$$H\psi(x) = \left[-\frac{\hbar^2}{2m}\frac{d^2}{dx^2} + V(x)\right]\psi(x) = E\psi(x), \tag{1.4}$$

the wavenumbers in each region can be calculated to be

$$k_0 = \sqrt{\frac{2mE}{\hbar^2}}, \qquad (x < 0 \text{ or } x > a) \tag{1.5}$$

$$k_1 = \sqrt{\frac{2m(E - V_0)}{\hbar^2}}. \qquad (0 < x < a) \tag{1.6}$$

The boundary conditions at the barrier edges ($x = 0$ and $x = a$) require the wavefunction and its derivative to be continuous, which gives

$$A_R + A_L = B_R + B_L, \tag{1.7}$$

$$ik_0(A_R - A_L) = ik_1(B_R - B_L), \tag{1.8}$$

$$B_R e^{iak_1} + B_L e^{-iak_1} = C_R e^{iak_0} + C_L e^{-iak_0}, \tag{1.9}$$

$$ik_1(B_R e^{iak_1} - B_L e^{-iak_1}) = ik_0(C_R e^{iak_0} - C_L e^{-iak_0}). \tag{1.10}$$

As the plane wave in this example is incident from the left, some coef-

ficients are known, such as $A_R = 1$ (incoming electron), $A_L = r$ (reflected part), $C_R = t$ (transmitted part), $C_L = 0$ (no incoming electron from the right). It is therefore possible to solve Eq.(1.10) for r and t, which gives:

$$t = \frac{4k_0k_1e^{-ia(k_0-k_1)}}{(k_0+k_1)^2 - e^{2iak_1}(k_0-k_1)^2}, \tag{1.11}$$

$$r = \frac{(k_0^2-k_1^2)\sin(ak_1)}{2ik_0k_1\cos(ak_1) + (k_0^2+k_1^2)\sin(ak_1)}. \tag{1.12}$$

The tunnelling probability, T, is simply $|t|^2$. For an electron of $E > V_0$, the probability of tunnelling is

$$T = \frac{1}{1 + \frac{V_0^2\sin^2(k_1a)}{4E(E-V_0)}}. \tag{1.13}$$

This can give a non-unity probability, and as the reflection probability is

$$R = |r|^2 = 1 - T, \tag{1.14}$$

we get an interesting result in that the electron with an energy above that of the barrier may still be reflected! As $E >> V$, this result converges to the classical result of $R = 0$.

For $E < V_0$, the solution in the barrier ($0 < x < a$) will be evanescent, i.e.

$$\psi_B(x) = B_Re^{\kappa x} + B_Le^{-\kappa x}. \tag{1.15}$$

This gives

$$T = \frac{1}{1 + \frac{V_0^2\sinh^2(k_1a)}{4E(V_0-E)}}, \tag{1.16}$$

which indicates a non-zero probability, and thus predicts the occurrence of quantum tunnelling.

1.2.2 Scattering-Assisted Tunnelling

In semiconducting tunnel devices, electrons tunnelling between energetic states in different layers will conserve energy and momentum in a process known as *direct tunnelling*. It is also possible for tunnelling to occur alongside electron scattering events, leading to *scattering-assisted tunnelling*. This is a

very common transport process, as there will always be some imperfections in semiconductor crystals used in tunnel diodes, such as impurities or deformations in the lattice structure, which lead to scattering events. There are two types of scattering process; *elastic* and *inelastic*. During elastic scattering, the energy of the electron is conserved, but the momentum of the electron is not. For example, when an electron collides with a defect in a lattice, the translational symmetry in $x - y$ is broken and thus k_x/k_y is not conserved. Inelastic scattering does not conserve the energy or the momentum of the electron. Most inelastic scattering processes arise from electron-phonon interactions, such as absorption (if the tempertaure is high enough), or emission of a phonon. We will later observe electron-phonon interactions are not a main contributor to the tunnelling events in the devices discussed in this thesis, due to the high energy of the phonons. The modelling of elastic scattering in graphene resonant tunnelling diodes will be discussed further in Chapters 2 and 3.

1.3 Tunnelling in Semiconductor Devices

In semiconductor devices, tunnelling has been exploited since the late 1950s [5]. The discovery of the Esaki semiconducting diode in 1957 [6] focused attention on the possibility of exploiting the resulting negative differential conductance (NDC), a phenomenon that leads to a decrease in current as the voltage is increased, for the generation of high-frequency electromagnetic waves. An example of the current-voltage (*I(V)*) characteristics of this device is shown in Fig. 1.3(a), with the NDC region highlighted (yellow). Following Esaki's pioneering work, transferred electron diodes [7–9] based on n-type GaAs and InP were successfully developed as microwave generators. Semiconductor superlattices [10, 11] and double-barrier resonant tunnelling diodes (DBRTDs) [12, 13] also exhibit strong NDC in their device characteristics and, recently, DBRTDs operating at frequencies of 1.04 THz and with output powers of up to 10 μW have been reported [14]. Here, we review the basic principles behind these devices.

1.3.1 Operation of Tunnel Diodes

The simplest tunnel diode is constructed of two oppositely-doped semiconductors to form an Esaki $p - n$ junction. The p-type semiconductor (left)

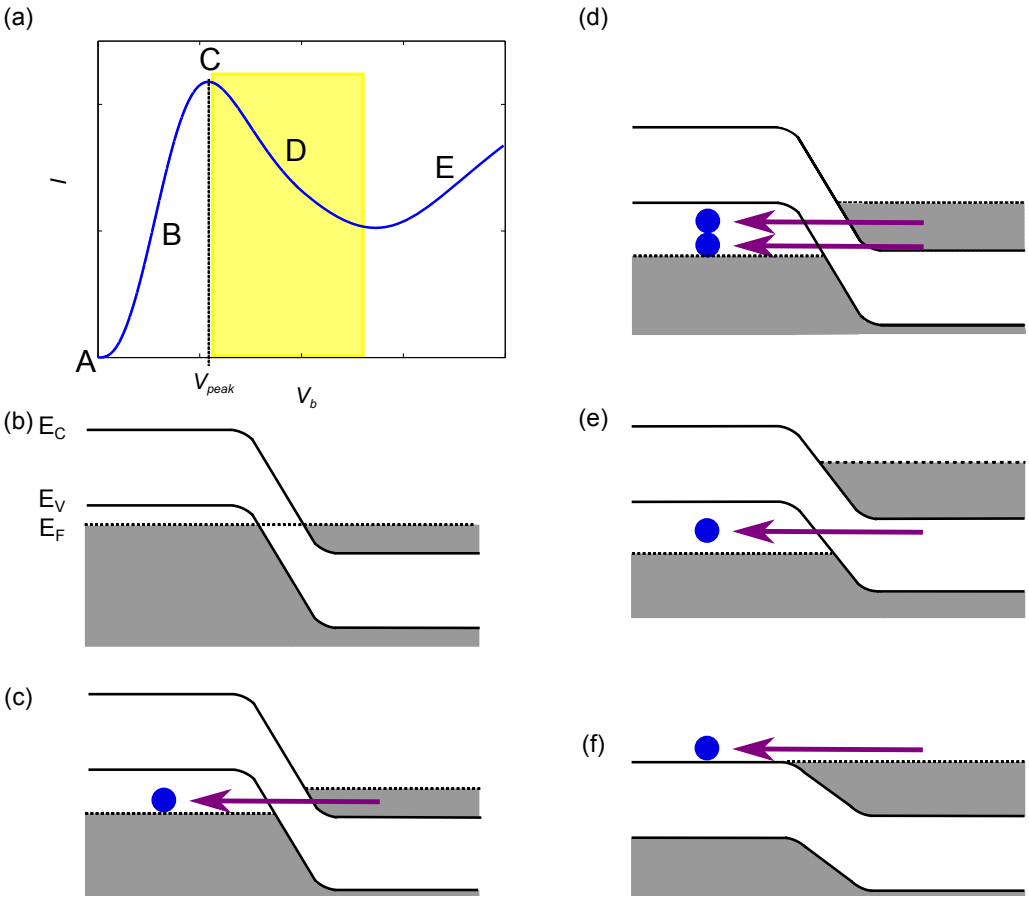

Figure 1.3: (a) The general $I(V)$ characteristics of a tunnel diode, with the NDC region highlighted yellow. Points A-E mark bias voltages for which the band structure is plotted in (b-f). (b) The band structure of a tunnel diode, with positively doped semiconductor on the left, negatively doped semiconductor on the right. The conduction band energy, E_C and valence band, E_V are shown, and filled states are coloured grey. Here, the applied voltage is 0 V, i.e. point A in (a). Fermi levels, E_F, in the p and n regions are aligned and no current flows. (c) A small forward bias is applied and electrons in the conductance band of the n region will tunnel to the empty states in the valence band of the p region. This leads to a small tunnel current (point B). (d) A larger applied voltage leads to a large number of electrons in the n-region having the same energy as empty states in the p-region, thus giving a maximum tunnel current of the peak at C. (e) For $V_b > V_{peak}$, V_b energetically shifts the available tunnelling and empty states such that the tunnelling decreases and thus the current at point D is lower. (f) As the forward bias further increases, the tunnel current drops to zero, but electron-hole injection increases due to the lower potential barrier, point E.

has so many acceptor impurities that states near the top of the valence band are emptied of electrons, such that the Fermi level lies in the valence band. The n-type semiconductor (right), which is doped with donor impurities, has a Fermi level above the band gap and in the conduction band. There exists a depletion layer between the two doped semiconductors, which becomes very thin (~ 10 nm), when the doping is high (with carrier concentrations of $\approx 10^{19}$ cm^{-3}). This reduces the effective barrier width and thus allows tunnelling to occur with high probability. In Figs. 1.3(b-f), the band structure of the diode at various applied bias voltage points A-E (as seen in Fig. 1.3(a)) are shown. When no bias voltage is applied, see Fig. 1.3(b), the Fermi levels in each layer are aligned, and no current flows through the junction (point A). When a small forward bias is applied, Fig. 1.3(c), the Fermi levels in each layer shift with respect to each other and electrons from the conduction band in the n-type semiconductor tunnel through the junction to the valence band of the p-type semiconductor, leading the the current seen at point B. Increasing this bias increases the current to the resonant peak (point C) as the overlap between the available valence states (between E_F and E_V in the p-layer) and the filled conduction states (between E_F and E_C in the n-layer) becomes maximal, as seen in Fig. 1.3(d). Here, the largest number of states are available for tunnelling to a large number of empty states of the same energy. After some voltage, $V = V_{peak}$, the number of states available for tunnelling decreases, because the tunnelling process must conserve energy and the available filled conductance states are mostly no longer energetically aligned with empty valence states, as in Fig. 1.3(e) which gives the reduced current at point D. This is the region of negative differential conductance (NDC), where an increase in applied voltage leads to a decrease in current. In Fig. 1.3(f), the states are so energetically misaligned that no tunnelling occurs. However, we see the current at point E has increased, this is due to the conduction of electrons over the barrier.

1.3.2 Double Barrier Resonant Tunnelling Diodes

Here, we consider the $n-i-n$ DBRTD, a band diagram and cross-section of which are shown in Fig. 1.4(a) ($p-i-p$ and $n-i-p$ are also possible). DBRTDs are usually constructed from III-V semiconductor materials, or similar, and grown via molecular beam epitaxy (MBE) [12, 16, 17]. Two potential barriers of large band gap semiconductor layers, sandwich a central

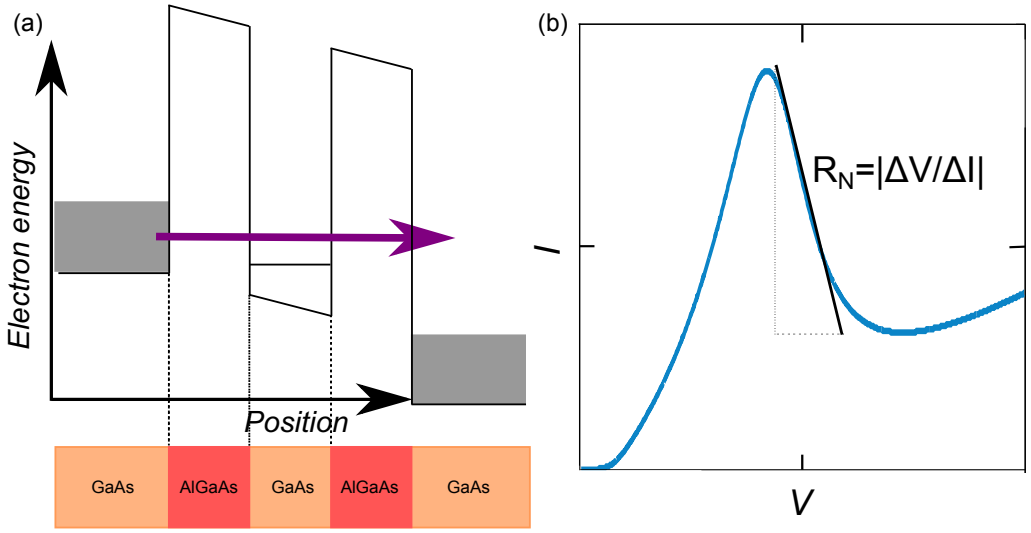

Figure 1.4: (a) Conduction band diagram for a GaAs/AlGaAs $n-i-n$ DBRTD. A double barrier resonant tunnelling diode, traditionally constructed from III-V semiconducting materials, as shown in the bottom schematic diagram. Grey rectangles indicate energy ranges of occupied electron states in the emitter and collector contacts. (b) Example I(V) characteristics with the maximum magnitude of the negative differential resistance, R_N, calculated from the slope of the NDC region.

quantum well formed of a lower band gap semiconductor. The mismatch in the band gaps leads to the production of a quantum well in the potential energy of the electron. Electrons are quasi-confined to the well and so their momentum in the direction perpendicular to the plane is quantized, producing a sequence of quasi-2D subbands. The barriers have a finite thickness, and thus electrons can tunnel out of the well. This structure is then sandwiched by lower band gap semiconductor layers, which act as emitter and collector regions. The emitter region (left of Fig. 1.4(a)) is the source of electrons for tunnelling, and is usually made of a heavily-doped n-type semiconductor, as is the collector region, where electrons collect after tunnelling through the structure.

Like the simple tunnel diode, $n-i-n$ DBRTDs also work through the alignment of energetic states, but the tunnelling is between conduction band states only. The $I(V)$ characteristics, as shown in Fig. 1.4(b), are similar to the Esaki $p-n$ junction diode. However, at low applied bias voltage, there is a delay ($\approx$ picoseconds) in the onset of current. This is because electrons must first tunnel into the states in the central quantum well, before tunnelling out. The mechanism for tunnelling in the DBRTD is also different, as due to the quasi-bound states in the well, a phenomenon known as *resonant tunnelling*

occurs. This is a tunnelling process that is sharply peaked around certain energies, determined by the boundary conditions formed by the quantum well. Electrons with an energy corresponding approximately to the resonant energy level of the quantum well will have a transmission coefficient close to unity. That is, an electron with this resonant energy can cross the double barrier without being reflected. This resonance phenomenon is similar to that taking place in the optical Fabry-Perot resonator or in a microwave capacitively-coupled transmission-line resonator.

When a bias voltage, V_b, is applied across the device, the chemical potential shifts in both semiconducting layers either side of the barrier layers, and also increases the number of electrons contained in the central quantum well. The probability of quantum mechanical tunnelling depends on the available quantized states at both the originating and the receiving sides of the junction. The quantized resonant states in a quantum well can give rise to resonant tunnelling behaviour when the energy of the quantum states with discrete levels align. When aligned, the tunnelling current peaks, exhibiting a negative differential conductance (NDC) at V_b just beyond the resonant bias where the current peak occurs. Such an intriguing NDC behaviour can be exploited in various devices, such as RTDs, to act as an active component in resonant circuits which leads to self-sustained current oscillations. More importantly, the resonant tunnelling phenomena offer unique insight into properties of materials, such as localized defect states (which can be probed by tunnelling spectroscopy [15]), collective electronic excitations, and quantum well band structures. In Fig. 1.4(b), the maximum magnitude of differential resistance, R_N, is defined from the slope of the NDC region. This, combined with the peak-to-valley ratio (PVR) (the peak current/valley current), provides insight into the frequency range and power output of devices, as discussed further in Chapter 4.

The most recent addition to the family of devices that exhibit NDC (Gunn diodes, DBRTDs, superlattices), are graphene-based tunnel transistors with high on-off current switching ratios [17–19]. The NDC in these RTDs arises from the constraints imposed by energy and momentum conservation of Dirac fermions tunnelling through a hexagonal-boron nitride (hBN) barrier when a bias voltage is applied between the two graphene electrodes. Peak-to-valley ratios approaching 2:1 have already been achieved at room temperature, with peak current densities of 26 $\mu A \mu m^{-2}$. The PVR not only gives a good estimate to the output power, but also indicates the control of growth

conditions and the quality of the interfaces between the different materials. When these devices are placed in a resonant LCR circuit, they can generate current oscillations in the MHz range and above [20].

1.4 Graphene

In 1947, Wallace [21] theoretically predicted the unique electronic band structure of graphene, a 2D layer of carbon atoms which comprises the structure of graphite. He noted there would be a linear dispersion relation at low energies, and later studies by McClure [22] and others [23, 24] looked at the wave equation for excitations and realised the similarities to the Dirac equation. It was predicted that graphene would have charge carriers that were effectively massless, which would lead to exceptional current-carrying properties. Attempts to isolate and characterize a monolayer were unsuccessful, and it was presumed to be too unstable due to thermal and other fluctuations that prevent long-range crystalline order at finite temperatures. That was until 2004, when Geim and Novoselov, at the University of Manchester, successfully exfoliated monolayer graphene using Scotch tape on graphite [25]. They were awarded the Nobel Prize in 2010 for the "identification and characterization of graphene", verifying its unique two-dimensional properties. This inspired the investigation of a whole class of novel 2D materials, including higher band gap materials such as boron nitride and molybdenum disulphide [26]. The discovery of graphene has led to an explosion of interest and research, inspiring a wide range of innovative technological applications such as graphene single-electron transistors [27], flexible displays [28, 29], and solar cells [30]. Graphene also has great physical properties for future electronics and other applications, such as; being atomically thin, exceptionally strong, transparent and flexible. The mechanical, magnetic and thermal properties have all led to many areas of research taking an interest in incorporating graphene into their areas. The unique electronic band structure and arising electrical transport properties were also confirmed, which has led to graphene becoming a candidate for integrated circuit components.

1.4.1 Basic Properties of Monolayer Graphene

Since the successful isolation of graphene, research into its extraordinary electronic properties and potential applications has boomed. The unique linear band structure, remarkable electron mobility and phenomenal strength, among many other properties, have marked graphene as a wonder material for the 21st century. Graphene is an ideal candidate for Quantum Hall resistance standard [31–34], due to it's true two-dimensionality, room-temperature operation, and the discrete electronic energy levels that arise in a magnetic field, called *Landau levels*. Single-layer sheets were the main initial focus of research, but in time, bilayer and trilayer graphene have been investigated, with many exciting results such as the Hofstadter butterfly effect [35, 36] and the realization of graphene LEDs [37]. This thesis will focus on the high-frequency application of monolayer graphene heterostructures.

1.4.2 Graphene Hexagonal Lattice

Graphene is a 2D hexagonal lattice of carbon atoms, as seen in Fig. 1.5(a), with primitive lattice vectors

$$\mathbf{a_1} = \left(\frac{a}{2}, \frac{\sqrt{3}a}{2}\right), \qquad \mathbf{a_2} = \left(\frac{a}{2}, \frac{-\sqrt{3}a}{2}\right), \tag{1.17}$$

where $a = |\mathbf{a_1}| = |\mathbf{a_2}| = 2.46$ Å is the lattice constant. The carbon atoms (circles) exist on two distinct triangular sublattices, A (unfilled) and B (filled), identified by the shape of the bonds to the surrounding atoms, i.e. for the A sublattice, the atoms have a "Y"-shaped bond, and for the B sublattice, the atoms have a "λ"-shaped bond. The lattice vectors are described in Cartesian coordinates with x and y axes in the plane of the graphene sheet, and the z axis perpendicular to the graphene sheet. Each carbon atom has four valence electrons, three of which combine in the graphene plane to form sp^2 orbitals. These form σ bonds with the surrounding carbon atoms, whilst the $2p_z$ orbital, which is perpendicular to the graphene plane, forms π bonds with neighbouring atoms.

1.4.3 The Reciprocal Lattice of Graphene

The reciprocal lattice points are plotted with crosses in Fig. 1.5(b-c), with the reciprocal lattice vectors, $\mathbf{b_1}$ and $\mathbf{b_2}$. The first Brillouin Zone of graphene

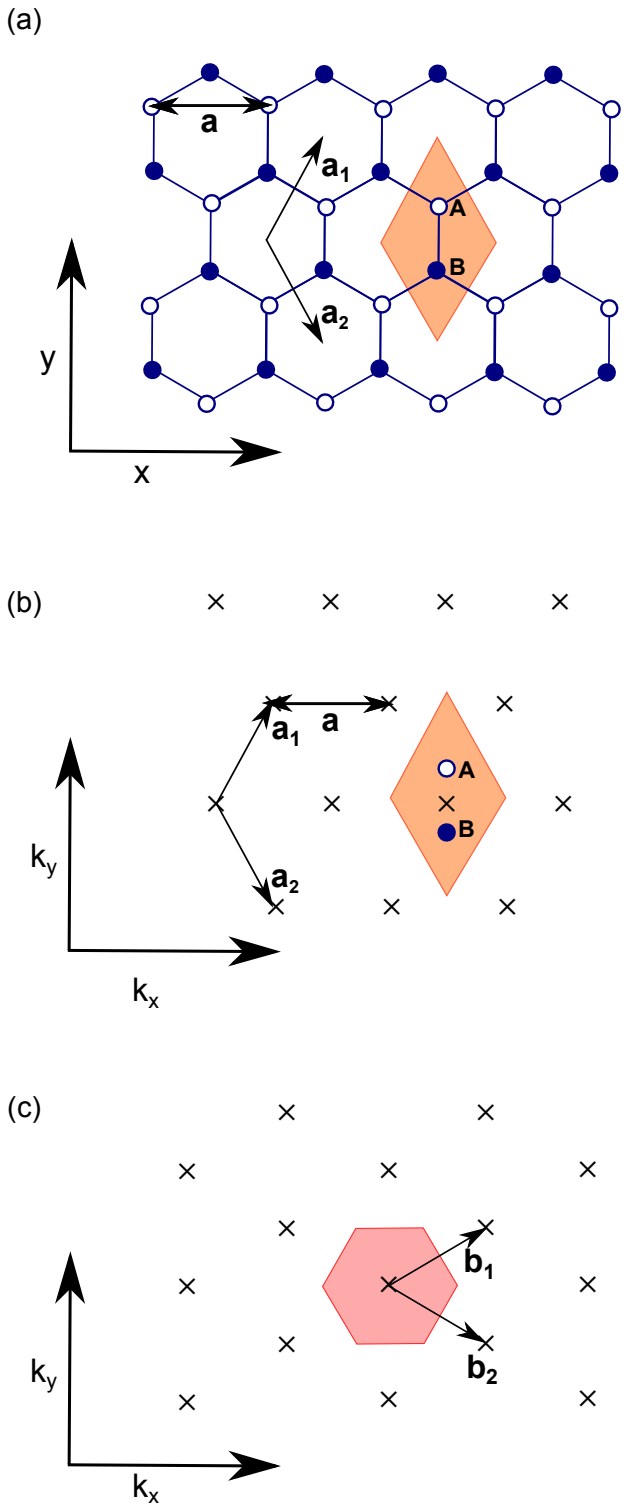

Figure 1.5: (a) The real space lattice structure of graphene - a honeycomb crystal structure of alternating carbon atoms (filled and unfilled circles) on A and B sites, with σ bonds between them (straight lines). The primitive lattice vectors, $\mathbf{a_1}$ and $\mathbf{a_2}$, are equal to the length of the lattice constant, a. The unit cell (orange diamond) contains two carbon atoms, one on each site: A and B. (b) Reciprocal space plot of lattice points of the Bravais lattice (crosses). (c) Reciprocal space plot of the first Brillouin zone of graphene (pink hexagon), with reciprocal lattice vectors, $\mathbf{b_1}$ and $\mathbf{b_2}$.

is indicated by the pink hexagon. The primitive reciprocal lattice vectors must satisfy $\mathbf{a_1 b_1} = \mathbf{a_2 b_2} = 2\pi$ and $\mathbf{a_1 b_2} = \mathbf{a_2 b_1} = 0$, and are thus given by

$$\mathbf{b_1} = \left(\frac{2\pi}{a}, \frac{2\pi}{\sqrt{3}a}\right), \qquad \mathbf{b_2} = \left(\frac{2\pi}{a}, \frac{-2\pi}{\sqrt{3}a}\right). \tag{1.18}$$

The unit cell of the lattice (orange rhombus) contains two identical atoms with non-equivalent Dirac points, $\mathbf{K}^{\pm} = (\pm 4\pi/3a, 0)$, in the Brillouin zone. At these points, the conduction and valence bands meet, as discussed in Section. 1.4.4.

1.4.4 Band Structure of Graphene

The electronic band structure of graphene can be calculated using the *tight-binding model*, or LCAO (linear combination of atomic orbitals), which is outlined below. The model assumes the electrons of each atom to be close, or *tight*, to the atom to which it belongs and have limited interaction with states and potentials on surrounding atoms of the solid. It uses an approximate set of wave functions based upon the superposition of wave functions of the isolated atoms located at each lattice site. The model has been shown to give good qualitative results.

General Tight-Binding Model

Electrons in a periodic lattice, such as graphene, can be described by a Bloch function,

$$\phi_j(\mathbf{k}, \mathbf{r}) = \frac{1}{\sqrt{N}} \sum_{i=1}^{N} e^{i\mathbf{k}.\mathbf{R_{j,i}}} \phi_j(\mathbf{r} - \mathbf{R_{j,i}}). \tag{1.19}$$

Here, $\mathbf{r}$ is the position vector, $\mathbf{k}$ is the wavevector, N is the number of unit cells within the lattice, labelled $i = 1...N$, and $\mathbf{R_{j,i}}$ is the position of the jth orbital in the ith unit cell. In the tight-binding approximation, the wavefunction, $\psi_j(\mathbf{k}, \mathbf{r})$, for a system with n atomic orbitals ($j = 1....n$) can be written as a linear combination of orbitals, ϕ_l,

$$\psi_j(\mathbf{k}, \mathbf{r}) = \sum_{l=1}^{n} c_{j,l}(\mathbf{k}) \phi_l(\mathbf{k}, \mathbf{r}), \tag{1.20}$$

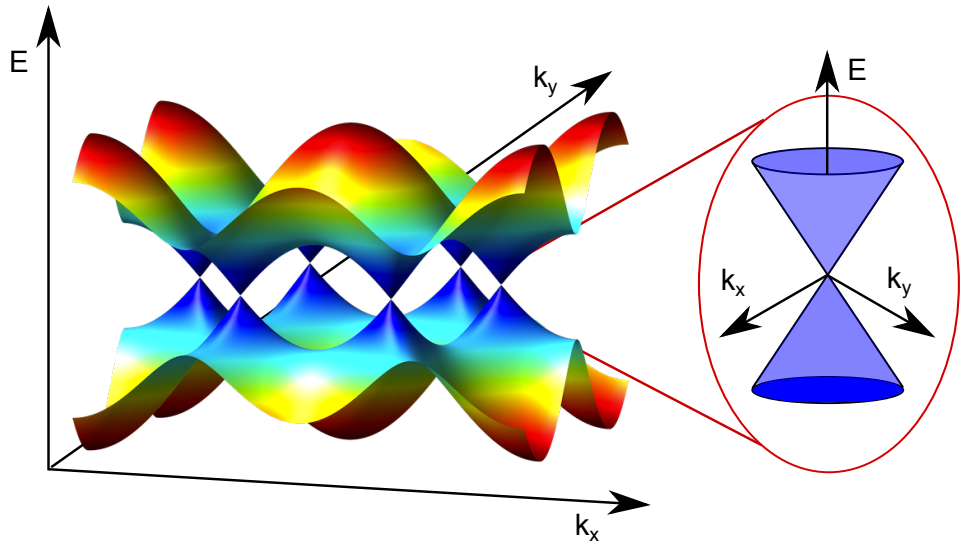

Figure 1.6: The band structure $E(k_x, k_y)$, of monolayer graphene around the first Brillouin Zone. The conduction band and valence band meet at 6 Dirac points at $E = 0$, one of which is shown in the close-up. Around the Dirac points, the dispersion is linear.

where $c_{j,l}$ are coefficients of expansion. The energy of the tight-binding wavefunction can be evaluated by substituting $\psi_j(\mathbf{k}, \mathbf{r})$ into the time-independent Schrödinger equation,

$$\hat{H}\psi_j(\mathbf{k}, \mathbf{r}) = E_j\psi_j(\mathbf{k}, \mathbf{r}). \tag{1.21}$$

The energy of the jth band, $E_j(\mathbf{k})$, can be calculated by multiplying from the left by the wavefunction and integrating over all space to give:

$$E_j(\mathbf{k}) = \frac{\langle\psi_j|\hat{H}|\psi_j\rangle}{\langle\psi_j|\psi_j\rangle}. \tag{1.22}$$

This can be written in terms of the Bloch states,

$$E_j(\mathbf{k}, \mathbf{r}) = \frac{\sum_{i,l}^{n} c_{ji}^* c_{jl}\langle\phi_i|\hat{H}|\phi_l\rangle}{\sum_{i,l}^{n} c_{ji}^* c_{jl}\langle\phi_i|\phi_l\rangle} = \frac{\sum_{i,l}^{n} c_{ji}^* c_{jl} H_{il}}{\sum_{i,l}^{n} c_{ji}^* c_{jl} S_{il}} \tag{1.23}$$

for each energy band. Here, $H_{il} = \langle\phi_i|\hat{H}|\phi_l\rangle$ are defined as the transfer integral matrix elements, and $S_{il} = \langle\phi_i|\phi_l\rangle$ are the overlap integral matrix elements. Minimising the energy [38] leads to the matrix equation

$$H\phi_j = E_j S\phi_j, \tag{1.24}$$

which allows the energies E_j to be calculated by solving

$$\det(H - E_j S) = 0. \tag{1.25}$$

Tight-Binding Model for Monolayer Graphene

The transfer integral matrix, H, and the overlap integral matrix, S, can now be calculated for graphene. Each unit cell in graphene contains two carbon atoms, therefore, we can replace $j = 1...n$ by $j = A$ and $j = B$. The diagonal matrix element corresponding to the A sublattice is

$$\begin{aligned} H_{AA} &= \frac{1}{N}\sum_{i=1}^{N}\sum_{j=1}^{N} e^{i\mathbf{k}\cdot(\mathbf{R}_{A,j}-\mathbf{R}_{A,i})}\langle\phi_A(\mathbf{r}-\mathbf{R}_{A,i})|H|\phi_A(\mathbf{r}-\mathbf{R}_{A,j})\rangle \\ &\approx \frac{1}{N}\sum_{i=1}^{N}\langle\phi_A(\mathbf{r}-\mathbf{R}_{A,i}|H|\phi_A(\mathbf{r}-\mathbf{R}_{A,i})\rangle. \end{aligned} \tag{1.26}$$

The approximation is due to the dominant contribution arising from the same site, i.e. $j = i$, within every unit cell. Although next-nearest neighbours would contribute to the electronic band structure, the contribution is negligible [38]. The right-hand side of the sum can then be set to be the energy of the orbital, ϵ_i, which is the same for all orbitals. This gives

$$H_{AA} \approx \frac{1}{N}\sum_{i=1}^{N}\epsilon_i = \epsilon. \tag{1.27}$$

As the B sublattice is identical to the A sublattice, we can also say $H_{BB} = H_{AA}$. The diagonal elements of the overlap integral matrix can similarly be calculated to find $S_{AA} = S_{BB} = 1$.

The off-diagonal matrix elements can be calculated assuming the contribution arises mostly from hopping between the three nearest neighbours on sites $l = 1, 2, 3$:

$$H_{AB} \approx \frac{1}{N}\sum_{i=1}^{N}\sum_{l=1}^{3} e^{i\mathbf{k}\cdot(\mathbf{R}_{B,l}-\mathbf{R}_{A,i})}\langle\phi_A(\mathbf{r}-\mathbf{R}_{A,i})|H|\phi_B(\mathbf{r}-\mathbf{R}_{B,j})\rangle. \tag{1.28}$$

The matrix element between neighbouring atoms is independent of the site of the neighbour, thus all $\langle\phi_A|H|\phi_B\rangle$ can be set to equal the hopping parameter, t. This is negative, thus we will use $\gamma_0 = -t$. The off-diagonal

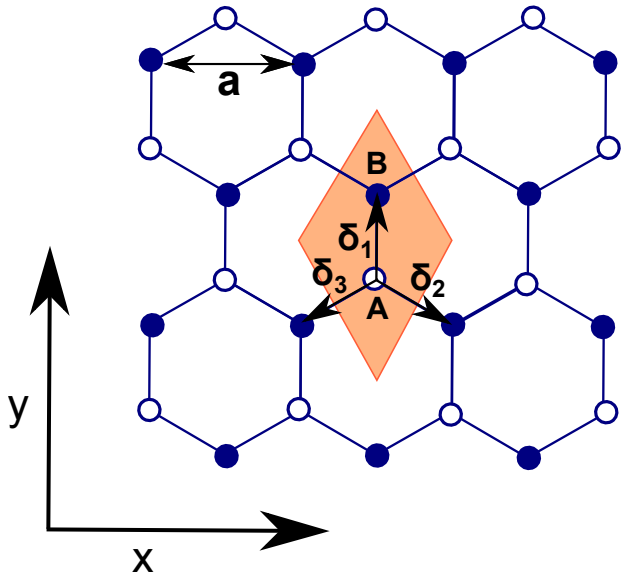

Figure 1.7: The nearest-neighbours of an atom on the A sublattice (white) lie on the B sublattice (blue) and are connected by position vectors δ_1, δ_2 and δ_3.

matrix element now becomes

$$H_{AB} = -\frac{1}{N}\sum_{i=1}^{N}\sum_{l=1}^{3} e^{i\mathbf{k}\cdot(\mathbf{R}_{B,l}-\mathbf{R}_{A,i})}\gamma_0,$$
$$= -\frac{\gamma_0}{N}\sum_{i=1}^{N}\sum_{l=1}^{3} e^{i\mathbf{k}\cdot\delta_l} \equiv -\gamma_0 f(\mathbf{k}). \tag{1.29}$$

H_{BA} is the complex conjugate of H_{AB}, i.e. $H_{BA} \approx -\gamma_0 f^*(\mathbf{k})$. Similarly, the off-diagonal elements of the overlap integral matrix can be calculated to give:

$$S_{AB} = s_0 f(\mathbf{k}) = S^*_{BA}, \tag{1.30}$$

where $s_0 = \langle\phi_A(\mathbf{r}-\mathbf{R}_{A,i})|\phi_B(\mathbf{r}-\mathbf{R}_{B,l})\rangle$. The function, $f(\mathbf{k})$, that describes the nearest-neighbour hopping can be evaluated by considering the position of the three nearest-neighbours, which are from the opposite sublattice, as shown in Fig. 1.7. The vectors connecting the considered A atom and the

neighbouring B atoms are:

$$\begin{aligned}\delta_1 &= \left(0, \frac{a}{\sqrt{3}}\right), \\ \delta_2 &= \left(\frac{a}{2}, -\frac{a}{2\sqrt{3}}\right), \\ \delta_3 &= \left(-\frac{a}{2}, -\frac{a}{2\sqrt{3}}\right).\end{aligned} \tag{1.31}$$

Here, $|\delta_1| = |\delta_2| = |\delta_3| = a/\sqrt{3}$ is the carbon-carbon bond length. The hopping function can then be evaluated:

$$\begin{aligned}f(\mathbf{k}) &= \sum_{l=1}^{3} e^{i\mathbf{k}\cdot\mathbf{d}_l} \\ &= e^{ik_y a/\sqrt{3}} + 2e^{-ik_y a/2\sqrt{3}} \cos(k_x a/2).\end{aligned} \tag{1.32}$$

It now follows that, we can now write the transfer integral matrix and the overlap integral matrix for monolayer graphene as:

$$H = \begin{bmatrix} \epsilon & -\gamma_0 f(\mathbf{k}) \\ -\gamma_0 f^*(\mathbf{k}) & \epsilon \end{bmatrix} \tag{1.33}$$

Solving for the energies as in Eq.(1.25), it is found:

$$E_\pm = \frac{\epsilon \pm \gamma_0 |f(\mathbf{k})|}{1 \mp s_0 |f(\mathbf{k})|}. \tag{1.34}$$

Here, E_+ gives the energy of the conduction band, and E_- gives the energy of the valence band. In [39], the parameter values are stated; $\gamma_0 = 3.033$ eV, $s_0 = 0.129$ and $\epsilon = 0$. The resulting band structure is plotted in Fig. 1.6, where we see the conduction and valence bands cross at six points on the edge of the Brillouin Zone with zero energy gap. Around these points, labelled $K^\pm$, the dispersion is linear, and electrons near these points can be described by a Dirac-like Hamiltonian. In [38], $f(\mathbf{k})$ is calculated at these Dirac points and is found to be zero, i.e. there is no coupling between the A and B sublattices at these points. Approximating near the Dirac points gives a non-zero coupling:

$$f(\mathbf{k}) \approx \frac{\sqrt{3}a}{2\hbar}(\xi p_x - i p_y), \tag{1.35}$$

where $\xi = \pm 1$ for K^+ and K^- valleys respectively, and $\mathbf{p} = (p_x, p_y) = \hbar\mathbf{k} - \hbar\mathbf{K}^{\pm}$. Therefore around the Dirac points, the transfer integral matrix is:

$$H = v \begin{bmatrix} 0 & \xi p_x - i p_y \\ \xi p_x + i p_y & 0 \end{bmatrix}, \tag{1.36}$$

where the velocity $v = \sqrt{3}a\gamma_0/(2\hbar)$. Within the linear dispersion regime, the overlap matrix, S, is approximately the unit matrix and thus the energy eigenvalues and eigenstates for monolayer graphene at low-energy are found to be:

$$\begin{aligned} E_{\pm} &= \pm\hbar v_F k, \\ \psi_{\pm} &= \frac{1}{\sqrt{2}} \left(\begin{bmatrix} 1 \\ \pm\xi e^{i\xi\varphi} \end{bmatrix} e^{i\mathbf{k}\cdot\mathbf{r}/\hbar} \right). \end{aligned} \tag{1.37}$$

Here, the $\pm$ refer to the conduction and valence bands, respectively, and φ is the angle of the momentum, $\mathbf{p}$, in the graphene plane. The linear dependence of energy on momentum is unique and leads to a linear density of states (DoS) relation also.

The band structure is shown in Fig. 1.6, which is found to be rather different from usual three-dimensional materials. Six double cones meet at $E = 0$ V, around which the dispersion relation is linear. These are the Dirac, or *neutrality*, points. A striking result of the dispersion around these points is that the Fermi velocity does not depend on energy or momentum. The band gap, i.e. the energy range between the valence band and the conduction band for which no states exist, is zero for graphene. For an undoped sample of graphene, the Fermi level is situated at this neutrality point, where the conductance and valence bands meet, i.e. the valence band is completely filled with electrons and the conductance band is empty. At this point, the density of states, which is also linear with energy at low E (see derivation below), is zero and thus the electrical conductivity of intrinsic graphene is low and of the order of the conductance quantum, $\sigma \sim e^2/h$. The Fermi level can be altered by doping, either chemically or by applying an electric field, or by adsorbing molecules onto its surface, such as water or ammonia [40]. For doped graphene, the electrical conductivity can be very high, potentially higher than that of copper at room temperature (bulk conductivity for graphene has been measured as 0.96 $\times 10^6$ $\Omega^{-1}\text{cm}^{-1}$ which

is higher than the conductivity of copper = 0.6 $\times 10^6$ Ω^{-1}cm^{-1}). The 2D nature of graphene and extremely high mobility at room temperature allows electrons to conduct very well.

Derivation of the Density of States

It is possible to derive the density of states in graphene at low E using the linear dispersion relation, $E = \hbar v_F k$. Each state in 2D k-space will have an area, $A_{state} = \left(\frac{2\pi}{a}\right)^2$, where a is the distance between k states. If we consider an arbitrary circle in k-space with radius $\mathbf{k}$, this will encompass an area, $A_{circle} = \pi k^2$. The number of filled states in this circle is then:

$$\begin{aligned} N_{circle}(k) &= g_v g_s \frac{A_{circle}}{A_{state}}, \\ &= 2 \times 2 \times \frac{k^2 L^2}{4\pi^2}, \end{aligned} \tag{1.38}$$

as the valley degeneracy, $g_v = 2$, and the spin degeneracy, $g_s = 2$. This can be written in terms of E:

$$N_{circle}(E) = \frac{E L^2}{\hbar^2 {v_F}^2 \pi}. \tag{1.39}$$

The density of states is the number of states per unit energy per unit volume, so differentiating with respect to E gives:

$$DoS(E) = \frac{2E}{\hbar^2 v_F^2 \pi}, \tag{1.40}$$

thus, the density of states (DoS) varies linearly with E for all E where $E = \hbar v_F k$, which is true for up to $E \approx 1$ eV.

1.4.5 Pseudospin and Chirality

In a single Dirac cone, there is a contribution to the energy band from both the A and B sublattice of graphene, as seen in Fig.1.8 (red and green, respectively). An electron with energy E propagating in the positive x-direction will originate from the same branch of the electronic spectrum as a hole with energy $-E$ propagating in the negative direction. Therefore electrons and holes from the same branch have a pseudospin, σ, pointing in the same direction, which is parallel to the momentum for electrons and antiparallel for holes. Pseudospin is analogous to electron spin and, in graphene, is opposite

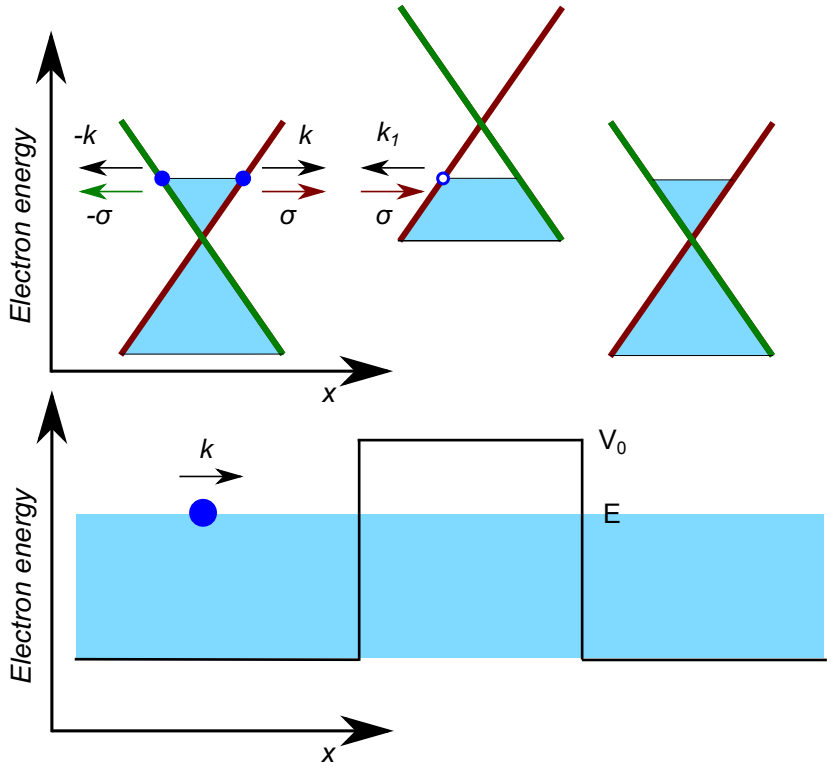

Figure 1.8: Dirac cones around and inside a potential barrier of height V_0. The red and green branches represent the pseudospin that arises from the sublattice origin of the electron or hole. The momentum, k or k_1, is parallel to an electrons pseudospin and antiparallel to a holes pseudospin, which leads to the definition of chirality. The schematic below shows an electron of energy E with momentum k incident on the barrier.

for the K^+ and K^- points. Chirality [41] is the projection of pseudospin onto the direction of motion, and is thus positive for electrons, and negative for holes. Chirality refers to the inbuilt symmetry felt by electrons and holes and is most noteable in graphene. Other semiconductors do have pseudospin effects [42] but due to the non-linear band structure and the lack of neutrality point, the chirality is mixed in traditional semiconductors.

Graphene offers clear advantages for future electronic technologies due to its high mobility and conductivity. However, difficulties in controlling electron transport arise due to Klein tunnelling and the absence of a band gap, which make it difficult to achieve low power dissipation in an off state. Traditional semiconductors have a band gap that encompasses a range of energies for which there are no states available. This exists between the valence band and conduction band. However, due to the unusual band structure of graphene, discussed in detail in Section 1.4.4, no such band gap exists. This leads to sensitivity issues when trying to construct a typical field-effect transistor (FET) or similar, as usually the OFF-state is within the band gap, but without one, even a small number of electrons existing in states around the neutrality point can affect the switching. This motivates the search for novel 2D materials such as van der Waal heterostructures.

1.4.6 Klein Tunnelling

In 1929, the Klein paradox was inferred [43] from the Dirac equation,

$$(\sigma_x p + V)\,\psi = E\psi, \tag{1.41}$$

where σ_x is the Pauli spin matrix, applied to the problem of a massless relativistic particle incident on a potential barrier. This surprising result showed that the particle would tunnel with $T = 1$. Even more suprising, if an electron is incident on a potential of the order of the electron mass, $V \sim mc^2$, the barrier is almost transparent, i.e. $T \approx 1$. As the potential approaches infinity, the reflection diminishes and the electron is always transmitted, i.e. $T = 1$. If the electron was behaving non-relativistically, exponential damping in the barrier of the wavefunction would be expected, however, in the Klein paradox, the electron behaves relativistically. The phenomenon of the electron passing through the barrier with a unitary probability is known as *Klein tunnelling*.

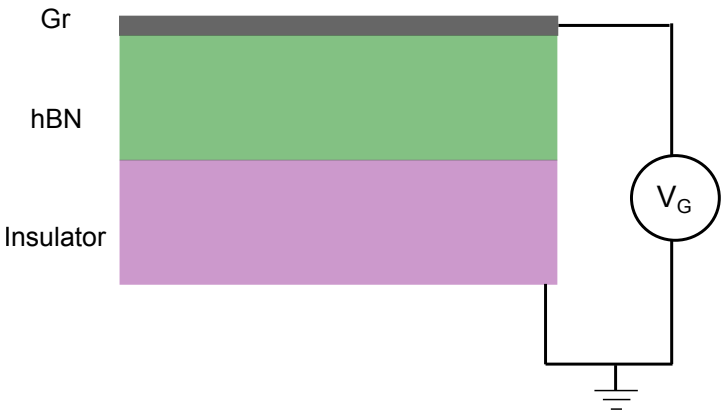

Figure 1.9: A schematic diagram of graphene (grey) mounted on hBN (green) and an insulator (purple), with a gate voltage applied across the device.

At low energies, in graphene, the electrons behave as massless Dirac fermions. When incident on the barrier at normal incidence, the tunnel barrier can become fully transparent, i.e. the probability of tunnelling is unity. Under certain conditions, the transparency of the tunnel barrier can oscillate as a function of energy or angle of incidence [44, 45], a property that could be useful for controlling electronic devices.

1.4.7 Field Effect in Graphene

The field effect in graphene can be shown by applying a gate voltage, V_g, across a device consisting of graphene mounted on hBN and an insulator, as seen in Fig. 1.9. This effect is the foundation for the field effect transistor and was shown in the primary graphene investigations [25]. On application of V_g, a field, F_g, is induced across the device. Due to the low density of states in graphene, this induces a charge on the graphene layer, n, and the chemical potential, μ, can be significantly changed, depending on the thickness of the device, D,

$$eV_g = \mu(n) - eF_gD. \tag{1.42}$$

This will be further discussed in Section 2.2, along with an introduction to the resulting quantum capacitance effect.

1.5 Boron Nitride

1.5.1 General Properties

Hexagonal-boron nitride has a honeycomb structure like graphene, with a very similar lattice constant, and is thus an ideal candidate to combine with graphene in van der Waals heterostructures, as described in Section. 1.6. It is very stable, in particular, being heat- and chemical-resistant. The band gap of hBN is ~ 5 eV and is thus favourable for its potential as a tunnel barrier in graphene heterostructures, as it means electrons will exhibit quantum tunnelling through the barrier, giving rise to a tunnel current, rather than conduction over the barrier which may occur with 2D materials with lower band gaps. Bulk hBN crystals have also been shown to be an exceptional substrate for graphene, allowing a tenfold increase in its electronic quality [46].

1.5.2 Barrier Properties

The hBN layers act as an electrostatic potential barrier with a potential energy determined by the barrier height Δ, which we take to be half of E_{gap}, as shown in Fig.1.10. The electrostatic potential energy is defined as the amount of work done by an electric field in carrying a unit positive charge from infinity to that point.

1.6 Van der Waals Heterostructures

A new class of heterostructure materials have emerged since the realization of graphene and other two-dimensional (2D) crystals. Such crystals are freestanding and chemically stable. Multilayer structures, known as van der Waal heterostructures, can be achieved simply by stacking, or growing, various 2D atomic crystals on top of each other, as seen in Fig. 1.11. The electronic properties of such devices can be tuned by design. The beauty of van der Waals heterostructures is the ease of modification. For example, changing the orientation of the layers when stacking can lead to dramatic alterations in the electronic properties. Devices with electronic properties fundamentally different from those constructed with conventional semiconductor materials can be achieved by formulating the composition of such novel heterostructures [35–37]. Another advantage of heterostructures

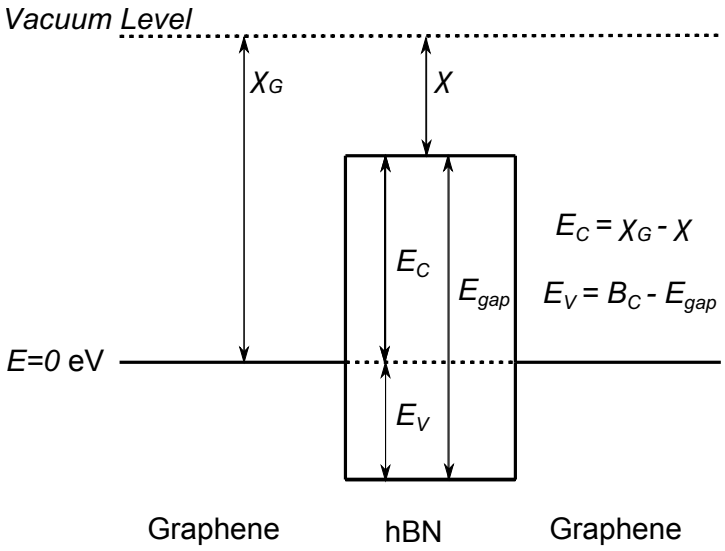

Figure 1.10: The band edge structure for a graphene RTD with zero applied voltage. E_C and E_V are the conductance and valence band energies in hBN relative to the Fermi level of graphene at $E = 0$. The electron affinities, $\chi = 1.11$ eV and $\chi_G = 4.25$ eV, show the amount of energy required to reach the vacuum level. For hBN, $E_{gap} \approx$ 4.7eV - 5.3eV [47–49].

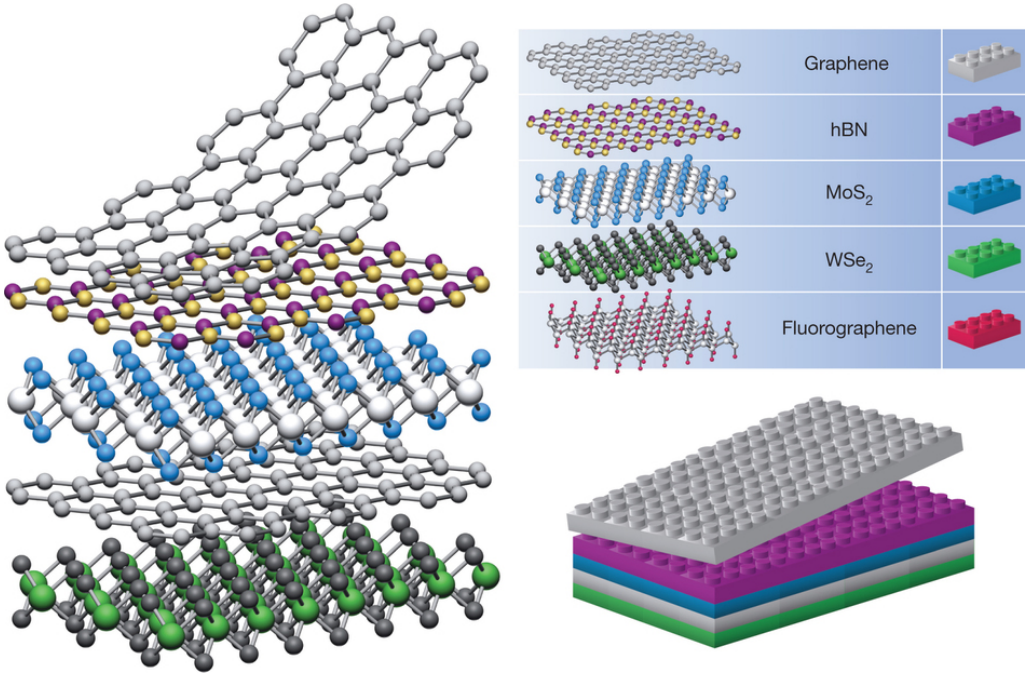

Figure 1.11: A variety of 2D crystals can be stacked like Lego blocks in many combinations, leading to a huge range of van der Waal heterostructures with a, potentially, vast array of tailored properties. Figure reproduced from [50].

is they are 'self-cleansing' as the van der Waals forces attract adjacent crystal layers and effectively squeeze out contaminants.

The main focus of this thesis is the graphene resonant tunnelling diode (GRTD) consisting of two graphene electrodes, exfoliated from highly-ordered pyrolytic graphite, separated by a thin hexagonal-boron nitride layer, or other 2D crystalline material, see Fig. 1.12. The combination of hBN and graphene is particularly attractive due to the small mismatch in their crystal lattices and the exceptional crystalline quality [20, 51–61]. The hBN acts as a vertical transport barrier and is of thickness in the range of d = 0.5 to 2 nm [62]. The tunnel barrier is thin enough to allow the quantum mechanical tunnelling of electrons through the barrier. This is key to the operation of our device. The bottom and top graphene electrodes overlap to make an active tunnelling area, A. The remainder of the graphene electrodes act as leads that carry current away from the active region to Ohmic, gold contacts between which a bias voltage, V_b, is applied. This heterostructure is mounted on a thick layer of hBN, which acts as an atomically-flat substrate. This is then mounted on the oxidised surface of an n-doped silicon substrate, to which a further contact can be attached to allow a gate voltage to be applied across the device, see Fig. 1.12. This allows the fine tuning of the position of the resonant peak and alterations to the lineshape of the current-voltage characteristics. The gated structure may then act as a field-effect transistor (FET). In [51], measurements of a vertical graphene heterostructure FET were first made. Here, the results show no resonant peak, as the graphene lattices are highly misaligned with respect to each other. In such a misaligned sample, there will be no momentum conservation, and the majority of current must arise from elastic scattering events.

These novel van der Waal structures offer an unprecedented degree of control of the electronic properties through means of barrier material choice, barrier thickness, chemical doping levels and relative orientation of the component layers. For example, it has been shown that the relative rotational alignment of the lattices of 2D van-der-Waals heterostructures can significantly affect their properties. In our devices, the crystal lattices of the two graphene layers are intentionally aligned to a high degree of precision, $\theta < 2^\circ$ during the fabrication procedure. The graphene layers are assumed to be flat and with few impurities. In the fabrication of initial devices, the boron nitride lattice is intentionally misaligned with respect to the lattices of the graphene electrodes, by an angle ϕ_M. This means that moiré pattern

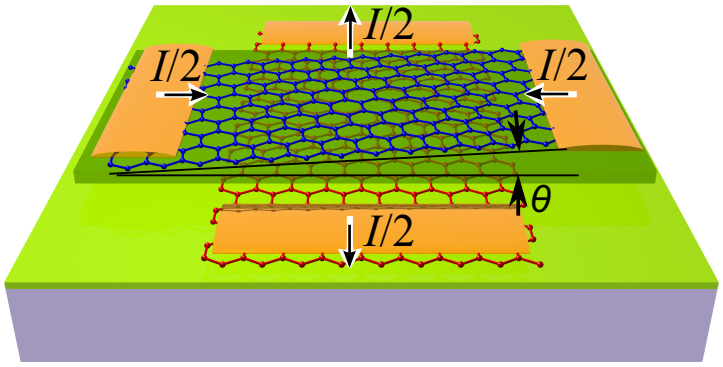

Figure 1.12: A schematic diagram of the graphene-RTD comprising a bottom (red) and top (blue) graphene lattices which are misaligned by an angle θ and separated by a hBN tunnel barrier. The current, I, from the tunnel region flows along the graphene layers to gold contacts (yellow). The diode is mounted on a hBN (green) and SiO_2.

effects, discussed further in Chapter 5, can be assumed to be negligible. If aligned to within $\phi_M < 5°$, moiré fringe superlattice effects would modify the graphene band structure. For the initial model however, the barrier layers will be treated as a dielectric slab. Chapter 3 will explore the $I_b(V_b)$ characteristics attained through fine-tuning of the device design and circuit parameters. Further details of the preparation of the device are found in [51].

When a bias voltage is applied, a tunnel current is generated between the graphene electrodes. Applying a gate voltage allows us to align the Dirac points of the two graphene electrodes whilst maintaining control of their chemical potentials.

1.7 Resonant Circuits

Electrical circuits containing a resistor (R), inductor (L) and capacitor (C), i.e. an RLC circuit, acts as a simple harmonic oscillator with a natural resonant frequency and damping factor, both determined by the configuration of the components. Resonance occurs in the circuit as the system is able to store and transfer energy between two or more different storage modes. In the case of the RLC circuit, energy is transferred between the inductor, where it is stored as a magnetic field in the coil, and the capacitor, where is is stored

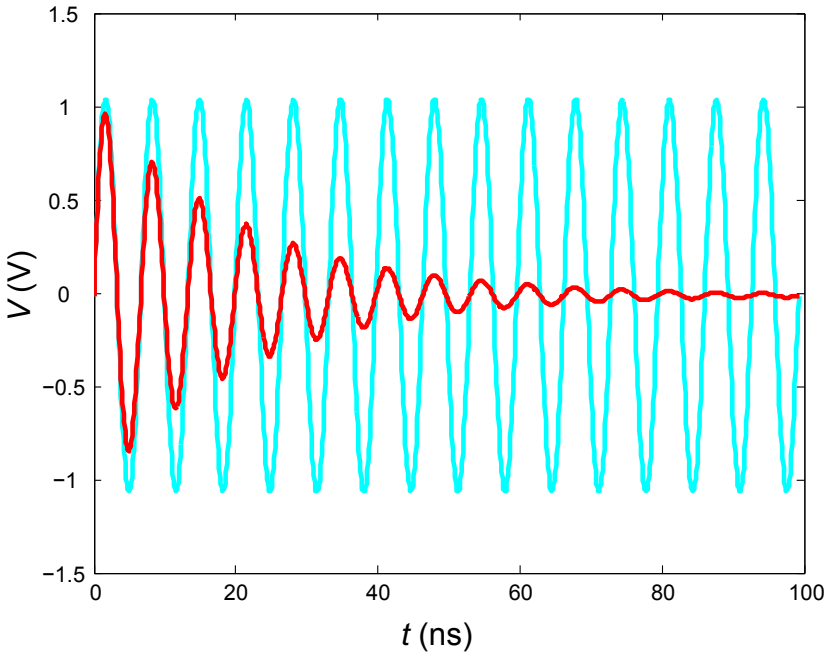

Figure 1.13: Voltage-time oscillations in an undamped circuit (cyan curve) and a damped circuit (red curve).

temporarily as an electric field. When the damping is small, the resonant frequency is approximately the natural frequency of the system. When the resistance is positive, current oscillations will decay in time, as seen in Fig. 1.13 (red curve), whereas the undamped (cyan curve) oscillations maintain their magnitude in time. If a device that exhibits NDC is introduced to the circuit, such as the GRTD, the negative resistance can compensate for the lossy resistances and result in reduced decay or the achievement of self-sustained current oscillations.

The natural, undamped frequency of a circuit is $f_0 = 1/2\pi\sqrt{LC}$ [63]. The resonant frequency is similar and depends on the circuit configuration and parameters. If all components are in series, as in Fig.1.14(a), the resonant frequency is the same as the natural frequency. This can be shown by considering the step response of a series circuit. From Kirchoff's Laws, we know for a resistor, inductor and capacitor, their respective voltages and currents will be:

$$V = V_R + V_L + V_C, \tag{1.43}$$

$$I = I_R = I_L = I_C, \tag{1.44}$$

where V and I are the total voltage and current, respectively. For a dc

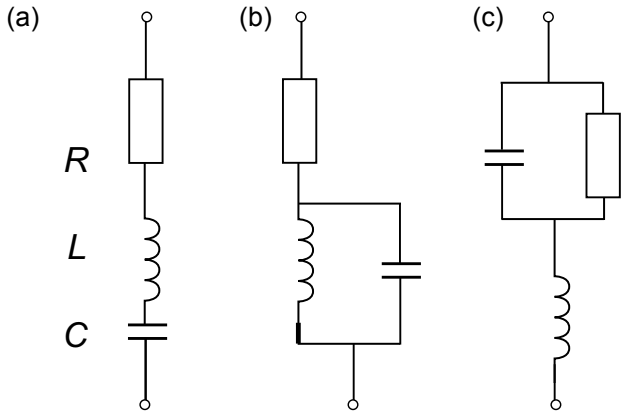

Figure 1.14: Circuit configurations with different resonant frequencies (a) R, L and C all in series, (b) L and C in parallel, with R in series, (c) C and R in parallel, with L in series.

circuit, $dV/dt = 0$, thus we can write:

$$0 = R\frac{dI}{dt} + L\frac{dI^2}{dt^2} + \frac{I}{C}. \tag{1.45}$$

This can be rearrange to give

$$\frac{dI^2}{dt^2} + \frac{R}{L}\frac{dI}{dt} + \frac{I}{CL} = 0 \tag{1.46}$$

$$\frac{dI^2}{dt^2} + 2\alpha\frac{dI}{dt} + \omega_0^2 I = 0, \tag{1.47}$$

where $\alpha = R/2L$ is the decay, or *neper frequency*, and $\omega_0^2 = 1/CL$ is the angular resonant frequency.

Similarly, when the resistance is placed in parallel to the capacitor, as in Fig.1.14(b) the resonant frequency can be calculated to be:

$$f_0 = \frac{1}{2\pi}\sqrt{\frac{1}{LC} - \frac{1}{(RC)^2}}, \tag{1.48}$$

and for the configuration in Fig.1.14(c), the resonant frequency will be:

$$f_0 = \frac{1}{2\pi}\sqrt{\frac{1}{LC} - \left(\frac{R}{L}\right)^2}. \tag{1.49}$$

It is possible to approximate the frequency expected when a GRTD is placed in a resonant circuit. The device acts as a capacitor and a negative resistor, and a small signal analysis can be performed, see Chapter 4. A

quality (Q)-factor can be used to describe how under-damped an oscillator is and predict whether self-sustained oscillations will be achieved, or if the decay will be exponential (heavily-damped) or sinusoidal (damped).

1.8 Conclusion

Graphene exhibits many unique electronic properties, which could potentially be harnessed for high-frequency electronics. In order to expand the incorporation of graphene into modern electronics, for instance, to produce a full-graphene mobile telephone, the first step is to realise a good quality graphene oscillator. Resonant tunnelling diodes formed of graphene heterostructures are predicted to operate at desirable voltages and temperatures, with a reasonable current output. They are also predicted to be much faster than current resonant tunnelling devices due to the lack of central quantum well and reduced dwell times. The purpose of this investigation is to predict how factors such as the alignment between graphene lattices, the alignment between the tunnelling barrier lattice and the graphene lattice, the material and thickness of the barrier and other parameters affect the frequency of oscillation. Theoretical investigation of these devices will accelerate the realization of successful products, as well as highlighting the underlying physical principles such as quantum capacitance, an effect that is revealed due to the unique density of states of graphene.

This thesis comprises an additional five chapters that explore graphene resonant tunnel diodes. Chapter 2 provides an insight into the static $I(V)$ characteristics of a graphene-hBN-graphene device, obtained via the Bardeen Transfer Hamiltonian method. Factors affecting the lineshape and magnitude of the $I(V)$ characteristics, such as misalignment between graphene lattices and barrier thickness, are investigated in Chapter 3. The effect of the $I(V)$ characteristics on the dynamic behaviour of the device are then explored in Chapter 4. Here, the conditions for highest frequency oscillations and possible improvement are discussed. Chapter 5 investigates how the moiré pattern arising from the change in lattice size between the graphene and boron-nitride lattices affects the tunnelling process and $I(V)$ characteristics. The final chapter, Chapter 6, provides an overall conclusion to the work presented in this thesis, and discusses potential future avenues of research.

Chapter 2

Modelling

In this chapter, the Bardeen Transfer Hamiltonian method is outlined. This method allows calculation of the tunnel current through the barrier within a graphene-resonant tunnel diode, a schematic of which is seen in Fig. 2.1. This calculation can be performed either by considering a general lateral confinement, or, equivalently, by taking into account a scattering potential which allows scattering-assisted transitions as well as direct tunnelling. The later parts of the chapter introduce and analyze the electrostatics of the device.

2.1 Bardeen Transfer Hamiltonian Method

2.1.1 Calculating the Current

Derived from Fermi's golden rule, the Bardeen Transfer Hamiltonian method [65, 66] gives the current across the barrier, I_b. The method takes into account the availability of states for tunnelling, the availability of states to tunnel into, and energy conservation, giving:

$$I_b = g_s g_v e \sum_{\mathbf{k}_B, \mathbf{k}_T} \frac{1}{\tau_{B\to T}} f_B(E_B)[1 - f_T(E_T)] - \frac{1}{\tau_{T\to B}} f_T(E_T)[1 - f_B(E_B)]. \tag{2.1}$$

Here the summation is over all states in the bottom (B) and top (T) electrodes, with lateral wavevectors $\mathbf{k}_{B,T}$ measured relative to the position of the nearest Dirac point, $\mathbf{K}^{\pm}_{B,T}$, in the two graphene layers, see Fig. 2.2. $g_s = 2$ is the spin degeneracy, $g_v = 2$ is the valley degeneracy, and $\tau^{-1}_{B\to T}$

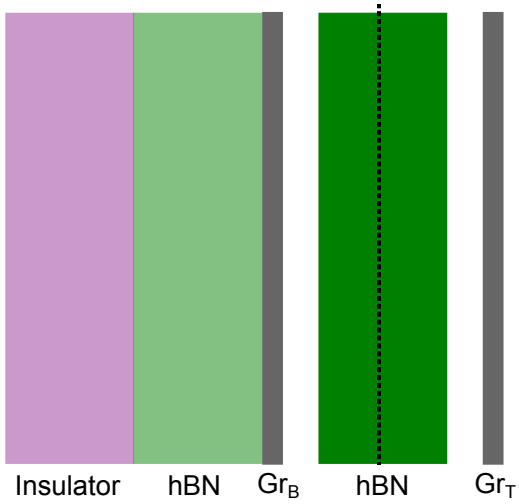

Figure 2.1: A schematic diagram of the layers within the device in the z-plane; the bottom insulating layer (purple), hBN (green) and graphene (grey). The surface integral in Eq. (2.2) is calculated for the $x-y$ surface located on the dashed line, half-way through the hBN tunnel barrier (dark green).

and $\tau_{T\to B}^{-1}$ are the tunnelling rates for electrons travelling from the bottom to top electrodes, and top to bottom electrodes, respectively. The Fermi function in each electrode is $f_B(E_{B,T}) = [1 + e^{(E_{B,T}-\mu_{B,T})\beta}]^{-1}$, with the electron energy $E_{B,T} = s_{B,T}\hbar v_F k_{B,T}$, $s_{B,T} = +1$ (-1) for electrons in the conduction (valence) band respectively, $\mu_{B,T}$ are the chemical potentials in each electrode, the thermal energy $\beta^{-1} = \kappa_B T_K$, and T_K is the temperature. The energy shift of the Dirac points with respect to each other due to the electrostatic field across the tunnel barrier is ϕ, as discussed in Section. 2.2. Note that simulations in this thesis are conducted in a low temperature regime, $T_K = 10$ K, so we can neglect the effect of phonon scattering. More generally, it has been shown that NDC is present in these devices up to room temperature [20], and the effect of phonon scattering remains small even at such temperature, due to the high phonon energy [64].

The tunnelling rates are given by Fermi's golden rule,

$$\begin{aligned}\frac{1}{\tau_{B\to T}} &= \frac{2\pi}{\hbar}|M_{BT}|^2\delta(E_B - E_T)\\ &= \frac{1}{\tau_{T\to B}}.\end{aligned}$$

The matrix element for the transition between electrodes is [54]:

$$M_{BT} = \frac{\hbar^2}{2m} \int dS \left({\psi^*}_B \frac{d\psi_T}{dz} - \psi_T \frac{d{\psi^*}_B}{dz} \right), \tag{2.2}$$

where $\psi_B(\mathbf{r}, z)$ and $\psi_T(\mathbf{r}, z)$ are the wavefunctions in the bottom and top electrodes, respectively, and m is the free electron mass. The integral is evaluated over a surface located half way between the electrodes, i.e. half way into the barrier, as seen in Fig. 2.1. Such a restriction can arise from the lateral extent of CVD graphene grains in electrodes, i.e. a 'structural coherence length', or from a scattering mechanism, which we discuss further in Section. 2.1.2. The tunnel current is thus:

$$I_b = \frac{8\pi e}{\hbar} \sum_{\mathbf{k}_B, \mathbf{k}_T} |M_{BT}|^2 [f_B(E_B) - f_T(E_T)] \delta(E_B - E_T). \tag{2.3}$$

The model assumes the wavefunction to be separable, with exponentially decaying z-components and lateral (x,y) components that have a Bloch form. For a state with wavevector $\mathbf{k}$, the wavefunction can be written as a linear superposition of Bloch states $\Psi_{j,\mathbf{k}}$, on two identical atoms (j=α, β) per unit cell [67],

$$\psi_k(\mathbf{r}, z) = \chi_\alpha(\mathbf{k}) \Psi_{\alpha,\mathbf{k}}(\mathbf{r}, z) + \chi_\beta(\mathbf{k}) \Psi_{\beta,\mathbf{k}}(\mathbf{r}, z), \tag{2.4}$$

where $\Psi_{j,\mathbf{k}}$ is of the Bloch form:

$$\Psi_{j,\mathbf{k}}(\mathbf{r}, z) = \frac{1}{\sqrt{A}} \exp(i\mathbf{k}.\mathbf{r}) u_{j\mathbf{k}}(\mathbf{r}) h(z). \tag{2.5}$$

Here, $u_{j\mathbf{k}}(\mathbf{r})$ is the cell-periodic part of the Bloch function in the graphene layer, and $h(z)$ describes the $z-$dependence of the electron wavefunction in the graphene and barrier layers. $h(z) = h_B(z) \approx \frac{1}{\sqrt{D}} e^{-\kappa(z+d)}$ in the bottom layer and $h(z) = h_T(z) \approx \frac{1}{\sqrt{D}} e^{\kappa(z)}$ in the top layer, where d is the distance between the electrodes, κ is the decay constant of the wavefunctions in the barrier (discussed further in Section 2.1.3), and D is a normalization constant comparable to the inter-planar separation in graphite.

This term will be further discussed in Section 2.1.3. As discussed in Chapter 1, within the tight-binding approximation, χ_j in Eq. (2.4) have the

well-known form:

$$\begin{bmatrix}\chi_\alpha\\ \chi_\beta\end{bmatrix} = \begin{bmatrix}1\\ \pm s e^{\pm i\phi}\end{bmatrix}, \tag{2.6}$$

where the upper (lower) sign is used for electrons in the band around the $\mathbf{K}^+(\mathbf{K}^-)$ point of the Brillouin zone, and $\phi = \arctan(k_y/k_x)$ specifies the orientation of the wavevector. When taking the overlap integral, all combinations of the basis functions, i.e. transitions between all atom sites and valleys, must be considered. However, for simplicity, in the following analysis, we only show explicitly the contribution to the matrix element due to the $j = \alpha$ parts of ψ_B and ψ_T. The cross terms are reintroduced later (Eq. (2.9)) and fully included in our numerical calculations. The matrix element thus becomes:

$$M_{\alpha\alpha} = \frac{\hbar^2}{2mA}\int dS e^{i(\mathbf{k_B}-\mathbf{k_T})\cdot\mathbf{r}}\times \left(u^*_{\alpha\mathbf{k_B}} h^*_B(z) u_{\alpha\mathbf{k_T}} \frac{h_T(z)}{dz} - u_{\alpha\mathbf{k_T}} h_T(z) u^*_{\alpha\mathbf{k_B}} \frac{h^*_B(z)}{dz}\right) \tag{2.7}$$

The periodic Bloch functions are localized around the basis atoms, and thus in the plane midway between the electrodes, the functions are spread out. Therefore, $u_{j\mathbf{k}}(\mathbf{r}, z)$ vary only weakly in $\mathbf{k}$, and the dependence does not greatly affect the integral. Assuming the $z-$dependent terms to be invariable over the surface, we arrive at the usual tunnelling form $2\kappa e^{-\kappa d}/D$. The form of this tunnelling term is further discussed in Section 2.1.3, where we confirm that the approximation is valid. We take $u_{\alpha\alpha}$ to have no dependence on $\mathbf{k_B}$ or $\mathbf{k_T}$, i.e. using an effective-mass approximation where the periodic functions are evaluated at the band extrema, however, we do find a dependence on misalignment angle between the two graphene layers, discussed in detail later in this Section. As the atoms in the unit cell are identical, $u_{\beta\beta} = u_{\alpha\alpha}$. $u_{\alpha\beta} = u_{\beta\alpha}$ and the ratio $u_{\alpha\alpha}/u_{\alpha\beta}$ is of order one. We can approximate the matrix element as,

$$\begin{aligned} M_{\alpha\alpha} &= \frac{\hbar^2}{2mA}\frac{\kappa e^{-\kappa d}}{D}\int dS e^{i(\mathbf{k_B}-\mathbf{k_T})\cdot\mathbf{r}}\left(u^*_{\alpha\mathbf{k_B}} u_{\alpha\mathbf{k_T}} + u_{\alpha\mathbf{k_T}} u^*_{\alpha\mathbf{k_B}}\right) \\ &\approx \frac{\hbar^2}{2mA}\frac{2\kappa e^{-\kappa d}}{D} u^2_{\alpha\alpha}\int dS e^{i(\mathbf{k_B}-\mathbf{k_T})\cdot\mathbf{r}}. \end{aligned} \tag{2.8}$$

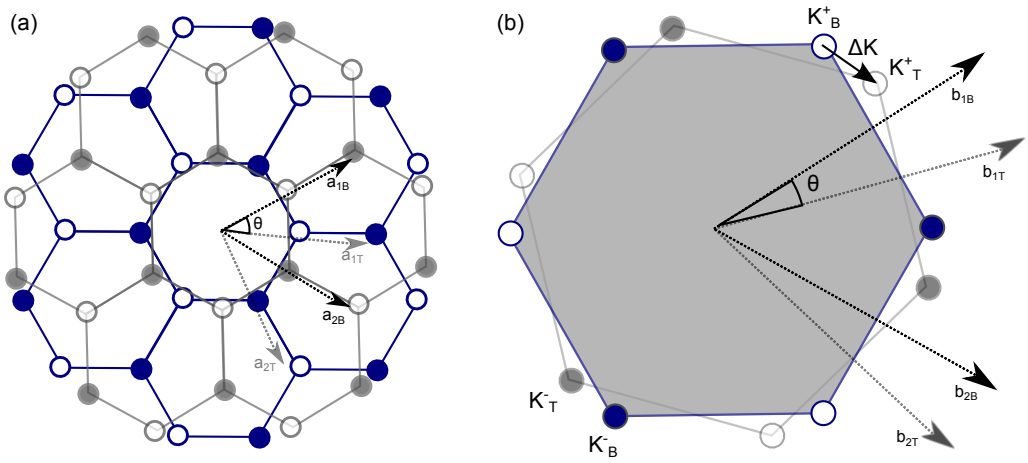

Figure 2.2: (a) Graphene lattice schematic in real-space of the bottom (navy) and top (grey) graphene electrodes. Filled (unfilled) circles represent carbon atoms on site α (β), $\mathbf{a}_{1B,2B}$ and $\mathbf{a}_{1T,2T}$ are the primitive lattice vectors in the bottom and top graphene electrodes respectively, and ω is the misalignment angle between the layers. (b) k-space schematic of the graphene lattices in the bottom (navy) and top (grey) electrodes, with the first Brillouin Zone of the bottom layer shaded in grey. $\mathbf{b}_{1B,2B}$ and $\mathbf{b}_{1T,2T}$ are the primitive reciprocal lattice vectors in the bottom and top electrodes,respectively. The inequivalent K^+ and K^- points are coloured white and black, respectively.

The crystalline lattices of the bottom and top graphene layers may be rotationally misaligned by an angle, θ, as seen in Fig. 2.2. Such a misalignment causes an equivalent rotation of the Brillouin zones in k-space such that the Dirac points in the two graphene layers no longer overlap. Even when the angle is very small, $\theta < 2°$, the misalignment of the cones is significant. The rotation matrix, $R(\theta)$, can be used to find a wavevector describing the displacement in $k-$space, $\mathbf{\Delta K} = (R(\theta)-\mathbb{1})\mathbf{K}^+$, which satisfies $\theta = 2\sin^{-1}(3a|\mathbf{\Delta K}|/8\pi)$ [68–71]. Therefore, the wavevector of an electron in the top graphene layer measured relative to the position of the Dirac point in the bottom layer becomes $\mathbf{k_T} + \mathbf{\Delta K}$ and the matrix element is now:

$$M_{BT} = \frac{\hbar^2\kappa}{mAD} e^{-\kappa d} g_\theta(\phi_B, \phi_T) \int dS e^{i\mathbf{\Delta K}\cdot\mathbf{r}} e^{i(\mathbf{k_B}-\mathbf{k_T})\cdot\mathbf{r}}, \tag{2.9}$$

where:

$$g_\theta(\phi_B, \phi_T) = u_{\alpha\alpha}^2 \left(1 + s_B s_T e^{-i(\phi_B \mp \phi_T)}\right) + u_{\alpha\beta}^2 \left(s_B e^{\pm i\phi_B} + s_T e^{\pm i\phi_T}\right). \tag{2.10}$$

Here the upper sign is for transitions between like valleys, i.e. $\mathbf{K}_B^\pm$ to $\mathbf{K}_T^\pm$, and

the lower sign is for transitions between unlike valleys, i.e. $\mathbf{K}_B^{\pm}$ to $\mathbf{K}_T^{\mp}$, and $\phi_T' = \phi_T + \omega$. Here, $s_{B,T} = \pm 1$ labels electrons in the conduction (valence) band, respectively, and $\phi_{B,T}$ specifies the orientation of the wavevector in each layer. The pseudospin of the electron wavefunctions is included in the function, $g_\theta(\phi_B, \phi_T)$, within the part of the matrix element and in the overlap of the periodic part of the wavefunctions, and as current from the $\mathbf{K}^-$ valley makes an equivalent contribution to the $\mathbf{K}^+$ valley. This factor can be written more simply as:

$$g(\phi_B, \phi_T) = 1 + s_B s_T e^{-i(\phi_B - \phi_T)} + s_B e^{i\phi_B} + s_T e^{-i\phi_T}, \tag{2.11}$$

where $g_\theta(\phi_B, \phi_T) = \gamma(\theta) g(\phi_B, \phi_T)$. The spatial overlap of the normalised cell-periodic part of the Bloch states, $u(\mathbf{r})$, at the Dirac points in the two electrodes is $\gamma(\theta)$ and is evaluated over an area, S_C, that greatly exceeds the length scale of the impurity potential, $\sim q_c^{-1}$, and can be written as:

$$\gamma(\theta) = \frac{1}{dS_C} \int_{S_C} dS_C u^*(R(\theta)\mathbf{r}) u(\mathbf{r}). \tag{2.12}$$

2.1.2 Scattering Potential Method

It is also possible to formulate an expression for the tunnel current by constructing a matrix element that describes a scattering process between the two electrodes,

$$M_{BT}^S = \int_\Omega d\Omega \psi_B^*(\mathbf{r}, z) V_S \psi_T(\mathbf{r}, z), \tag{2.13}$$

where the integral is over all space, Ω, and $V_S(\mathbf{r}, z)$ is a scattering potential that can induce transitions between states with mismatched in-plane wavevectors, as discussed further in Section 3.1.1. Although this form looks to be quite different from that in Eq. (2.2), it can be demonstrated that the methods are equivalent. In Ref. [52], Eq. (2.13) is evaluated to give:

$$M_{BT}^S = \frac{u_{\alpha\alpha}^2}{AD} e^{-\kappa d} e^{i(\phi_B - \phi_T + \theta)} \Xi \int dS e^{i\mathbf{\Delta K}\cdot r} e^{i(\mathbf{k_B} - \mathbf{k_T})\cdot r}. \tag{2.14}$$

If $\Xi = \hbar^2\kappa/2md$, Eq. (2.2) and Eq. (2.14) are identical. The scattering potential in Ref. [52] is assumed to be separable into components in the tunnelling direction and the plane parallel to the tunnelling direction, $V_S(\mathbf{r}, z) = V_S(z) V_S^{\parallel}(\mathbf{r})$. The factor $V_S(z)$ is assumed to be constant over the

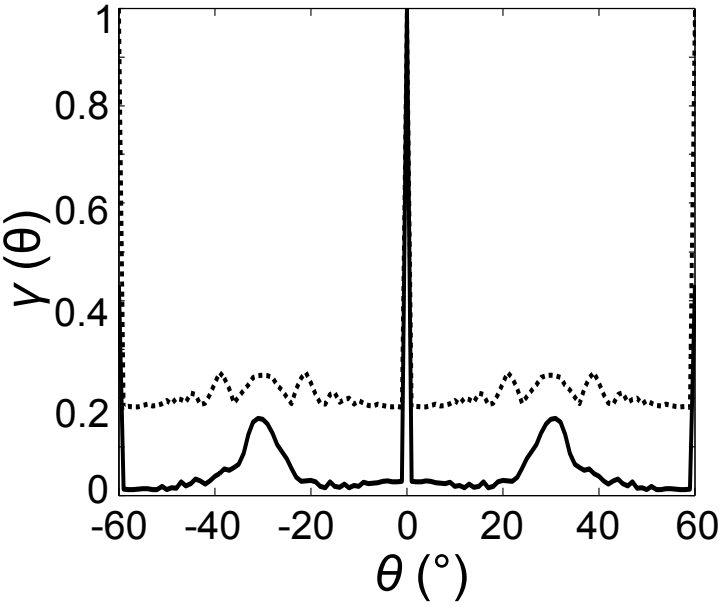

Figure 2.3: The function $|g(\phi_B, \phi_T, \theta)|$ calculated exactly by density functional theory by M. T. Greenaway (solid curve), and calculated approximately by evaluating the overlap of Gaussian functions placed on the lattice sites (dashed curve).

barrier region, and thus Ξ corresponds to $V_S(z) = \hbar^2\kappa/2md$. Inserting all matrix elements into the integral form of Eq. (2.3),

$$I_b = \frac{8\pi e}{\hbar^2 v_F} \int_{\mathbf{k}} |M_{BT}|^2 [f_B(E_B) - f_T(E_T)] d\mathbf{k}, \tag{2.15}$$

gives the current across the barrier.

This latter method is useful if a secondary source of scattering is involved, as the scattering potential can be altered accordingly. The distinction between the two methods is further discussed in [72]. It is concluded in [73] that the two methods are modelling the same aspect of the tunnelling process, which is a restriction in the lateral extent over which the wavefunctions maintain their coherence. We will consider the scattering potential method approach when discussing changes to the matrix element. Another equivalent method considers the dwell time of electrons in the graphene electrodes and in the barrier, and relates this time to an energy broadening for the tunnelling calculation.

2.1.3 Discussion of the Tunnelling Probability

Here, we discuss further the term describing the tunnelling across the barrier. The current will be proportional to a transmission probability $T \propto 1/\tau_{B\to T}$. If the tunnelling conductance per channel is much smaller than the conductivity quantum e^2/h, which is true for this case, T will be exponentially small and depend strongly on the energy, E, of the tunnelling electrons, i.e.

$$T(E) = A(E)\exp([-W(E)]), \tag{2.16}$$

where $A(E)$ is a function that depends on the wavefunction matching at the interface [51]. We assume $A(E)$ is constant here and investigate the form of $W(E)$. For an isotropic barrier, we can solve the dispersion relation $E = \epsilon_n(k_x, k_y, k_z)$, where E is the energy of the electrons tunnelling in the z direction, and ϵ_n is the energy each band ($n = 0$ for the conduction band, $n = 1$ for the valence band). The tunnelling probability depends primarily on k_z, as tunnelling through the barrier is in the z-direction, and as no real solution can exist within the barrier, must be imaginary, therefore:

$$W(E) = 2d\mathrm{Im}(k_z). \tag{2.17}$$

For the case of parabolic bands within the barrier, the dispersion relation for the electron is given by:

$$\Delta = \frac{\hbar^2 k^2}{2m^*}, \tag{2.18}$$

where Δ is the barrier height, i.e. the distance to the valence band in our case, and m^* is the effective mass of the electron in the barrier, and thus:

$$\mathrm{Im}(k_z) = \frac{\sqrt{2m^*\Delta}}{\hbar}. \tag{2.19}$$

For layered crystals, the band structure can be approximated as:

$$E = \tau(k_z) + \epsilon_1(k_x, k_y), \tag{2.20}$$

where $\tau(k_z) = 2t_\perp \cos(k_z d_i)$, where $t_\perp > 0$ describes the interlayer coupling, and d_i is the interlayer distance ($d_i \approx 3.4$Å for hBN). Inserting this into the

tunnelling equation gives k_z within the gap to be

$$k_z = \frac{i}{d_i} ln \left(\frac{|E - \epsilon_1|}{2t_\perp} + \sqrt{\left(\frac{E - \epsilon_1}{2t_\perp} \right)^2 - 1} \right). \tag{2.21}$$

At the top of the valence band, $E_{max} = \max(\epsilon_1(k_x, k_y)) + 2t_\perp$, which gives a wavevector of:

$$\mathrm{Im}(k_z) = \frac{1}{d_i} \ln\big(|\frac{\Delta}{2t_\perp} + 1| + \sqrt{(\frac{\Delta}{2t_\perp + 1})^2 - 1} \big), \tag{2.22}$$

where $\Delta = E - E_{max}$. If $\Delta >> 2t_\perp$, this can be simplified to $\mathrm{Im}(k_z) = \frac{1}{d_i} \ln(\frac{\Delta}{t_\perp})$, which gives a tunnelling probability $T \propto (t_\perp/\Delta)^{2N_L}$, where $N_L = d/d_i$ is the number of atomic layers making up the tunnel barrier. If $\Delta << 2t_\perp$, $\mathrm{Im}(k_z) = \frac{1}{d_i} \sqrt{\frac{\Delta}{t_\perp}} = \frac{\sqrt{2m^* \Delta}}{\hbar}$, where $m^* = \frac{\hbar^2}{2t_\perp d_i^2}$ is the effective mass in the tunnelling direction. Therefore, as long as the tunnelling occurs near the band gap edge, the standard isotropic model is applicable.

Further models considering a more complicated dispersion relation, which allows the inclusion of factors such as the stacking formation, have been studied [51]. Each of these shows that the parabolic approximation for the energy bands of hBN works well. This ties in well with the matrix element, which, when incorporated into the equations for current, gives a factor of $\exp(2\kappa d)$ in the current.

2.2 Electrostatics of a Two-Layer Graphene Device

Now that the current across the barrier can be calculated, we can explore the electrostatics of the graphene-hBN-graphene device. Two voltages can be applied to the device; a gate voltage, V_g, and a bias voltage, V_b, as seen in Fig. 2.4, with the bottom graphene electrode as the ground. These will control the induced carrier densities, n_B and n_T, in the bottom and top graphene electrodes, respectively. We define $n_{B,T} > 0$ for holes and $n_{B,T} < 0$ for electrons, i.e. in the figure, $n_B < 0$ and $n_T > 0$. The electronic charge is also defined as $e > 0$. In the absence of applied voltages, $n_B = n_T = 0$, and the chemical potentials in each layer, μ_B and μ_T, are at the neutrality

(Dirac) point.

The gate voltage is applied between the Si substrate and the bottom graphene layer, and increases the carrier concentration in the bottom electrode, n_B. Due to the low density of states close to the Dirac point and the weak screening in monolayer graphene [67], the bottom graphene electrode only partially screens the charge, and resulting electric field, F_g, induced on the Si-gate electrode by V_g. Therefore, the carrier density in the top electrode, n_T, is also influenced by V_g, when the chemical potential is close to the Dirac point [51]. This behaviour is associated with the so-called quantum capacitance [74], discussed further in Section 3.7 which is an effect relatively unnoticed in traditional semiconductors but shows up strongly in graphene, where a relatively small V_g induces a significant change in the chemical potential, μ_B, thus providing additional control of the effective barrier height and the transmission coefficient.

The bias voltage is applied between the two graphene layers, and gives rise to the tunnel current through the barrier. The electric field induced across the barrier, F_b, and the external electric field from the gate voltage, F_g, can be related to the charge densities via Gauss's Law. For a field, $\mathbf{F}$ and charge (carrier density), ρ (n), Gauss's Law is:

$$\nabla \cdot \mathbf{F} = \frac{\rho}{\epsilon} = \frac{ne}{\epsilon}. \tag{2.23}$$

For our system, this gives:

$$\epsilon(F_b - F_g) = (n_B - n_B^D)e, \tag{2.24}$$

$$\epsilon(0 - F_b) = (n_T - n_T^D)e, \tag{2.25}$$

where n_B^D and n_T^D are the doping levels in each layer, and $\epsilon = \epsilon_0\epsilon_r$ and ϵ_r (ϵ_0) are the relative (absolute) permittivies. For hBN, $\epsilon_r = 3.9$. The field across the barrier, F_b, is defined as negative as it shifts the top Dirac cone down with respect to the bottom Dirac cone, which has a neutrality point centered at $E = 0$, whilst F_g has an opposing effect and is therefore positive. For the case of chemically undoped graphene layers, i.e. $n_B^D = n_T^D = 0$, which, to a good approximation, is the case in the currently-fabricated devices, μ_B and

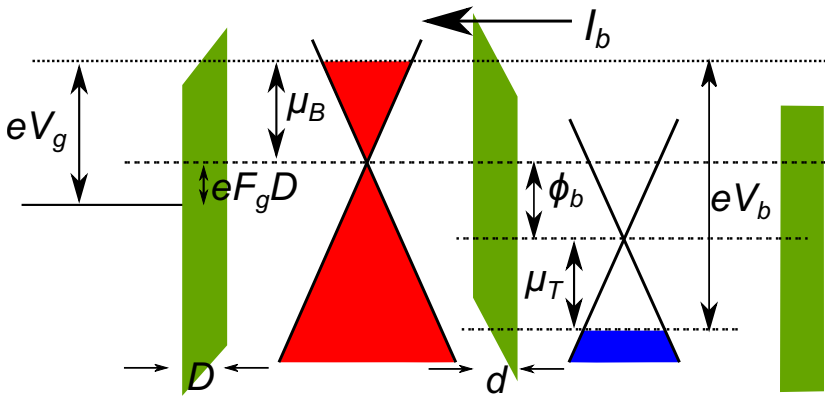

Figure 2.4: Electrostatic diagram of the device, showing the bottom graphene electrode with filled states (red) up to the chemical potential, μ_B, and the top graphene electrode with filled states (blue) up to μ_T. The hBN barrier (central green layer) separates the two electrodes. Current, I_b, flows from right to left here. The voltage dropped across the device, eV_b, and the voltage shifts due to the resulting gate field, eF_gD, and the field across the barrier, ϕ_b, are shown.

μ_T are related by:

$$eV_b = \mu_B(n_B) - \mu_T(n_T) - eF_b d, \tag{2.26}$$

where d is the thickness of the barrier. The chemical potentials have the opposite sign to the carrier densities so that, for the case of Fig. 2.4, μ_B is positive and μ_T is negative. For simplicity, we assume the graphene electrodes are chemically undoped, unless otherwise stated. For energies within the linear dispersion curve of graphene, the Fermi level in the two electrodes is defined as:

$$\mu(n) = -\mathrm{sgn}(n)\sqrt{\pi|n|\hbar^2 v_F^2}, \tag{2.27}$$

where sgn(n) is the sign function, i.e. +1 for $n > 0$ and -1 for $n < 0$. From the coupled Poisson's equations, we can write n_T in terms of n_B,

$$n_T = -(n_B - n_B^D) - \frac{F_g\epsilon}{e} + n_T^D, \tag{2.28}$$

which can be inserted into Eq. (2.26) to give an equation in terms of either

n_B or n_T. The field, F_g, due to the gate voltage, V_g, is defined by:

$$eV_g = \mu_B(n_B) + eF_gD, \tag{2.29}$$

giving

$$n_T = -(n_B - n_B^D) - \frac{\epsilon}{e^2}(\frac{eV_g - \mu_B}{D}) + n_T^D. \tag{2.30}$$

In order to calculate the carrier densities, a shooting method, in which an initial range of n_B is trialed, can then be used to minimise:

$$0 = eV_b - \mu_B(n_B) + \mu_T(n_T) - \frac{e^2(n_T - n_T^D)d}{\epsilon}, \tag{2.31}$$

giving n_B and, thus, n_T. Fig. 2.5(a) shows the calculated charge densities vs V_b for a device with $V_g = 0$ (solid lines; red for the bottom layer, blue for the top layer). We see that as V_b increases, the number of electrons in the bottom cone, and the number of holes in the top cone, increase parabolically, and at $V_b = 0$, $n_B = n_T = 0$. For $V_g \neq 0$ (dashed lines in Fig. 2.5), at $V_b = 0$, the charge densities are nonzero due to the charge induced by the gate voltage. At higher V_b, the charge densities then follow the same parabolic behaviour, but shifted to have more (fewer) electrons (holes) on the bottom (top) graphene layer. The chemical potentials are also plotted in Fig. 2.5(b), where $\mu_T' = \mu_T - eF_bd$ is the chemical potential in the top layer with respect to the Dirac point of the bottom layer. The effect of applying a gate voltage can be seen to increase the chemical potential in the bottom electrode and decrease it in the top layer.

2.3 Comparison with Conventional RTDs

Resonant tunnelling and negative differential resistance have been studied extensively in double barrier resonant tunnelling diodes (DBRTDs) [75, 76]. As seen in Section 1.3.2, the DBRTD consists of a central well surrounded by two barriers. Charge build up in the well leads to a delay in current with respect to voltage changes, which can be represented as an inductance. This effective inductance, an important feature in the operation of double-barrier RTD oscillators, is absent in our single barrier device, which means that graphene-based oscillators are potentially faster. The quantum well

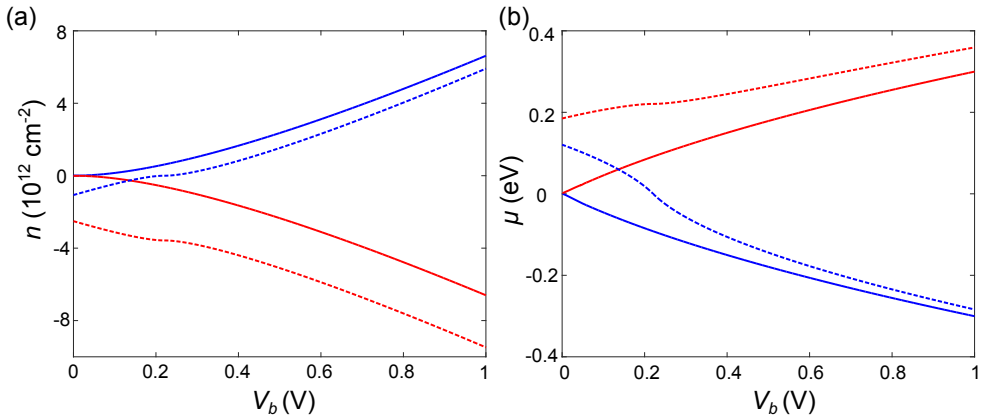

Figure 2.5: (a) Charge densities, n_B (red) and n_T (blue), in the bottom and top electrodes calculated respectively for aligned devices with four hBN layers acting as the barrier, for $V_g = 0$ V (solid lines) and $V_g = 50$ V (dashed lines). When $n_B < 0$, the conduction band of the Dirac cone is filling with electrons, whilst $n_T > 0$ represents electrons being lost from the valence band in the top Dirac cone. (b) Chemical potentials, μ_B (red) and μ_T (blue), in the bottom and top electrodes respectively for aligned devices with four hBN layers acting as the barrier, for $V_g = 0$ V (solid lines) and $V_g = 50$ V (dashed lines). When $\mu_B > 0$, the conduction band of the Dirac cone is filling with electrons and thus shifting the Fermi level up, whilst for $\mu_T > 0$, electrons are lost from the valence band in the top cone.

confinement provided by the two barriers creates quasi-two-dimensional states through which charged carriers can tunnel when their energy is tuned to resonance by an applied voltage. Such confinement is already built into a single sheet of graphene, thus the resonant tunnelling diode can be constructed by sandwiching a single tunnel barrier between two graphene electrodes. A fundamental intrinsic limitation on the frequency of DBRTDs is the carrier dwell time within the central quantum well ($\sim$ picoseconds). In the GRTD, without the quantum well, the limitation is set by the time to transit the barrier ($\sim$ femtoseconds). This, coupled with the high mobility of carriers in the graphene electrodes, and the atomically thin barrier, suggests great potential for future high-speed electronics, potentially operating in the THz regime. Present day DBRTDs are well optimised, whereas GRTDs are still in the primary stages of design. One particular benefit highlighted so far is the room-temperature operation, alongside the motivation to harness fundamental physical principles arising from graphene's unique properties. We investigate and quantify theses benefits in Chapters 3 and 4.

Chapter 3

DC Characteristics

In this chapter, we describe the general behaviour and physics behind the $I_b(V_b)$ characteristics of the graphene-hBN-graphene heterostructure and compare our calculations to experiment. We then investigate the device parameters that affect the shape of the current-voltage curves to determine the parameter set which will give rise to an optimum high-frequency response. The parameters we investigate include the tunnel barrier width, chemical doping levels of each electrode, and the alignment of the graphene lattices. It is found that reducing the barrier width to a minimum, i.e. a single atomic plane of barrier material, selecting a barrier material with an optimum potential height, applying a high level of chemical doping to an electrode and aligning the graphene layers leads to the highest-frequency oscillations and ensures high current output.

3.1 Electron Tunnelling between Aligned Graphene Electrodes

In Fig. 3.1, we show a typical $I_b(V_b)$ curve calculated for the graphene resonant tunnelling diode (GRTD) and the band diagrams (insets) for the bottom (left) and top (right) electrodes for two values of V_b. The curve is calculated for graphene layers that are undoped. At zero applied bias, and with zero gate voltage, i.e. $V_b = V_g = 0$, the Dirac points in the top and bottom layers are energetically aligned, and the chemical potentials in both layers, μ_B and μ_T, are at the neutrality point, i.e. $\mu_B = \mu_T = 0$, as in the lower inset of Fig. 3.1. If a positive bias voltage is applied between the two layers, $V_b > 0$, electrons accumulate in the bottom (negatively-biased)

layer, and an equal number of holes accumulate in the top (positively-biased) electrode. This difference in charge on the two electrodes, see Fig. 2.5, induces an electric field across the barrier, F_b, which leads to an electrostatic energy difference between the two layers of $\phi = eF_b d$, and, consequently, produces a relative energetic misalignment of the cones in the two layers. This shift means that most available carriers tunnelling from one electrode to the other must change their in-plane wavevector $\mathbf{k}$ in order to tunnel with conservation of energy. This type of transition is forbidden unless the tunnelling event is accompanied by a scattering process in which the conservation of $\mathbf{k}$ is relaxed. This long-range (in real-space) scattering process can arise from disorder and interaction effects and their effects are further discussed in Section 3.1.1.

3.1.1 Elastic Scattering

The resonant feature of the $I_b(V_b)$ characteristics has a line width and position that depends on the disorder potential or the nature of the interaction leading to elastic scattering processes. A scattering potential,

$$V_S(\mathbf{q}) = \frac{V_0}{(q_c^2 + \mathbf{q}^2)}, \tag{3.1}$$

is used in our model to describe the tunnelling-induced change in in-plane wavevector, $\mathbf{q} = \mathbf{k_B} - \mathbf{k_T}$, between the graphene layers. This scattering potential is taken to be localized over the region of the tunnel barrier. In Eq. (3.1), $\mathbf{q_c}^{-1}$ is the lower limit of the modulation length of the scattering potential in real space, and $V_s(\mathbf{q})$ has a Lorentzian form. This potential can arise due to disorder in the system and impurities in the layers, and possibly from the misalignment of the barrier and graphene layers. Random impurities automatically introduce a correlation length, $r_0 < r_i = 1/(\pi n_i)^2$, where r_i and n_i are the radius and the number density of the impurities [77]. It follows from Eq. (3.1) that $V_S(\mathbf{q})$ is maximal when the Dirac points and the electronic spectra of the two graphene electrodes are aligned energetically, i.e. $\mathbf{q} = 0$, thus allowing electrons to tunnel resonantly. The choice of V_0 and q_c will be discussed below. If we set $V_S(\mathbf{r}) = 1$, i.e. all transitions are allowed and $q_c^{-1} = 0$ nm, the tunnel current increases monotonically with increasing V_b and there is no resonant peak, for the aligned device, as seen in the green curve of Fig. 3.2. It is found that

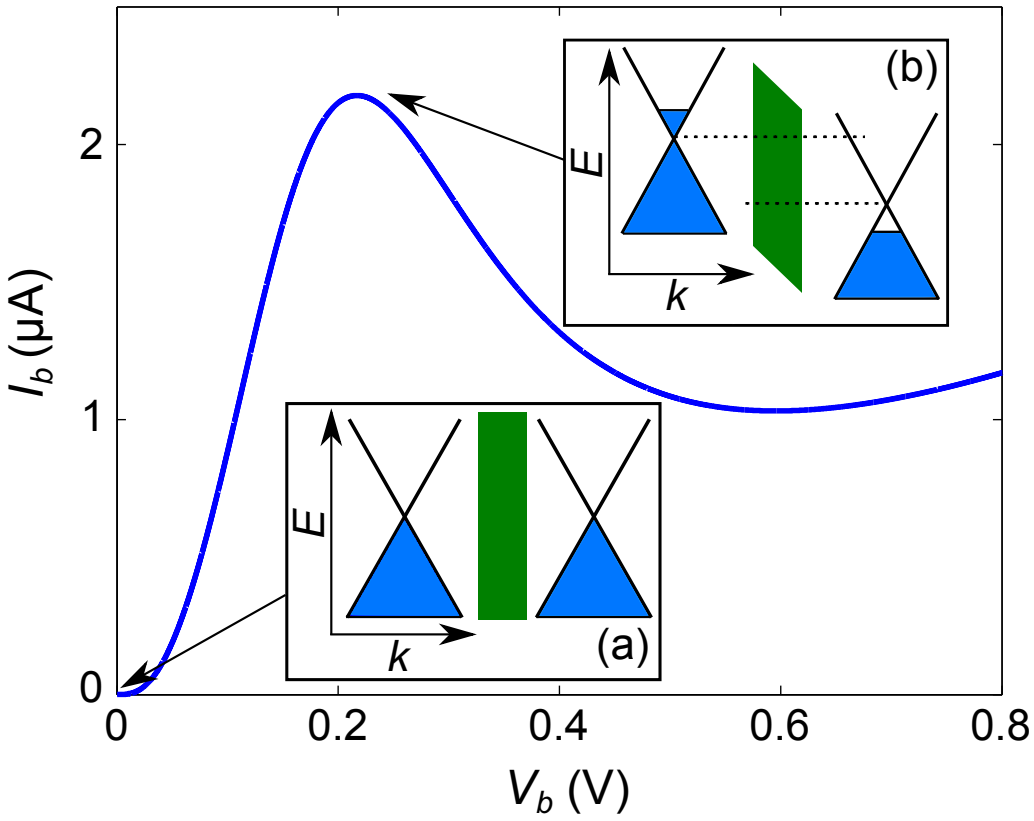

Figure 3.1: A general $I_b(V_b)$ characteristic calculated for the graphene-hBN-graphene diode. Insets(a-b): Band diagrams ($E-k$) of Dirac cones (displaced for clarity) of the bottom (left in (a) and (b)) and top (right in (a) and (b)) layers, with blue representing the filling of the cones with electrons, separated by a hBN barrier (green). Initially, at $V_b = 0$ (a), both cones are filled to the neutrality point. At $V_b > 0$, the bottom cone is filled above the neutrality point, whereas the top cone loses valence electrons. The Dirac cones are shifted in energy with respect to each other by the electric field induced across the barrier, which causes the barrier potential to become tilted. This curve is a result of simulations of a device comprises 4 hBN layers as the tunnel barrier, and with aligned graphene layers ($\theta = 0°$).

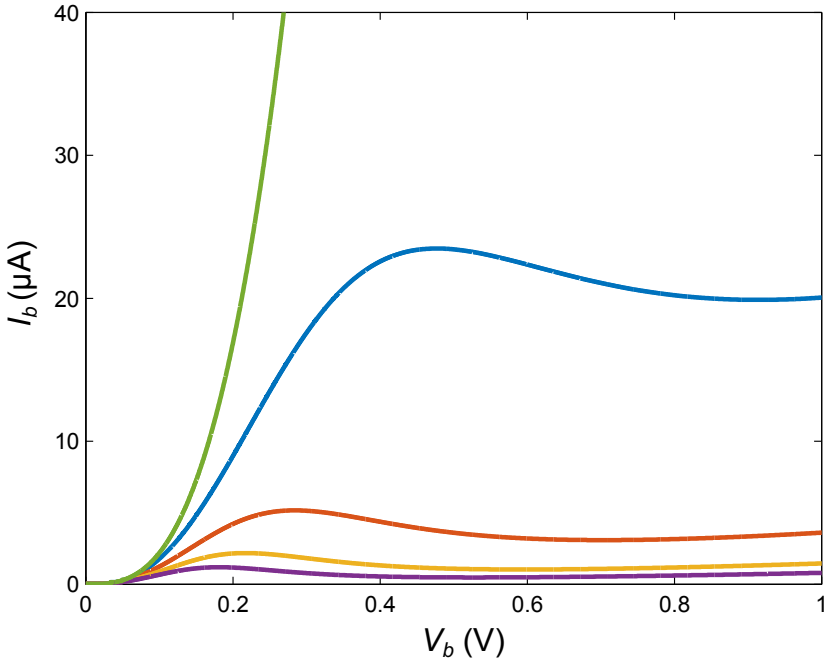

Figure 3.2: $I_b(V_b)$ characteristics for $q_c^{-1} = 0$ nm (green), $q_c^{-1} = 5$ nm (blue), 10 nm (red), 15 nm (orange), and 20 nm (purple). Increasing q_c broadens the $I_b(V_b)$ characteristics. We find $q_c^{-1} = 15$ nm best fits the experimental measurements, and matches the peak and valley magnitude and position. All curves are for a $\theta = 0°$ device.

decreasing the length scale of the scattering potential, i.e. q_c^{-1}, broadens the $I_b(V_b)$ characteristics, as seen in Fig. 3.2, where characteristics for $q_c^{-1} =$ 5 nm (blue) to $q_c^{-1} = 20$ nm (purple) are shown. The current peak shifts to higher V_b and higher current magnitudes for increasing q_c. The NDC region approximately corresponds to $V_b \sim \hbar v_F q_c/e$, where the average in-plane change in wavevector, q, approaches q_c. Experimentally, the $I_b(V_b)$ characteristics, including the strong resonant peak and NDC region, persist up to room temperature. Thus, we can conclude that the scattering is primarily elastic as there is a negligible change in the $I_b(V_b)$ characteristics when the temperature, T_K, is increased up to 300 K, as seen in Fig. 3.3, indicating a lack of phonon-assisted tunnelling. We note the $q_c^{-1} = 0$ nm case, i.e. $\delta-$function scattering, gives a similar result to Ref. [51], where many different impurities and length scales were involved, thus most transitions were allowed.

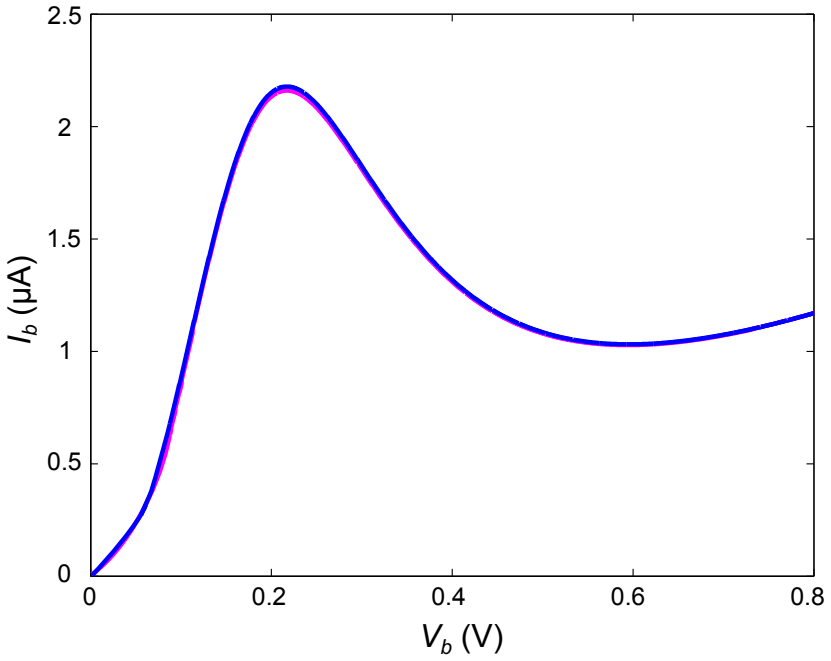

Figure 3.3: $I_b(V_b)$ characteristics for a device with $N_L = 4$ and $\theta = 0°$ for $T_K = 10$ K (blue) and $T_K = 300$ K (magenta), $q_c^{-1} = 15$ nm, neglecting phonon-processes.

3.1.2 General Description of $I_b(V_b)$ Characteristics ($\theta = 0°$)

Initially, for small V_b, increasing V_b causes the current flowing across the barrier to also increase (Fig. 3.1), thus the device exhibits typical Ohmic-like behaviour. This is because ϕ is initially small and the Dirac cones in the top and bottom layers are closely aligned in energy. As V_b increases, the magnitude of the chemical potentials in the two layers increases, increasing the number of states that are available to tunnel. Although the states in the bottom and top electrodes are no longer energetically aligned, the change in $\mathbf{k}$ required for the tunnelling process to occur is well within the elastic scattering regime. At the peak in current, I_{peak}, the resonant condition $\phi = \hbar v_F |\Delta \mathbf{K}|$ is met. As this occurs when the chemical potentials are high up in the linear dispersion curve, this is the V_b value at which the largest number of electrons can tunnel through the barrier, via elastic scattering. The band diagrams, with μ_B and μ_T (marked by the upper edges of the blue filled regions) are shown in the upper inset of Fig. 3.1. Note, the two Dirac cones are displaced horizontally for visual effect only, as for a $\theta = 0°$ device, the cones would completely overlap in k-space. Once the bias voltage is increased beyond this point, the energetic misalignment of the Dirac

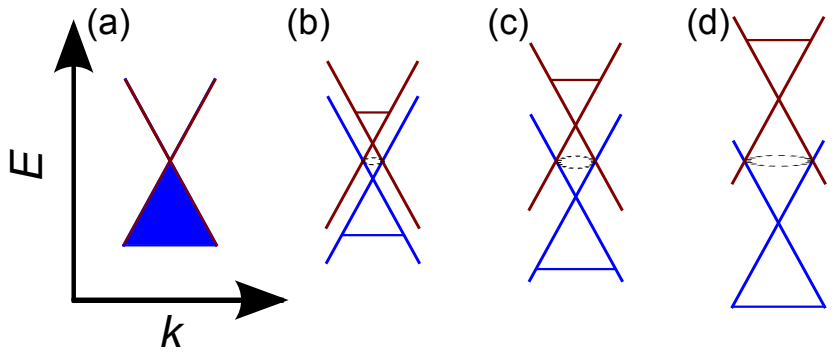

Figure 3.4: Band diagrams ($E - k$) of the bottom (red) and top (blue) Dirac cones for (a) $V_b = 0$ and (b-d) increasing $V_b > 0$, for an aligned device. The Dirac cones completely overlap each other in the tunnelling direction when $V_b = 0$, as in (a). The application of a bias voltage shifts the cones energetically with respect to each other. The black dashed curve in (b-d) represents the 3D energy slice of the intersecting cones. It is unique to the $\theta = 0°$ case to have a circle for each E.

(neutrality) points due to the field across the barrier becomes large, and most transitions require a large $\mathbf{k}$ change in order to tunnel, which cannot be provided by the scattering potential. Thus, at this point, an increase in voltage leads to a decrease in current through the barrier, despite an increase in the number of states available to tunnel. This region, seen in Fig. 3.1 between $V_b = 0.25$ V and $V_b = 0.6$ V, is known as a region of negative differential conductance (NDC). In this range of V_b, the device is unstable if placed in a resonant circuit, which is known to lead to self-sustained current oscillations [76]. After $V_b = 0.6$ V, another Ohmic-like positive differential conductance (PDC) region occurs, as despite the large energetic displacement of the Dirac cones, there are many states available to tunnel, and the current continues to increase with increasing V_b.

Fig. 3.4(a-d) show plots of the dispersion relations in the two electrodes in k-space. When the lattices of the graphene electrodes are aligned, the Dirac points of the two layers are at the same point in k-space. Thus, when $V_b = 0$ V, we see that the band diagrams overlap completely in the tunnelling direction, and both the bottom (red) and top (blue) Dirac cones are filled with electrons to the neutrality point. Fig. 3.4(b-d) show the change in chemical potentials and overlap with increasing V_b. We see that any electron tunnelling at a particular energy E between the Dirac points of the two cones, will be able to tunnel to all available states on that energy contour, for example, the black ring in (b-d).

Eq. (2.15) from the Bardeen Transfer Hamiltonian method can also be

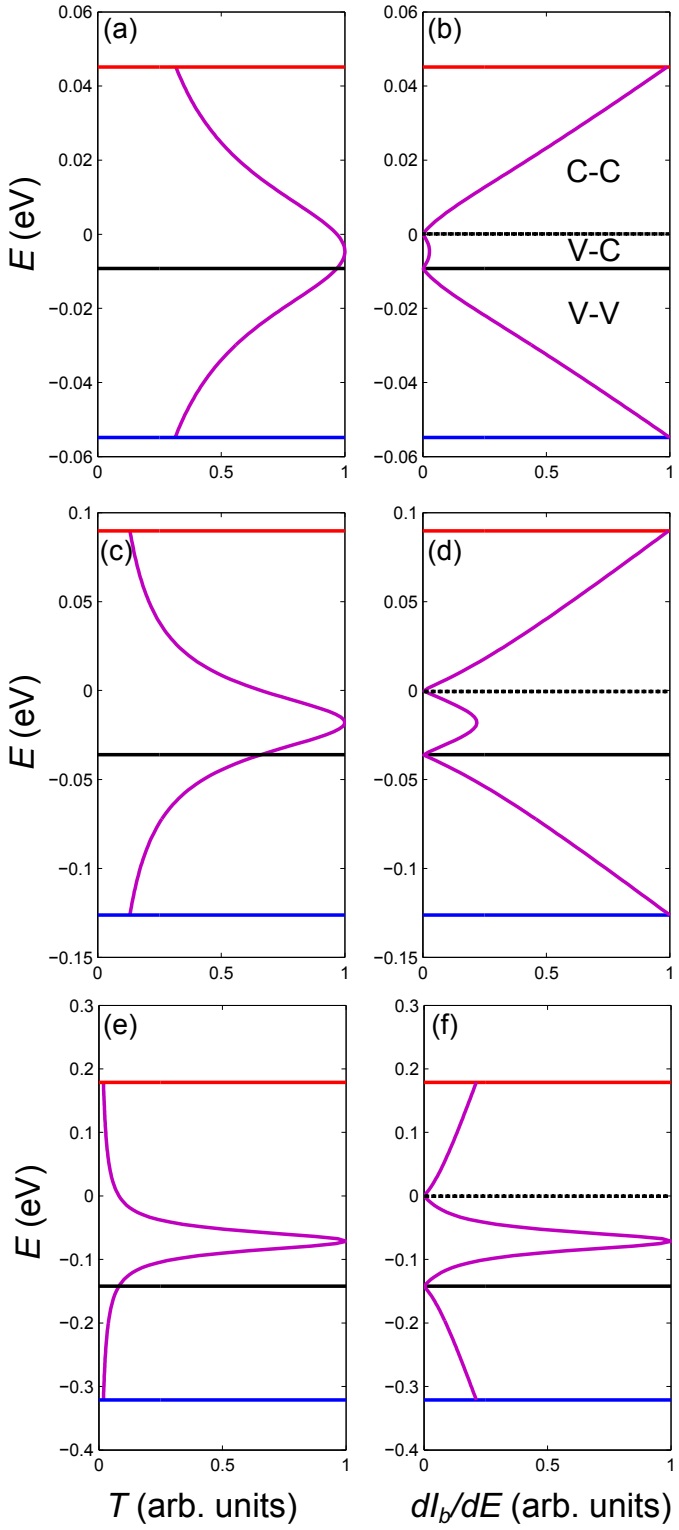

Figure 3.5: $T(E)$ (a,c,e) and $T(E)DoS_B(E)DoS_T(E)$ (b,d,f) for three points on the $I_b(V_b)$ curve in Fig.3.1; (a,b): 0.1 V, i.e. in the first PDC region, (c,d): 0.22 V, i.e. the current peak, and (e,f): 0.5 V, i.e. the valley. Here, we see the trade-off between momentum conservation and the linear density of states. The red (blue) line represents $\mu_B(\mu_T)$ and the solid black line represents the position of the Dirac point in the top cone, with respect to the Dirac point of the bottom cone (dashed black line), which is at $E = 0$ eV. Three different regimes of tunnelling (labelled C-C, V-C and V-V) are shown in (b) and explained in the text ($\theta = 0°$).

written as

$$I_b(V_b) \propto \int dE D_B D_T T(E)[f(E_B) - f(E_T)], \tag{3.2}$$

where $D_{B,T}$ is the density of states in each layer, $T(E)$ is the tunnelling coefficient which relates to the probability of an electron with energy E in the bottom graphene electrode tunnelling to an empty state in the top electrode. Integrating the density of states (DoS) over energy provides the number of available states in the bottom electrode available for tunnelling, and the number of states available to tunnel into in the top electrode. Tunnelling will only occur when an electron occupying the state at energy E in the bottom electrode, i.e. $f(E_B) = 1$, can tunnel into an empty state at energy E in the top electrode, i.e. $f(E_T) = 0$. Note, it is also possible to have current in the reverse direction if $f(E_B) = 0$ is combined with $f(E_T) = 1$, i.e. an electron in the top electrode tunnelling into an empty state in the bottom electrode. The tunnelling coefficient multiplied by the DoS in the bottom and top electrodes provides dI_b/dE, i.e. the contribution to the total current from electrons with energy E.

Fig. 3.5 shows the tunnelling coefficient $T(E)$ and dI_b/dE, between the chemical potentials in the bottom (red line) and top (blue line) graphene electrodes, for three different points on the $I_b(V_b)$ curve. We see that the linear DoS has a large influence when the current is low, because here most of the states are aligned within the elastic scattering regime and thus the number of states available determines the current. For higher V_b, the conservation of momentum dominates and we see only a small change between (e) and (f) around the Dirac points of the bottom ($E = 0$) and top (black line) electrodes. In (b), the three regimes of tunnelling are highlighted; conduction band to conduction band (C-C), valence band to conduction band (V-C) and valence band to valence band (V-V). Before the current peak, as in (b), the current is dominated by the C-C and V-V (alike) band transitions. This is due to the low energy shift between the cones as in Fig. 3.4(b), where most of the Dirac cone overlap is occuring between like bands. At higher V_b, the cones are shifted further in energy, as in Fig 3.4(c,d), and thus the transitions between unlike bands dominate. In this case, electrons tunnel from the valence band of the bottom electrode into the conduction band of the top electrode.

The effect of chirality, discussed in Section 1.4.4, can be uniquely observed

within graphene devices. In the $I_b(V_b)$ characteristics in Fig. 3.6, the curves are calculated with (blue) and without (magenta) the inclusion of chirality. Due to the unique band structure of graphene, in which the energy falls linearly to zero at the Dirac point, the effect of chirality can be uniquely observed. In gapped semiconductors, the chirality in the bands is mixed, and thus the effect cannot be observed. Transitions for bias voltages preceding the resonant peak are dominated by transitions between alike bands and therefore current is enhanced compared to a non-chiral electron case. This causes the current peak to be larger for the chiral case. However, increasing the bias voltage beyond the resonant peak induces a change to transitions between unlike bands, as in Fig. 3.3(c), which suppresses the current, and thus leads to a lower valley current. Consequently, the effect of chirality increases the peak-to-valley ratio (PVR), which determines the power output of the device once it stabilizes, as the output current fluctuates between the peak and valley currents, and should thus be maximized. We can see from Fig. 3.6 that the effect of chirality is more prominent in aligned devices, as shown in (a), as opposed to the $\theta = 0.9°$ device in (b). This is because, for aligned devices, $\gamma(\theta)$ and thus $g(\phi_B, \phi_T, \theta)$ increase, as seen in Eq. (2.10).

Fig. 3.7 shows the effect of chirality at high V_b for the aligned (a,b) and misaligned (c,d) device. We see that in both cases, the tunnelling between like bands is enhanced by the effect of chirality and the tunnelling between unlike bands is decreased. The enhancing effect is more pronounced in the aligned sample, whereas the suppressing effect is more pronounced in the misaligned sample, due to the initial contributions from each type of tunnelling.

3.2 General Description of $I_b(V_b)$ Characteristics ($\theta \neq 0°$)

During preparation of the devices, which are fabricated using the standard dry-transfer procedure [79], care is taken to align the crystalline lattices of the graphene layers physically and angles of $\theta < 2°$ have been achieved. Even better alignment could be reached by using novel preparation techniques such as growth by molecular beam epitaxy (MBE). This could potentially allow devices with $\theta = 0°$ to be produced consistently. It is clear from the Transfer Hamiltonian method that aligning the layers will lead to a much

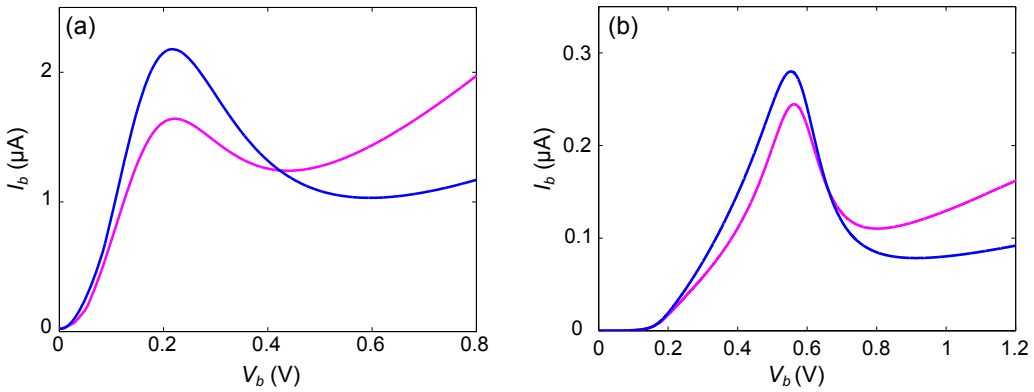

Figure 3.6: $I_b(V_b)$ characteristic calculated for the graphene-hBN-graphene diode with the chirality term included (blue) and with the chirality not included, i.e. $g = 4$ for the pseudospin and valley degeneracy, (magenta), for (a) a device with θ= 0° and (b) a device with θ= 0.9°.

higher magnitude of the tunnel current through the increase in the overlap integral, $\gamma(\theta)$, yet the general dependence on V_b will remain the same.

For non-zero misalignment angles where $\Delta K \neq 0$, it is clear from Eq. (2.13) that the matrix element is maximal when $\mathbf{q} - \Delta\mathbf{K}^{\pm} = 0$, which, as the misalignment angle approaches 1°, occurs for the highest number of states when $eF_bd = \pm\hbar v_F \Delta K$ [20]. Therefore, the position of the current peak increases in V_b as the misalignment angle increases. We also find that the peak-to-valley ratio (PVR) of the $I_b(V_b)$ curve increases with increasing θ converging to a value of 2.4 as θ approaches 2°. This is because, at higher θ, the overlap region of the tunnelling states occurs higher (lower) up in the conduction (valence) band where there is a larger number of states energetically aligned. However, we also find that the peak current amplitude decreases as θ increases due to the misorientation of the spatial parts of the wavefunction. This reduction in overlap can be seen in Fig. 3.8 and Fig. 3.9.

Each intersection point for each energy, as seen in Fig. 3.10, $\mathbf{I}(x(E), y(E))$, can be determined by combining the energy and momentum conserving equations:

$$s_B\hbar v_F|k_B| - \phi - s_T\hbar v_F|k_T| = 0 \tag{3.3}$$

$$k_T = k_B - \Delta\mathbf{K}, \tag{3.4}$$

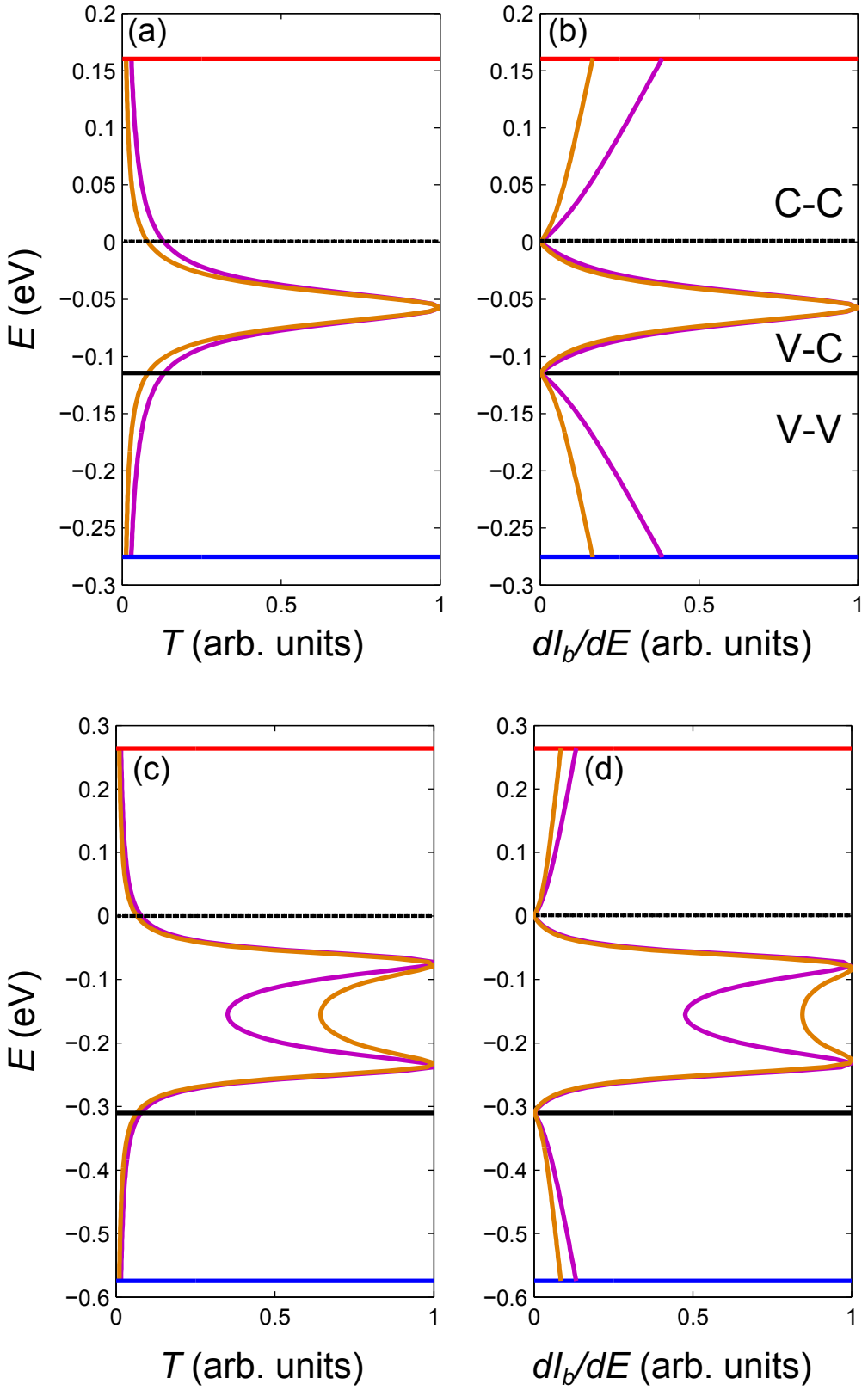

Figure 3.7: $T(E)$ (a,c) and $\partial I_b/\partial E$ (b,d) for a high V_b point on the $I_b(V_b)$ curve; (a,b): the aligned device, (c,d): $\theta = 0.9°$ device. The red (blue) lines represent $\mu_B(\mu_T)$ and the solid black lines represent the positions of the Dirac point in the top cone, with respect to the Dirac point of the bottom cone (dashed black lines), which is at $E = 0$ eV. The purple curves show the calculated $T(E)$ and $\partial I_b/\partial E$ variations with chirality included, and the orange curves show the calculations with no chirality effects included.

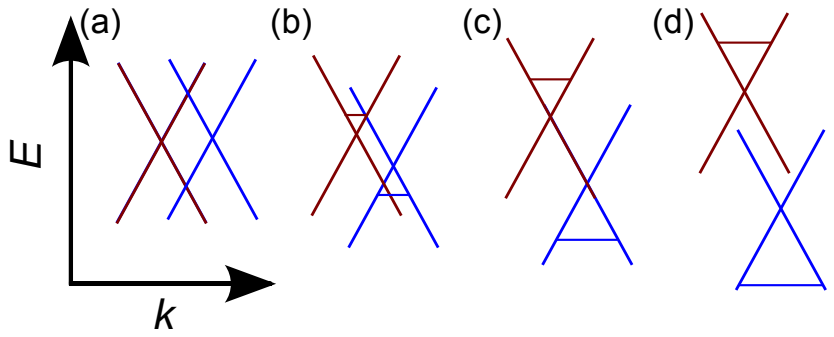

Figure 3.8: Band diagrams ($E-k$) of the bottom (red) and top (blue) Dirac cones for (a) $V_b = 0$ and (b-d) increasing $V_b > 0$, for a misaligned ($\theta = 0°$). The application of a bias voltage shifts the cones energetically with respect to each other. The misalignment of the graphene layers shifts the cones with respect to each other in k-space, which can be seen in further detail in Fig. 3.9.

with the geometric intersection coordinates:

$$x(E) = \frac{(\Delta\mathbf{K})^2 - k_T^2 + k_B^2}{2\Delta\mathbf{K}}, \tag{3.5}$$

$$y(E) = \sqrt{\frac{4(\Delta\mathbf{K})^2 k_B^2 ((\Delta\mathbf{K})^2 - k_T^2 + k_B^2)^2}{4(\Delta\mathbf{K})^2}}. \tag{3.6}$$

The form of these intersection points joined together will then either be hyperbolic, elliptical or linear depending on s_B and s_T. For a further detailed explanation of the form of these curves, see Ref. [20].

We see the effect of misalignment on the position of Dirac cones in k-space for different V_b in Fig. 3.8. In the aligned case, at $V_b = 0$, all states are aligned and able to tunnel, as in Fig. 3.4(a). However, in the corresponding diagram 3.8(a) for $\theta = 0.9°$, the cones are no longer completely overlapping and thus tunnelling between some states is forbidden. This alters the shape and magnitude of the $I_b(V_b)$ characteristics as seen in Fig. 3.11 (red curve) compared to the aligned sample (blue dashed curve). We see the current peak is decreased in magnitude and occurs at a higher V_b when the graphene layers are misaligned. For very low $V_b > 0$, no current flows. The affect of misalignment will be further discussed in detail in Section 3.5.

3.3 Momentum Conservation

Curves of intersection between the Dirac cones of the top and bottom graphene electrodes, where electrons can tunnel with conservation of mo-

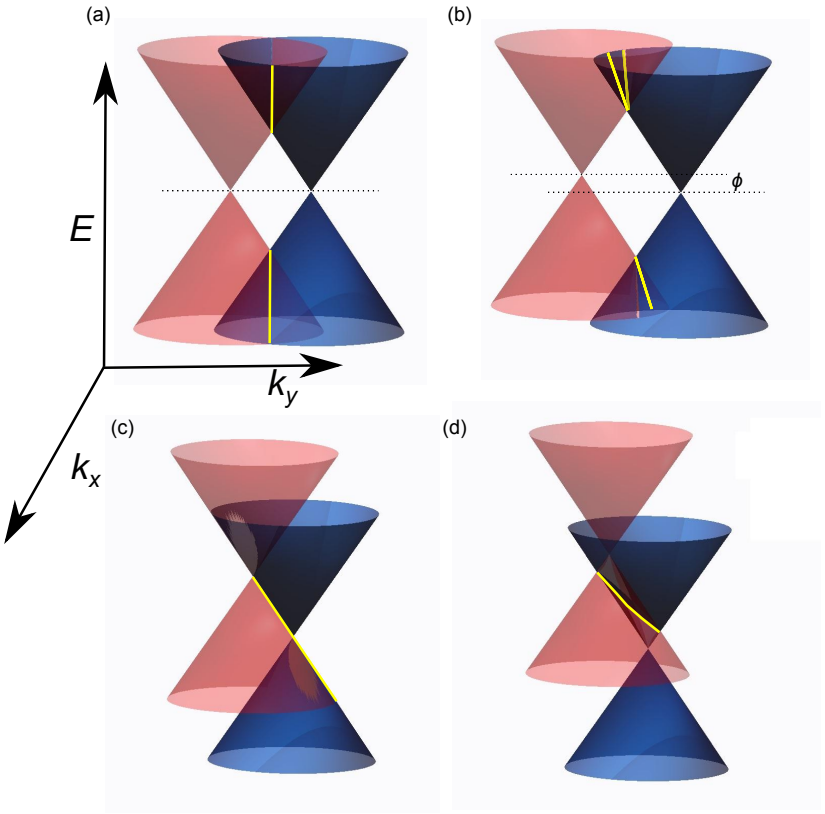

Figure 3.9: Dirac cones of the bottom (red) and top (blue) graphene layers, misaligned by a small angle θ. If $\theta = 0°$, the cones lie directly on top of each other, i.e. at the same point in the (k_x, k_y) plane. The yellow curves represent intersecting states which can tunnel with conservation of energy and momentum. (a) $V_b = 0$ V, (b) $0 < V_b < V_{peak}$, (c) $V_b = V_{peak}$, and (d) $V_b > V_{peak}$, where V_{peak} is the bias voltage at which the resonant peak in the $I_b(V_b)$ characteristics occurs. The line of intersection changes from a line (a), to a hyperbola (b), to a line (c), to an ellipse (d) as the bias voltage is increased.

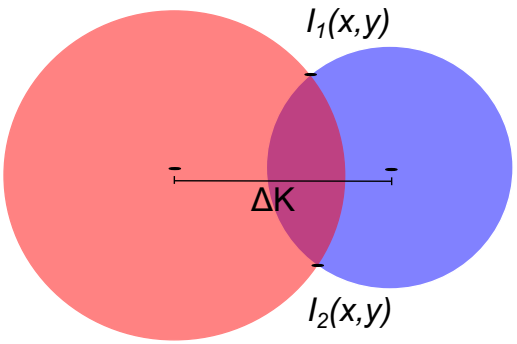

Figure 3.10: Conservation of momentum and energy leads to two intersection points, $I_1(x, y)$ and $I_2(x, y)$ at any given energy.

mentum and energy, are shown (yellow), for four V_b values, in Fig. 3.9 when $\theta = 0.9°$. The misalignment of the graphene layers shifts the Dirac cones with respect to each other in k-space. Fig. 3.9(a) shows the cones at zero applied bias voltage, and we see the points of conservation of momentum are represented by a line (yellow). With some applied voltage but before the current peak, this intersection has the form of a hyperbolic curve that extends between the Dirac points and the chemical potentials in the two layers. The length of this curve increases as V_b increases and therefore the current also increases, as seen in Fig. 3.9(b). At the current peak, the two Dirac cones just touch and so their intersection is a straight line along the surface of the cone, as shown in Fig. 3.9(c). In this case, $|\phi| = \hbar v_F |\mathbf{\Delta K}|$ and so electrons can tunnel between many states with conservation of energy and momentum and a large number of states are occupied in one layer and empty in the other layer due to the high magnitude chemical potentials, thus facilitating a large resonant tunnel current. For V_b values beyond the current peak, the in-plane momentum is only conserved for $k-$states along an elliptical locus of intersection between the Dirac cones for the two layers, as seen in Fig. 3.9(d). The number of available states that can tunnel is thus diminished and so the current falls. Note that in our model, tunnelling transitions induced by a Gaussian scattering potential with a characteristic length scale of 15 nm [52], as described in Section 3.1.1 are included, i.e. states near the yellow curves of intersection in Fig. 3.9.

3.4 Model Validation

Preliminary devices, a schematic of which is shown in Fig. 3.13, have been produced and measured by the graphene group at the University of Manchester [20, 52]. These results can be used to test our model, by using the parameters of the devices produced; an active tunnel area of $A = 120$ μm^2, graphene lattices misaligned at $\theta = 0.9°$ and four layers of hBN forming a barrier of width $d = 1.4$ nm. In Eq. (3.1), values for the potential length scale, V_0, and for the scattering length scale, q_c, must be chosen. Here, we take parameters consistent with those observed in models of Coulomb impurity disorder in single layer graphene, $V_0 = 10$ meV and q_c^{-1} of the order of 10 nm [77, 80]. From Fig. 3.2, it was found that $q_c^{-1} = 15$ nm gave the best agreement to experimental results and we will therefore fix q_c^{-1} to this value for the rest of our investigation.

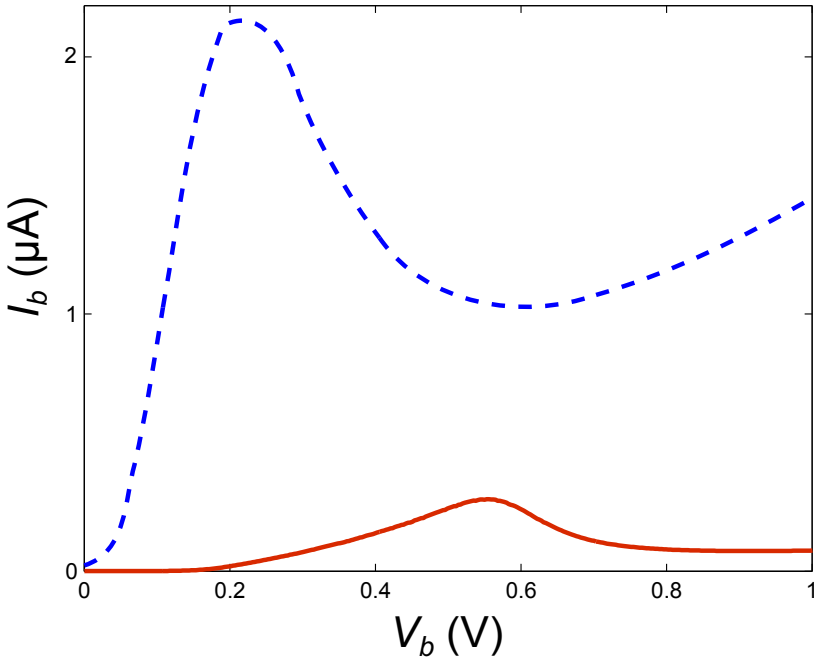

Figure 3.11: $I_b(V_b)$ characteristics calculated for a device with $N_L = 4$ and $\theta = 0°$ (blue dashed curve) and $\theta = 0.9°$ (red curve).

The colour maps shown in Fig. 3.14 give a deeper insight into the effect of q_c on the $I_b(V_b)$ characteristics when $V_g = 0$, and help us select the fixed value for q_c. For very low q_c^{-1}, there is no peak in the current, as seen in Fig. 3.14(a). As q_c^{-1} is increased, a current peak occurs with a decreasing maximum current. For a small q_c^{-1}, the $V_0/(q_c^2 + q^2)$ scattering term falls off more slowly with increasing q, and thus transitions with a large q make a more significant contribution to the current compared to when q_c^{-1} is large. For very low q_c^{-1}, changes in the density of states dominate rather than those in the scattering term. This increases I_b and requires a higher V_b to suppress the current beyond the peak. The conductance, $\partial I_b(q_c^{-1}, V_b)/\partial V_b$ seen in Fig. 3.14 shows NDC is induced when $q_c^{-1} > 3$ nm, and its value increases as q_c^{-1} increases and the width of the scattering term decreases. The highest magnitude NDC and PVR would thus be achieved with the largest physically-attainable q_c^{-1}, since that would lead to a well-defined tunnelling peak when $\mathbf{q} = 0$. There is, however, a limit on the sharpness of the resonant peak due to size effects of the electrodes at such length scales, and therefore, the magnitude of the NDC has an upper limit also. In our investigation, we therefore set $q_c = 15$ nm^{-1} as the longest q_c^{-1} currently achievable.

The lineshapes of the $I_b(V_b)$ characteristics were found to agree, and the

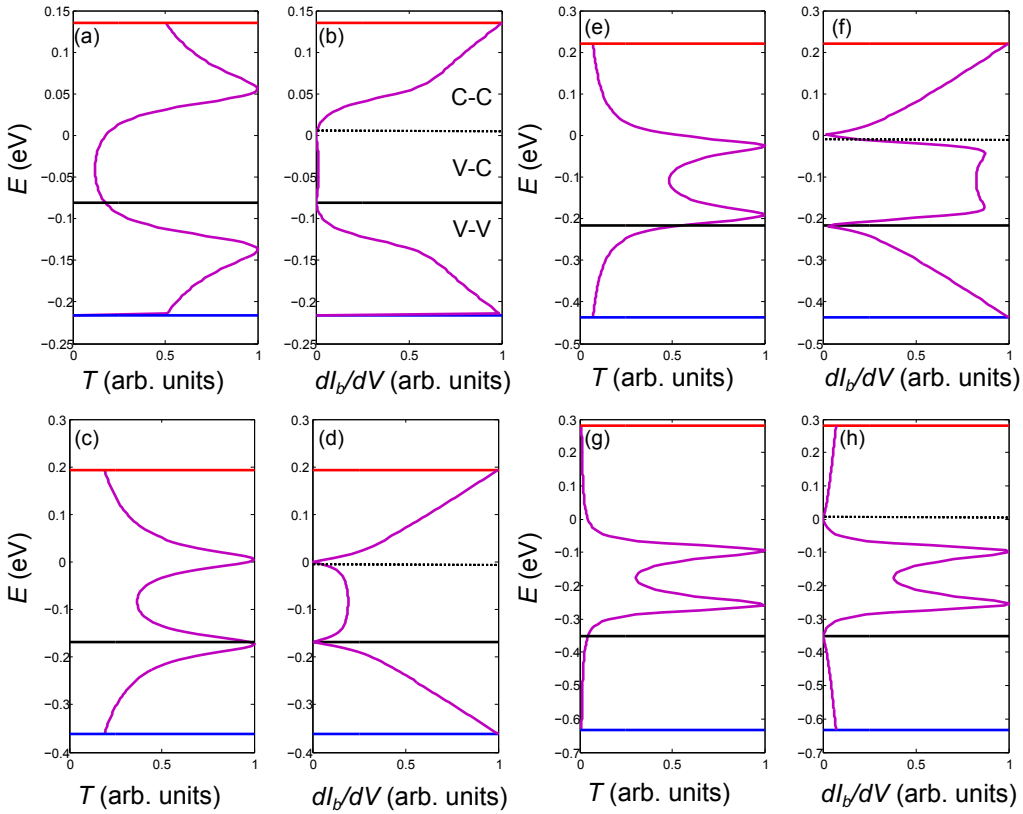

Figure 3.12: $T(E)$ (a,c,e,g) and dI_b/dV_b (b,d,f,h) for three points on the $I_b(V_b)$ curve; (a,b): V_b= 0.35 V, i.e. in the first PDC region, (c,d): V_b= 0.56 V, i.e. the peak, (e,f):V_b= 0.66 V, i.e. the NDC region, and (g,h) V_b= 0.91 V, i.e. the valley. We see again the trade-off between momentum conservation and the linear density of states. The red (blue) curves represent $\mu_B(\mu_T)$ and the solid black lines represent the positions of the Dirac point in the top cone, with respect to the Dirac point of the bottom cone (dashed black line), which is at $E = 0$ eV. Three different regimes of tunnelling are shown in (b), explained in the text, ($\theta = 0°$).

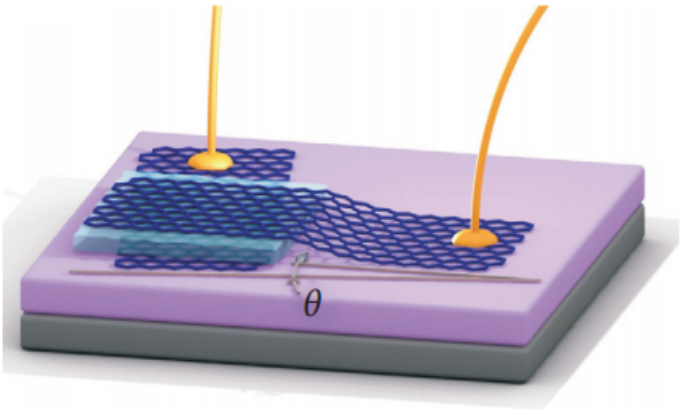

Figure 3.13: A schematic diagram of the device in [20] with an exaggerated angle, θ, between the two graphene layers, separated by a light blue hBN tunnel barrier. Both graphene layers are independently contacted by Cr/Au metallization (yellow) some distance away from the tunnel area. This initial design leads to a higher parasitic capacitance and resistance than the device in the optimized device of Fig. 1.12.

calculated current magnitudes were found to be within an order of magnitude of the measured I_b when using the equations:

$$I_b = \frac{8\pi e}{\hbar} \sum_{\mathbf{k}_B, \mathbf{k}_T} |M|^2 [f_B(E_B) - f_T(E_T)] \delta(E_B - E_T - \phi_b), \tag{3.7}$$

$$M = \Xi g(\varphi_B, \varphi_T, \theta) V_S(\mathbf{q} - \mathbf{\Delta K}), \tag{3.8}$$

where $\Xi = \xi e^{-\kappa d}$, ξ is a normalisation constant determined by comparison with recent measurements. In our analysis, ξ is approximated to be $1/D_g$, where $D_g = 0.335$ nm is the interlayer separation in graphite. As the transmission has an exponential dependence on κ and d, the current magnitude is very sensitive to small variations in these values. Although the model produces results within one order of magnitude of the measured current, the precise nature of the decay in the barrier is uncertain. Therefore, to fully match experimental results, an additional scaling parameter is applied to Eq. (3.7), and the resulting calculated peak-to-valley ratio agrees well with that of the device.

Fig. 3.15 shows the current and conductance calculated vs the bias and gate voltages. As expected, $I(V_g, V_b)$=-$I(-V_g, -V_b)$, and increasing V_g

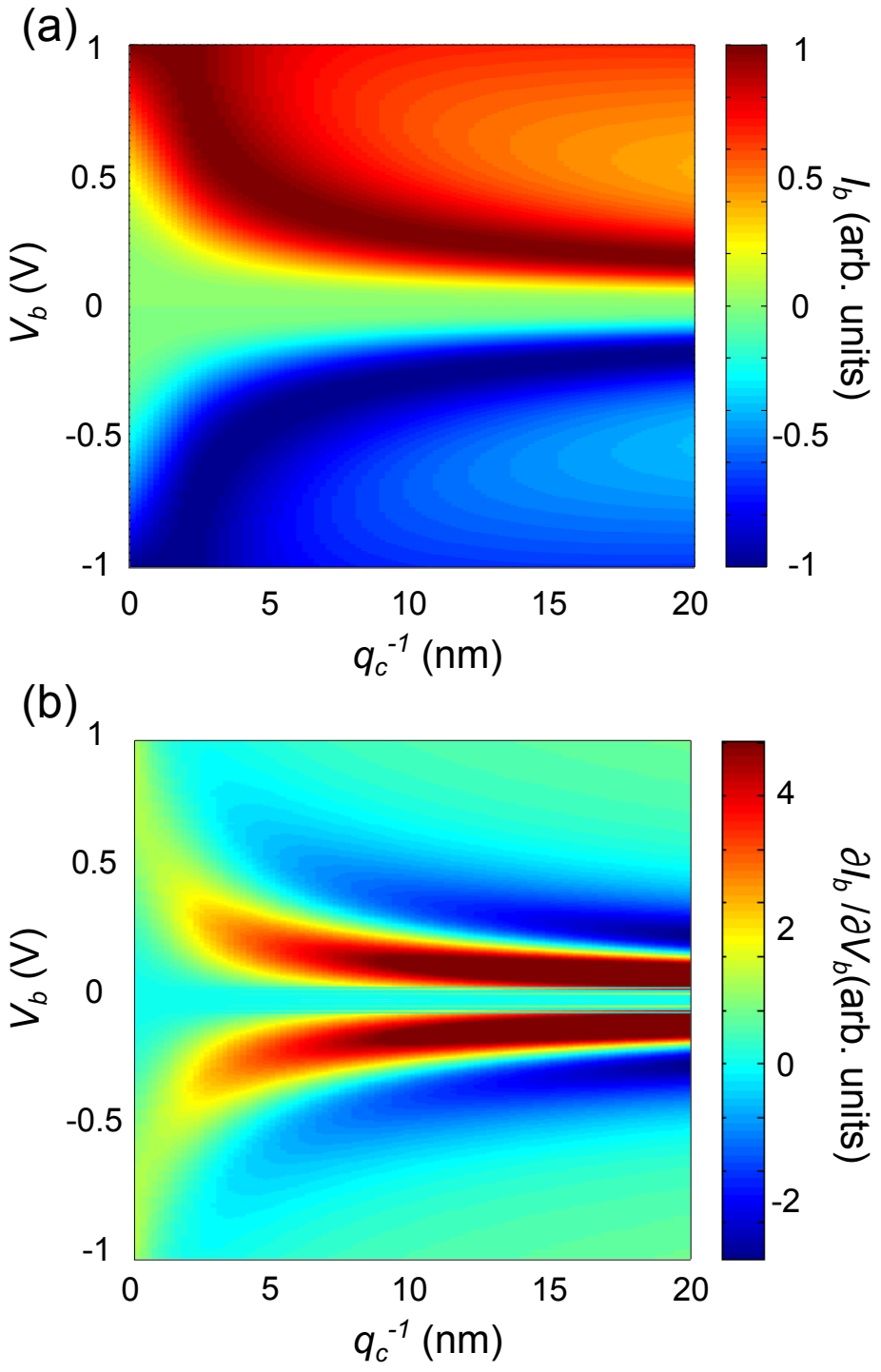

Figure 3.14: Colour maps of (a) $I_b(q_c^{-1}, V_b)$ and (b) $\partial I_b(q_c^{-1}, V_b)/\partial V_b$, calculated when $V_g = 0$ for a device with $\theta = 0°$. Increasing q_c^{-1} compresses features in the $I_b(V_b)$ characteristics along the V_b axis and leads to a significant NDC region, as seen in (b). Below q_c^{-1} <3 nm, there is only weak NDC, as the changes in the density of states, rather than $V_S(\mathbf{q})$, dominate.

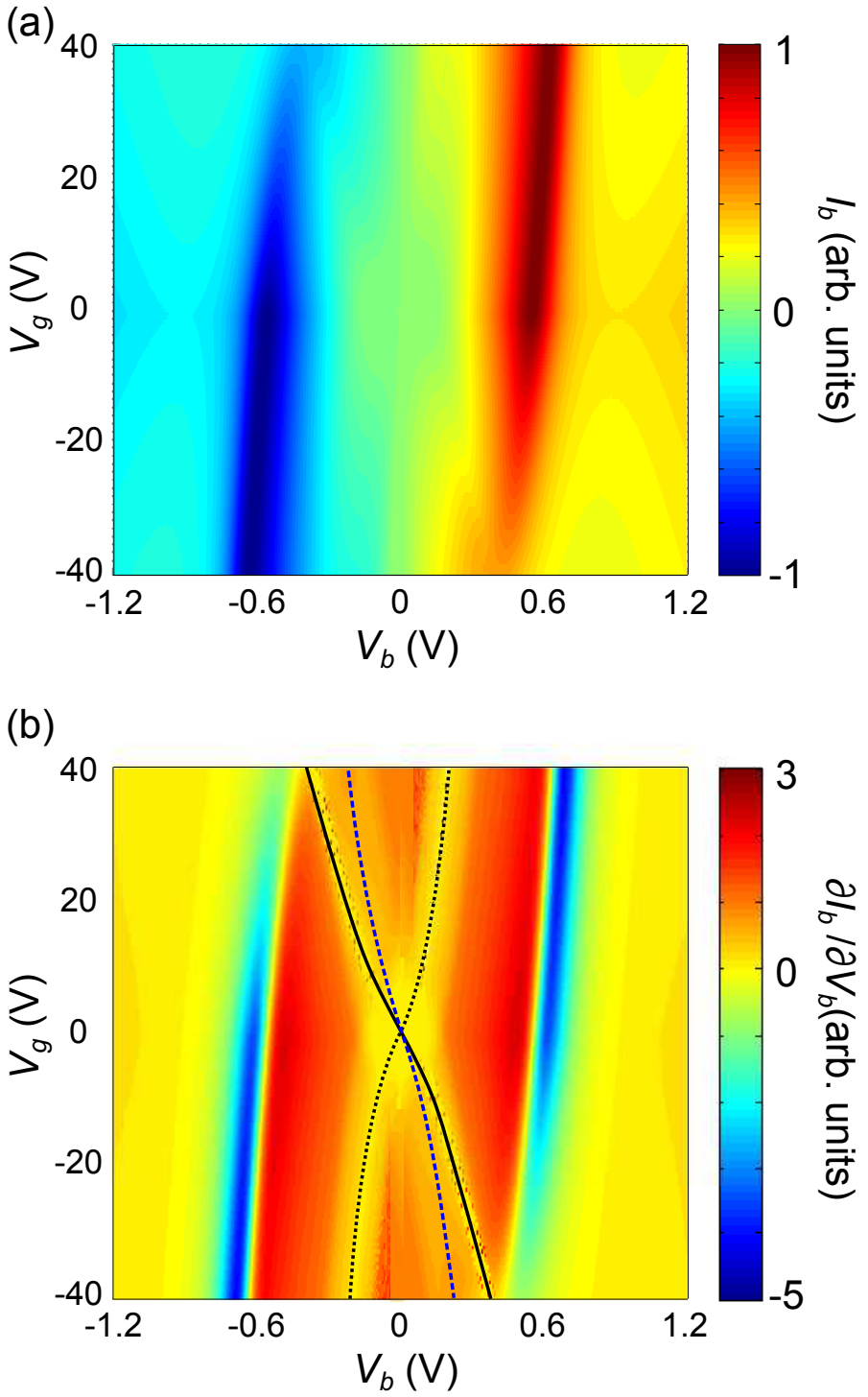

Figure 3.15: Colour maps of (a) $I_b(V_g, V_b)$ and (b) $\partial I_b(V_g, V_b)/\partial V_b$, calculated when $V_g = 0$, $q_c^{-1} = 15$ nm for a device with $\theta = 0°$. The dashed curves show loci where $\mu_T = E_{DB} = E_{DT}$ (black dashed curve), $\mu_B = E_{DT}$ (blue dashed curve) and $\mu_B = E_{DB}$ (solid black curve).

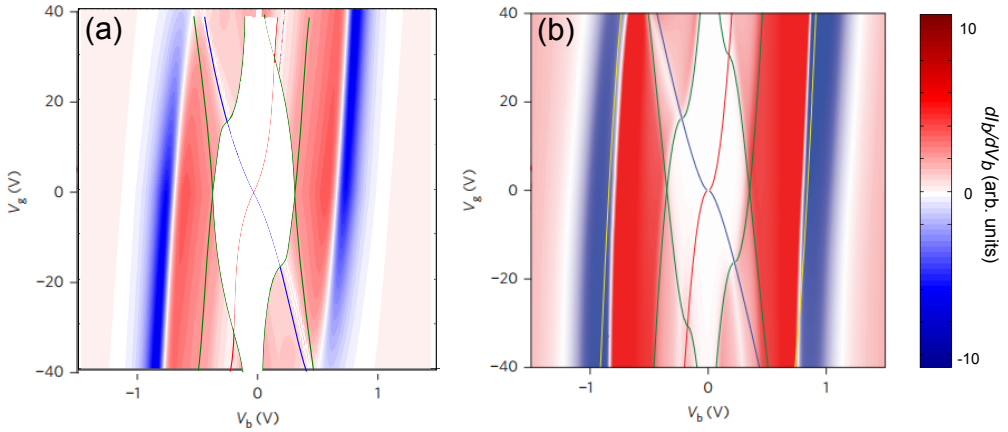

Figure 3.16: (a) Theoretical and (b) experimental [20] measurements of $\partial I_b(V_g, V_b)/\partial V_b$ for a $\theta = 0.9°$ device. The loci (red and blue) correspond to the chemical potential in one layer passing through the Dirac point of the other layer.

increases (decreases) the current peak for positive (negative) V_b. The current peak also shifts to higher $|V_b|$ for increasing $|V_g|$ as a higher $|V_b|$ is required for the energetic alignment of the Dirac cones. The results calculated for a $\theta = 0.9°$ device in Fig. 3.16(a) agree well with the features seen in the experimental measurements shown in Fig. 3.16(b). We note that due to the misalignment, current only switches on once the chemical potential magnitude exceeds the intersection point, resulting in a large central region of $I = 0$ (white).

We can now modify the device parameters to simulate the change in $I_b(V_b)$ characteristics in future devices, such as alterations to the barrier and chemically doping the graphene layers. We note that several features of the measured $I_b(V_b)$ characteristics are not reproduced by the simulations. For example, at $V_b = 0$, the measured current is finite for all values of V_g, rather than the simulated result of zero. This is probably due to the residual doping of the graphene layers, the existence of electron-hole puddles and leakage current. This region of the $I_b(V_b)$ curve, however, is unimportant for the operation of the device, which will be biased around the NDC region. In the operational V_b range, the effect of electron-hole puddles will be negligible, due to the increased induced carrier densities.

Another example of deviation between the model and experimental results is seen when looking at the $I_b(V_b)$ characteristics for negative V_b. Here, the model predicts symmetric behaviour for the $V_g = 0$ V curve and asymmetric

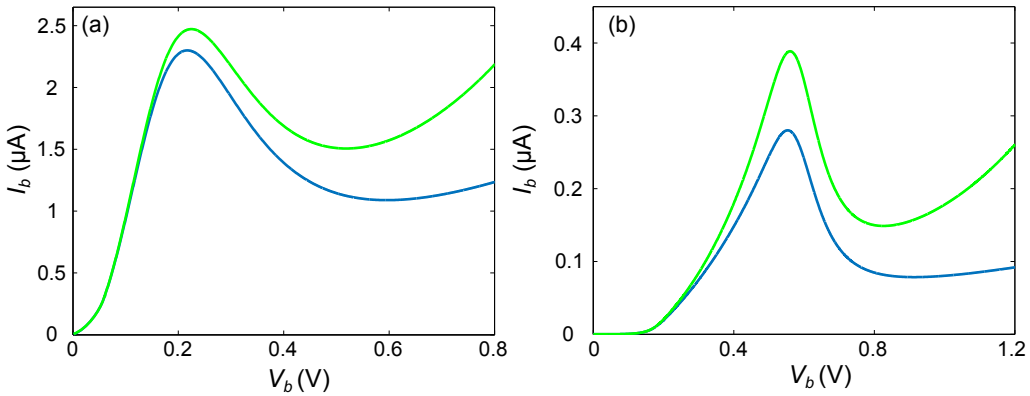

Figure 3.17: $I_b(V_b)$ characteristics calculated for a device with $N_L = 4$ and a barrier height of Δ (blue) and a tilted barrier of $\Delta - \phi/2$ (green) for (a) $\theta = 0°$ and (b) $\theta = 0.9°$.

behaviour for $V_g \neq 0$ V (curves shown in Fig. 3.24), but the measured results reveal asymmetry for all $V_g \neq -20$ V. A lower PVR is measured than expected from the simulations, this effect may arise due to small leakage currents between the graphene electrodes, potentially involving inelastic scattering also, or a more complex $V_S(\mathbf{q})$. Microstructural analysis [62, 78] of the graphene and boron nitride layers indicate that they have a high level of structural perfection, so grain size effects can be neglected in our devices.

3.4.1 Tilted Tunnel Barrier

It is important to consider the effect of high fields across the tunnel barrier. For large V_b, the field will be large, leading to a spatial non-uniform modification of the electrostatic energy drop of the barrier in z. This effectively reduces the height of the barrier for the tunnelling electrons.

At higher V_b, the potential barrier due to the tunnelling material will become more sloped due to the higher carrier densities in each graphene layer, which induce the distance-dependent term $\phi = eF_b d$ across the barrier. Simulations were run for isotropic barriers of fixed height Δ, and with a height of $\Delta - \phi/2$. It is found that an isotropic barrier is a good approximation for the tunnel barrier as the lineshape and magnitude of the $I_b(V_b)$ characteristics are similar, see Fig. 3.17, especially at low V_b and within the operational V_b range of the device [51]. Thus, for simplicity, we will use a fixed barrier height.

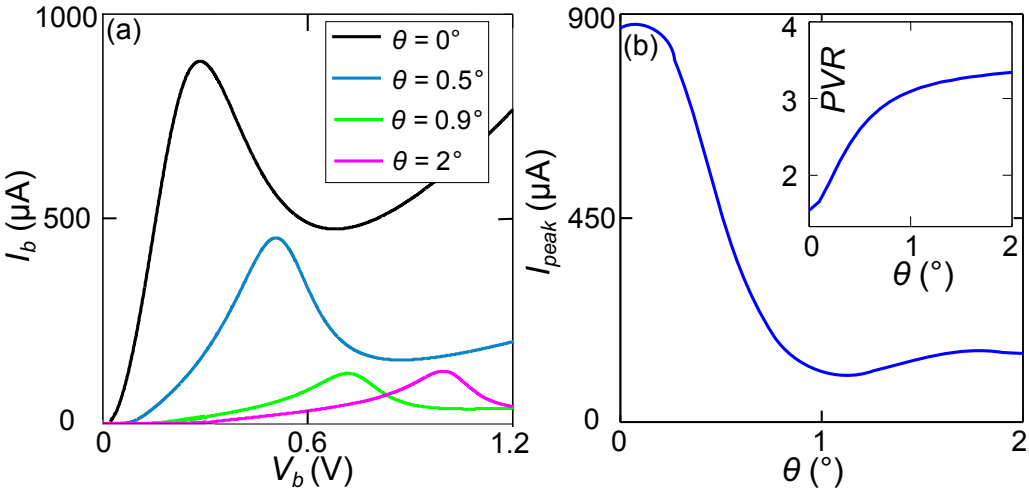

Figure 3.18: (a) $I_b(V_b)$ characteristics for undoped, $N_L = 2$ devices with misalignment angle $\theta = 0 - 2°$. (b) Peak current vs θ, and peak-to-valley ratio (inset).

3.4.2 Active Tunnelling Area

The first GRTD sample devices produced have had a wide span of active tunnelling areas, from 0.3 μm^2 [52] to 120 μm^2 [20]. The current per unit area for devices with $\theta = 0.9°$ and $N_L = 4$ has been consistently around 0.28 μAμm^{-2}, and thus for simplicity, we will consider devices with a fixed active area of 1 μm^2. Increasing the area would increase the current and power output, however, it would also increase the geometric capacitance, $C_g = \epsilon_r \epsilon_0 A/d$. This would limit the frequency of operation achievable, as discussed in Section. 4.3. The dependence of frequency on area will be non-linear, due to the change in R_N, the resistance in the NDC region, along with the change in C.

3.5 Misalignment of the Graphene Layers

The $I(V_b)$ characteristics show the interplay between the shift to higher voltages (and thus larger n) of the resonant conditions and the decrease in overlap of the spatial parts of the wavefunction, firstly, showing an increase in the peak-to-valley ratio (PVR) and current peak magnitude as the misalignment is increased, followed by a decrease in current until θ reaches 1.2°, when the current begins to increase again despite the steady PVR. The current peak and NDC region are shifted to higher V_b as the layers become more misaligned, due to the shift in energetic alignment of

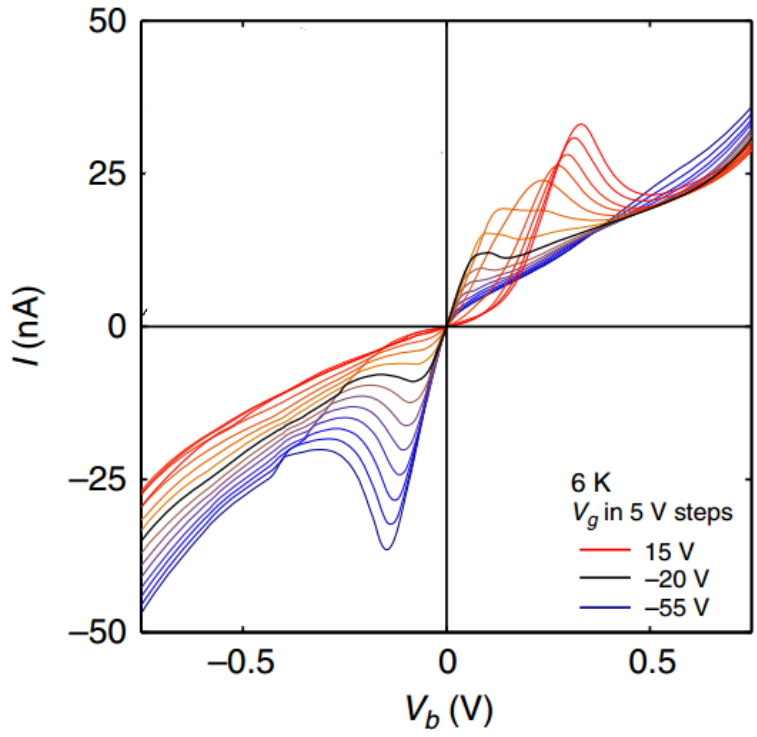

Figure 3.19: Measured $I_b(V_b)$ characteristics taken from Britnell et. al. [52] for undoped, $N_L = 4$ devices with a high misalignment angle ($\theta >> 2°$) and varying V_g.

tunnelling states, the effects of which will be further discussed in detail.

As misalignment is increased, the peak-to-valley ratio (PVR) generally increases despite the suppression of the current peak as a result of the lack of available states for tunnelling. The interplay between the overlap and the energetic alignment of the tunnelling states leads to a decrease in the valley current. The NDC region is also shifted to higher V_b for higher θ.

To quantify the possible benefits of lattice alignment, Fig. 3.18 shows static $I_b(V_b)$ characteristics calculated for several misalignment angles; $\theta = 0°$ (black), $\theta = 0.5°$ (blue), $\theta = 0.9°$ (green) and $\theta = 2°$ (magenta). We see that as θ increases, the position of the current peak shifts to higher V_b. The peak current amplitude, I_{peak}, decreases as θ increases due to increasing misorientation of the spatial parts of the wavefunction, see Fig. 3.18(b), so that I_{peak} could be $\sim 10\times$ larger for an aligned device. However, for undoped samples, the PVR increases with increasing θ, see inset in Fig. 3.18(b), converging to a value of 3.4 as θ approaches 2°. At higher θ, more states are available to tunnel resonantly at the current peak [54]. For the doped samples ($n_B^D = 10^{13}$ cm^{-2}), the valley current is close to 0 for all

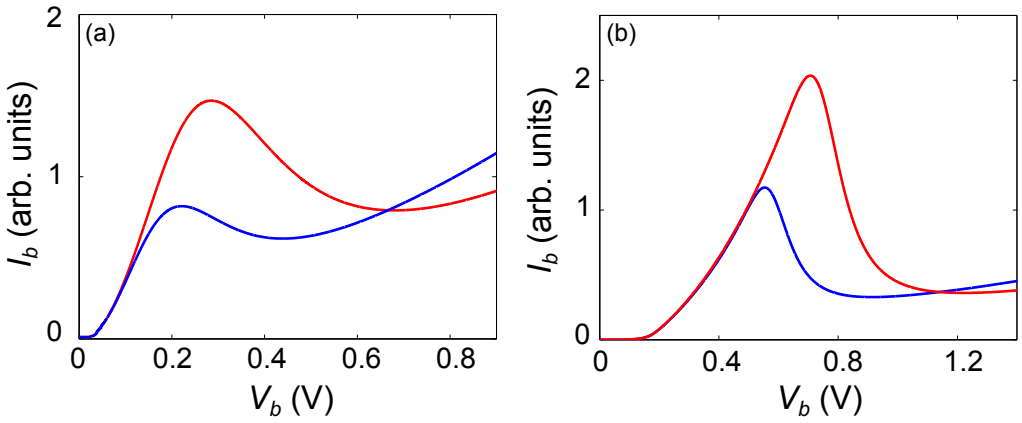

Figure 3.20: $I_b(V_b)$ characteristics calculated without the $\exp(-2\kappa d)$ term, to demonstrate the effect of the decreasing the field, F_b, via decreasing the barrier width, d. Devices with $N_L = 4$ (blue curve) and $N_L = 2$ (red curve), for (a) $\theta = 0°$ and (b) $\theta = 0.9°$.

θ, thus the PVR is consistently large. Increasing the misalignment angle further causes the Dirac cones to become so misaligned ($\theta >> 2^0$) that little tunnelling occurs.

An interesting point to note can be seen in the results shown by Britnell et. al. [52], as seen in Fig. 3.19. Here, in the initial GRTD devices, the alignment of the graphene layers was not considered. Thus the graphene layers are highly misaligned ($\theta >> 2°$), yet when a gate voltage, V_g, is applied, the $I_b(V_b)$ characteristics have features very similar to those of an aligned device, rather than the slightly misaligned ($\theta < 2°$). For example, at low bias voltage, a slightly misaligned sample would have a low conductance, however, we see here that the device has a high conductance, as if it were aligned.

3.6 Barrier Thickness

The tunnel barriers in the first devices, studied in [52], were composed of 4 atomic layers of hexagonal boron nitride in order to operate in a comfortable range of current densities and bias voltages. Here, we consider the effect of changing the number of layers, N_L, which make up the barrier, which is of thickness d. There are two main effects on the equilibrium $I_b(V_b)$ characteristics when changing d; the change in the matrix element due to wavefunction overlap and the shift of the Dirac points relative to each other by $\phi = eF_bd$. The dominant effect comes from the matrix element due to the

term $\exp(-2\kappa d)$. This leads to a $\sim$ 320-fold increase in the current when halving the barrier width from $N_L = 4$ to $N_L = 2$, and $\sim$ 18-fold increase when changing from 4 layers to 3. The second effect is due to the reduction of ϕ, which is demonstrated in Fig. 3.20. Here the $I_b(V_b)$ characteristics are calculated without the change to the matrix element. We see a change in the resonant conditions and the number of states available for tunnelling, i.e. the resonant peak is shifted in the $N_L = 2$ device (red curve) to a higher bias voltage (0.71 V compared to 0.55 V) than the $N_L = 4$ device (blue curve). The result is an increase in current as d is decreased; the current at the peak is also almost twice as high in the $N_L = 2$ device. An interesting point is that for low V_b, the curves are equivalent whilst the Dirac cones fill up, thus the total change in $I_b(V_b)$ characteristics, as seen in Fig. 3.21, is due to the change in the matrix element only, in this region. Decreasing d also increases the geometric capacitance of the device, an effect which will be discussed in Section 4.6. The results from the simulations are in good agreement with experimental results from Britnell et. al. [62]. Although it is possible to construct a device with only one layer of hBN as the barrier, the resonant peak would shift to even higher voltages, which when applied at such a high magnitude, may damage the device. Also, the wavefunctions of the graphene layers would then overlap in the z direction and affect the behaviour of the device.

3.7 Chemical Doping of the Graphene Layers

In order to fully exploit graphene's potential and tune the current-voltage curves of the device, the additional gate electrode can be used to change the carrier density in the electrodes, which allows the manipulation of the resonant peak and the associated NDC region. Equivalently, the $I_b(V_b)$ characteristics can also be modified by doping the graphene chemically [81, 82]. The relation between gate voltage and doping levels can be seen by combining Eqs. (2.25,2.26,2.29) to give:

$$eV_b = eV_g + \frac{e^2(n_B - n_B^D)D}{\epsilon} + \frac{e^2(n_T - n_T^D)D}{\epsilon} - \mu_T(n_T) + \frac{e^2(n_B - n_B^D)d}{\epsilon}. \quad (3.9)$$

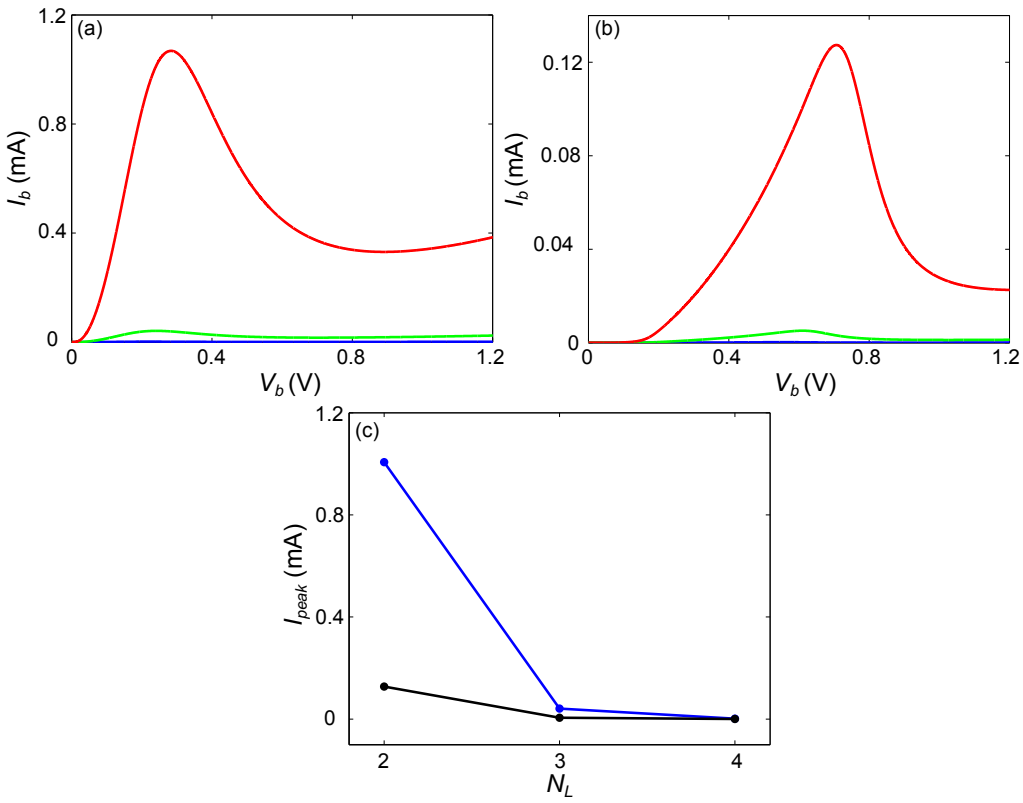

Figure 3.21: $I_b(V_b)$ characteristics calculated for a device with $N_L = 4$ (blue), $N_L = 3$ (green) and $N_L = 2$ (red) for (a) an aligned device and (b) a misaligned ($\theta = 0.9°$) device. (c) Comparison of current peak, I_{peak}, for aligned (blue) and misaligned (black) devices vs N_L.

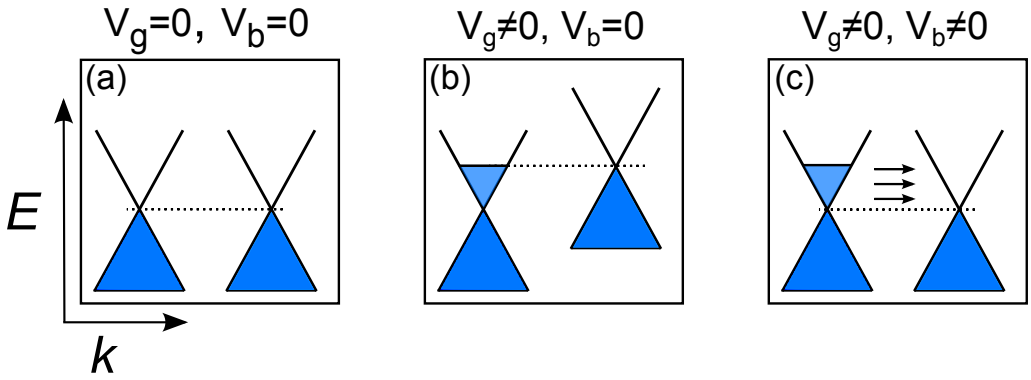

Figure 3.22: Dirac cones for the bottom (left) and top (right) graphene layers, shown with a visual displacement in k-space, for (a) zero applied bias and gate voltages, (b) zero applied bias voltage and nonzero doping or gate voltage, (c) nonzero applied bias voltage and doping or gate voltage. In (c), we see the filled cones have been brought back into the alignment shown in (a), but with a large number of states in the conduction band of the bottom cone available for resonant tunnelling.

At $V_b = 0$, when a gate voltage or n_B^D is applied, the chemical potential in the bottom cone increases, as seen in Fig. 3.22(b). The Dirac points of the cones can then be brought back into alignment by adjusting V_b. But then there are many filled states in the conduction band of the bottom cone which can all resonantly tunnel to many empty states in the conduction band of the top layer. Thus, we expect an increase in current and a change in the resonant V_b condition. Here, we investigate the effect of doping the bottom graphene electrode only. Doping is used rather than a gate voltage in order to avoid the extra capacitance a gate electrode would introduce. Also, although increasing V_g leads to desired properties such as a higher peak current and higher PVR, it must be limited to $|V_g| < 50$ V in order to not damage the device, for $D = 300$ nm. Consequently, doping is the preferred choice of shifting the resonant conditions here.

In Fig. 4.16(a), we show $I_b(V_b)$ curves calculated when $N_L = 2$ for an undoped (red curve) and an asymmetrically-doped device with $n_B^D = 10^{13}$ cm^{-2}, $n_T^D = 0$ (green curve). When $n_B^D > 0, n_T^D = 0$, the resonant peak occurs at higher V_b than when $n_B^D = 0$, and the current peak magnitude is higher, raising the peak-to-valley ratio (PVR) from 1.5 to 3.5. The magnitude of R_N is also increased, which is a good indication for high-frequency performance, as discussed further in Section. 4.3.

The shoulder of the green curve in Fig. 3.23 (arrowed) when $n_B^D = 10^{13}$ cm^{-2}, arises from the low density of states around the Dirac point. At this V_b, the doping levels are such that the chemical potential in the top graphene layer aligns with the Dirac point of the bottom layer. When this occurs, carriers close to the Fermi level in one electrode can only tunnel to a very low density of states in the other, such that the current is dominated by the DoS. Therefore, the current becomes insensitive to small changes in V_b, yielding a differential conductance close to zero. This gives rise to an additional quantum capacitance [52, 74], C_Q. The total capacitance is given by:

$$\frac{1}{C} = \frac{1}{C_G} + \frac{1}{C_Q}, \tag{3.10}$$

where $C_G = \epsilon_0 \epsilon_r A/d$ is the geometric capacitance.

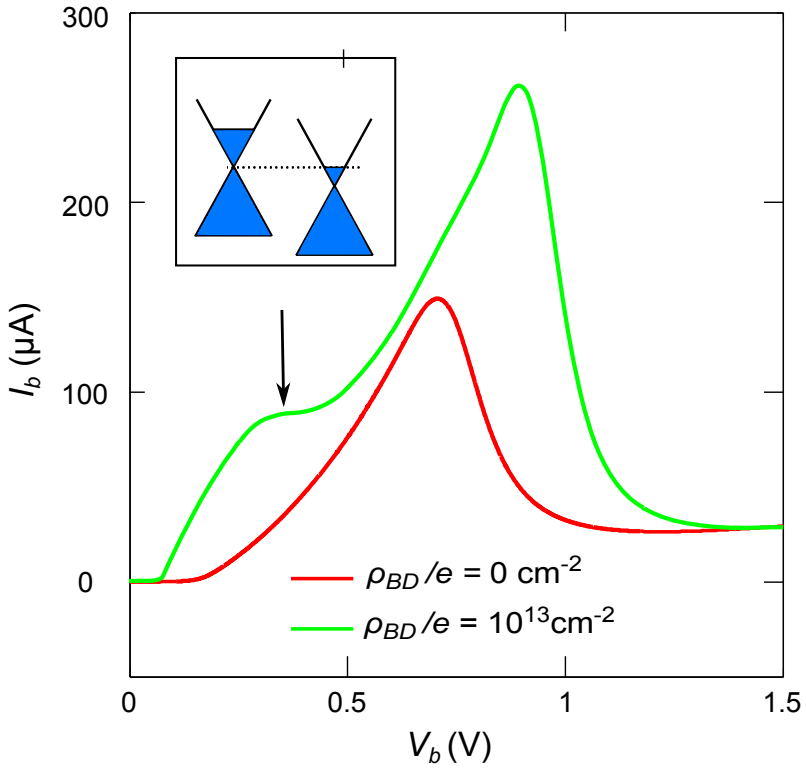

Figure 3.23: $I_b(V_b)$ characteristics calculated for $N_L = 2$, $\theta = 0.9°$ devices with $n_B^D = 0$ cm^{-2}, $n_T^D = 0$ (red curve) and $n_B^D = 10^{13}$ cm^{-2}, $n_T^D = 0$ (green curve). The shoulder (arrowed) indicates a new feature arising when the chemical potential of the top graphene layer passes through the Dirac point of the bottom graphene layer, leading to the quantum capacitance becoming the main contributor to the capacitance. The band diagrams are inset, with an additional visual displacement in **k**.

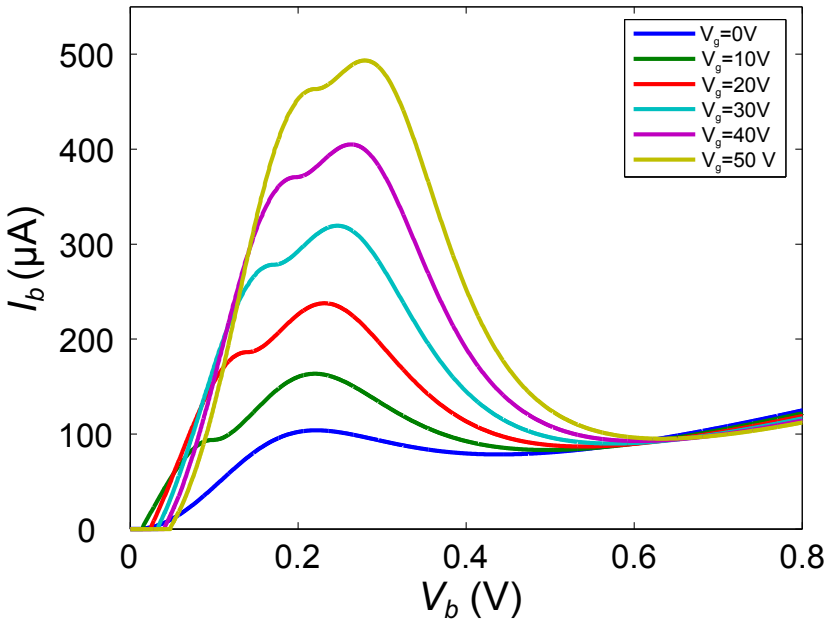

Figure 3.24: $I_b(V_b)$ characteristics calculated for an aligned device with $N_L = 4$ and $V_g = 0 - 50$ V (see legend inset). Increasing the gate voltage leads to a higher current, a shift in the resonant peak to higher bias voltages, and the illustration of the quantum capacitance effect. These changes can similarly be induced by chemically doping the graphene layers.

3.8 Barrier Composition

The material selected for the barrier region determines the barrier height, Δ, and, consequently, the barrier decay constant, $\kappa = \sqrt{2m^*\Delta}/\hbar$, where $m^* = 0.5m_e$ is effective mass of an electron in hBN, where m_e is the electronic mass. Hexagonal boron-nitride was chosen as the tunnel barrier material for the first devices due to its stability and similiar lattice size to graphene. We set κ to be a constant in this investigation, dependent on the barrier height. Although κ will change throughout the barrier, a method with a z-dependent κ was tested and the results were found to be almost identical, so, for simplicity, a constant value will be used. For hBN, $\Delta = 1.5$ eV [83, 84] and is included in the current calculation via the term $\exp(-2\kappa d)$.

The current density can be dramatically increased if a material with a lower tunnel barrier is selected, for example, WS_2, which has a band gap of 2.1 eV and thus a barrier height of 1.05 eV [55]. As we can see from Fig. 3.25, this results in an increase over 6× in the current, but does not affect the V_b value at which the peak occurs. MoS_2 is known to have an even smaller barrier height (0.65 eV), but care must be taken to ensure that tunnelling over the barrier is high enough for the current to be from

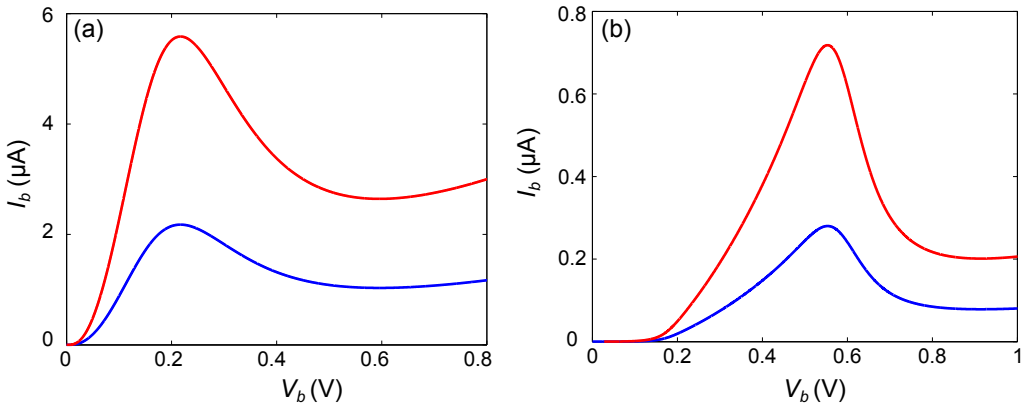

Figure 3.25: $I_b(V_b)$ characteristics calculated for undoped, $N_L = 4$ devices composed of hBN barrier layers (blue) and WS_2 layers (red) for devices with misalignment angles (a) $\theta = 0°$ and (b) $\theta = 0.9°$.

tunnelling rather than direct conduction. During simulations, $\mu_B < \Delta$ at all times for the current to be from tunnelling rather than conduction.

The on-off switching ratio of a transistor can be improved by having a lower barrier than hBN, so there is over-the-barrier thermal current at room temperature, but the effective barrier height can be increased by changing the gate voltage. An over-the-barrier current can be useful for high current, however, it kills off the NDC. hBN is a good barrier material because the energy gap is so wide that the over-the-barrier current is always small, even at room temperature. As the WS_2 has a much smaller band gap, it is possible the over-the-barrier current would destroy the NDC in this device, particularly at room temperature, in which all practical devices would need to work. Therefore, we will keep the focus on hBN only during this thesis.

Chapter 4

High-Frequency Current Oscillations

In this chapter, we consider the time-dependent charge dynamics of our graphene resonant tunnelling device. It is well known that devices exhibiting NDC can be used as high-frequency oscillators and amplifiers [76]. In some devices, such as III-V resonant tunnel diodes and semiconductor superlattices, oscillations can be induced in the device itself as it contains an in-built inductance. However, due to the lack of central quantum well and accumulation regions, which normally provide an in-built inductance, our device cannot be self-excited [85]. Therefore, we incorporate the device into an external resonant circuit as outlined below. The non-equilibrium charge dynamics are calculated and validated with experimental measurements [20, 52]. We consider the conditions necessary for oscillation and amplification. It has been shown in experiment that when the device is biased in the NDC region, the negative resistance, R_N, can effectively cancel out the oscillation decay associated with resistance and losses in the circuit, and thus support stable continuous oscillations at the resonant frequency of the LC circuit, as discussed in Section 1.7. The experiments have so far demonstrated self-sustained radio frequency oscillations, i.e. $\sim 1-2$MHz, for the present device and circuit parameters [20]. Here, we investigate the effect on frequency and power output due to changes in the $I_b(V_b)$ characteristics.

4.1 THz Technologies

Solid-state terahertz (THz) oscillators and amplifiers are essential components for high-frequency circuits. Semiconductor-based THz oscillators such as semiconductor lasers, quantum cascade lasers [86] and RTDs [87] have been studied extensively. Operation frequencies, output powers and operation temperature are all improving, with recent examples such as Suzuki *et al.* achieving output powers of 10 μW and oscillations at 1.04 THz [18] in GaInAs/AlAs DBRTDs. RTD-based oscillators offer the best potential for performance at room temperature [88].

4.2 Resonant Circuit Model

In our model, the device is placed in series with an external inductor, L. The parallel graphene layers of the device store and release charge, thus providing an in-built capacitance. Therefore, the device can be modelled by an effective circuit consisting of a capacitor, C, in parallel with a negative resistor, R_N, representing the resistance arising from the tunnel current. We also include the dissipative resistance, R, present within the device and circuit, e.g. arising from the gold contacts, and the leads and graphene sheets themselves. This forms the resonant RLC circuit shown in Fig. 4.1.

The charge continuity equation results in the following expressions for the carrier density on the two layers, $n_{B,T}$:

$$\begin{aligned} e\frac{dn_B}{dt} &= -\left(\frac{I - I_b}{A}\right), \\ e\frac{dn_T}{dt} &= \left(\frac{I - I_b}{A}\right), \end{aligned} \tag{4.1}$$

where $I(t)$ and $I_b(t)$ is the current in the contacts and through the barrier, respectively. As shown previously in Section 2.2, the electric field within the barrier (F_b) and due to the gate voltage (F_g), and the carrier densities in the graphene electrodes are related by Poisson's equations,

$$\begin{aligned} \epsilon(F_b - F_g) &= (n_B - n_B^D)e, \\ \epsilon(0 - F_b) &= (n_T - n_T^D)e, \end{aligned} \tag{4.2}$$

where $\epsilon = \epsilon_0\epsilon_r$ and $\epsilon_r = 3.9$ for hBN (ϵ_0) are the relative (absolute) permit-

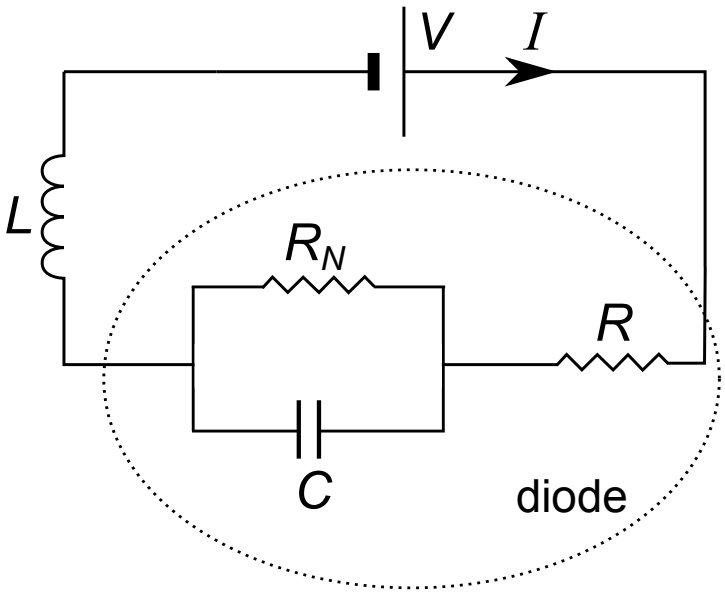

Figure 4.1: Effective circuit used for a small signal analysis of the behaviour of the graphene - hBN - graphene diode. The diode itself has an inbuilt capacitance, C, lossy resistance, R, and negative resistance, R_N. This is placed in series with an inductor, L.

tivies [89]. The time-evolution of the current in the inductor and the voltage across the capacitor are given by the following circuit equations:

$$\begin{aligned} \frac{dI(t)}{dt} &= \frac{V_L(t)}{L}, \\ \frac{dV_C(t)}{dt} &= \frac{I_C(t)}{C}, \end{aligned} \tag{4.3}$$

and the voltage drops in the circuit satisfy:

$$V = V_L + V_R + V_b. \tag{4.4}$$

Initially, $I_b(t)$ was calculated via the Bardeen transfer Hamiltonian method for each time step, which was rather slow due to the number of Runge-Kutta steps required. It was found that the values of $I_b(t)$ always remained within those spanned by the $I_b(V_b)$ curve and could therefore be looked up for each V_b, allowing a significantly faster calculation time, and thus allowing smaller time steps to be used. Fig. 4.2 shows the $I_b(V_b)$ points plotted in time (crosses) on the static $I_b(V_b)$ curve.

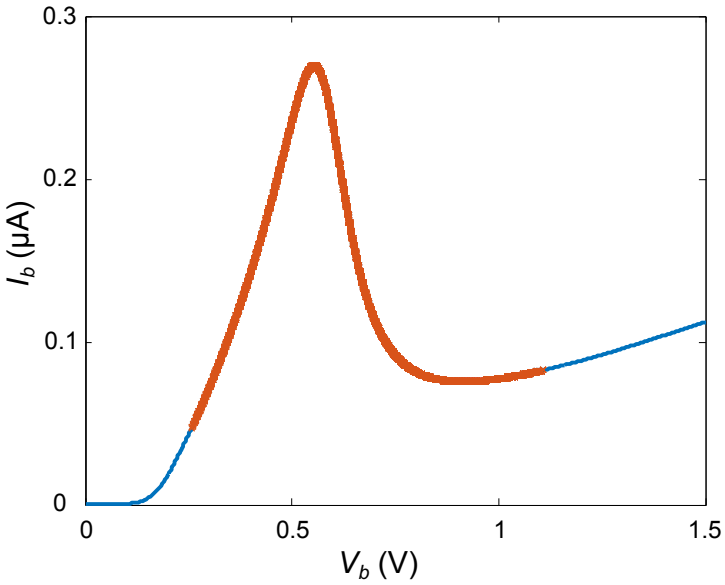

Figure 4.2: Calculated static $I_b(V_b)$ characteristics (blue curve) with $I(V)$ points plotted in time (red). The non-equilibrium behaviour matches the static curve, and thus allows a reduction in computational time.

4.2.1 Time-Development of Charge Densities, Current and Voltage

Here, we discuss the evolution of charge and current. If we initially begin with $V_b = 0$ V, then for an undoped, ungated device, $n_B = n_T = 0$, and $I_b = 0$ A. When a small $V_b > 0$ V is applied, the number of electrons in the bottom graphene layer increases, i.e. the conduction band fills up, whilst the top electrode loses an equal number of valence electrons. This shifts the chemical potentials in each layer, μ_B and μ_T, and also induces a field across the barrier as determined by Eq. (4.2). The bias voltage, $V_b = \mu_B - \mu_T + \phi$, then increases and, as the total voltage dropped around the circuit must equal V, $V_R + V_L$ must decrease. If V_R decreases, I decreases. If V_L decreases, from Eq. (4.3), we see I decreases also.

As V_b increases, I_b follows the $I_b(V_b)$ characteristics as outlined in Chapter 3. When I_b exceeds I, we see that from Eq. (4.1), the bottom electrode then loses conduction electrons, whereas the top electrode gains valence electrons. This, in turn, reduces F_b and brings the Dirac cones closer to alignment, but away from the resonant conditions, and thus I_b decreases to below I, and the oscillatory cycle begins again. The charge densities and currents do not necessarily need to return to 0 within each cycle.

In Fig. 4.3(a-d), we plot the parameters once stable oscillations have

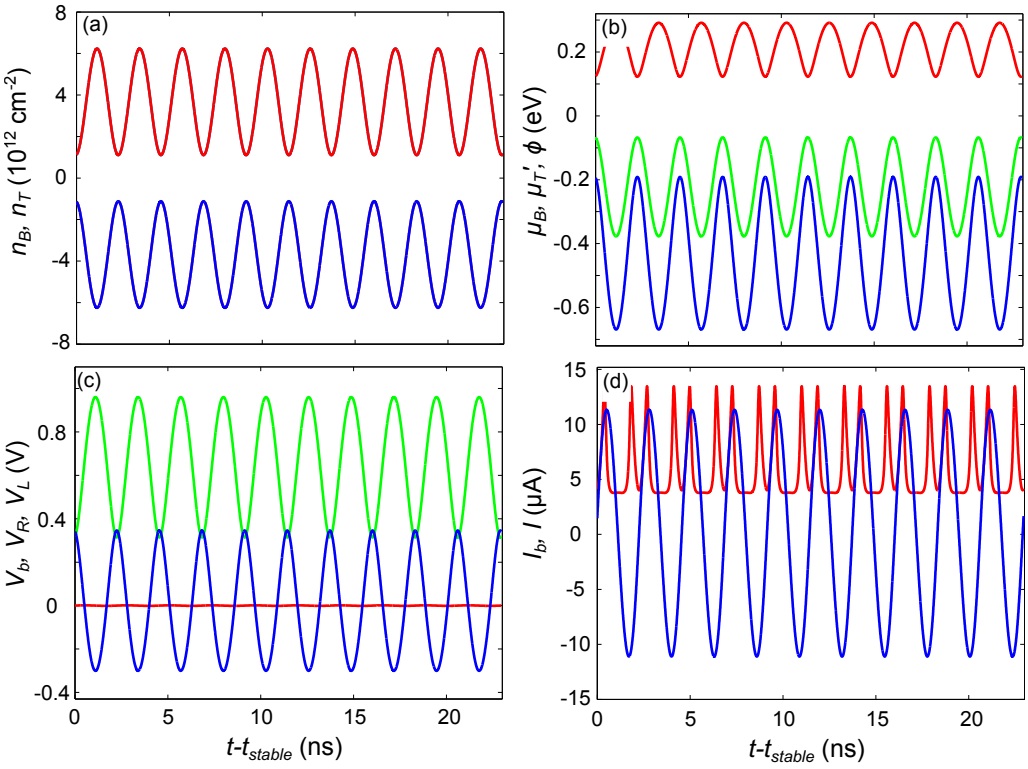

Figure 4.3: Calculated parameters once stable oscillations have been reached (a) $n_B(t)$ (red curve) and $n_T(t)$ (blue curve), (b) $\mu_B(t)$ (red curve), $\mu_T'(t)$ (blue curve) and $\phi(t)$ (green curve), (c) $V_b(t)$ (green curve), $V_R(t)$ (red curve) and $V_L(t)$ (blue curve), (d) $I_b(t) \times 50$ (red curve) and $I(t)$ (blue curve). All parameters are calculated for a circuit and device with $R = 100\ \Omega$, $L = 10\ \mu$H, and $\theta = 0.9°$.

been achieved, i.e. after some time t_{stable}. Later on in this chapter, we will discuss reaching the stable oscillations and the conditions to do so. The magnitude of the oscillations is determined by the total voltage, V, and the $I_b(V_b)$ characteristics. In Fig. 4.3(a), we see the charge densities, n_B (red) and n_T (blue) oscillating sinusoidally, and in this particular example, they do not return to 0, or exchange magnitude, within the oscillation cycle, thus the bottom electrode has additional conduction electrons, and is negatively-charged, throughout the complete cycle. The top electrode is always missing some valence electrons and is thus positively-charged. In Fig. 4.3(b), we show the chemical potentials, μ_B (red) and $\mu'_T = \mu_T + \phi$ (blue), and electrostatic potential difference across the barrier, ϕ (green), evolving in time. In Fig. 4.3(c), we find that most of the voltage is across the device, V_b (green), or across the inductor, V_L (blue), with very little dropped across the resistor, V_R (red). The peaks in V_b and V_L are in anti-phase, showing that the energy of the circuit is stored alternately between the inductor and between the device, which acts as a capacitor. In Fig. 4.3(d), we show I (blue) and I_b (red, scaled by $\times 50$), seeing that I_b is small compared to I and thus $I \approx I_C$. In addition, I varies almost sinusoidally whilst I_b traces the shape of the $I_b(V_b)$ characteristics. The peak in $|n_B|$ corresponds to the peak in μ_B and thus the peak in I. The peak of V_L is shifted from this by a phase $\phi < 90°$, as is typical in an inductive circuit [90].

Not all oscillations are sinusoidal in nature, due to the effect of quantum capacitance, as seen in Fig. 4.4(a). The device is very fast when the bias takes the chemical potential through the Dirac point in one of the two electrodes. The Fourier transform of the voltage oscillations reveals the frequency contributions to the 3.5 GHz oscillations, represented by the main peak in Fig. 4.4(b), with higher contributions from 7 GHz and 1 THz.

4.3 Small Signal Analysis of Effective Circuit

It is possible to perform a small signal analysis of the resonant tunnelling effective circuit, shown in Fig.4.1, to find an approximation for the frequency of oscillation, and to highlight the conditions required for oscillations to occur [91]. The capacitance of the device itself, C, and its resistance R_N, which is negative when biased in the NDC region, are represented here in

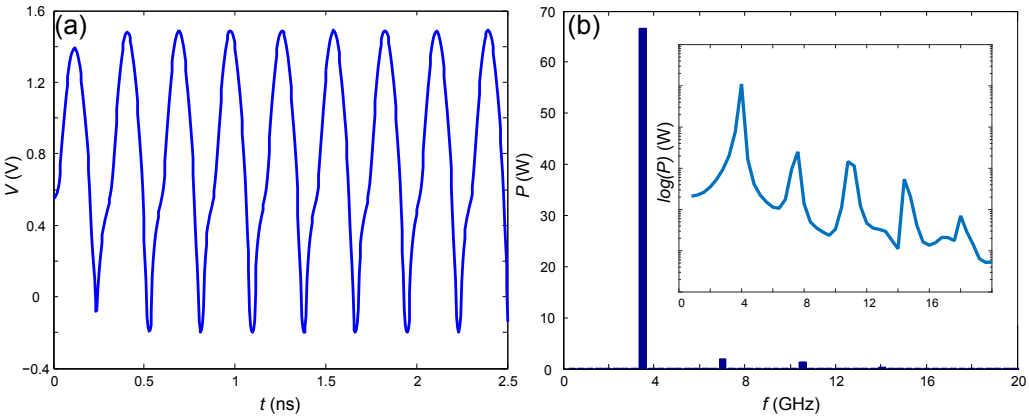

Figure 4.4: (a) Calculated $V_b(t)$ showing non-sinusoidal behaviour due to the quantum capacitance effect. (b) Power spectrum showing the frequency contributions in the oscillation, with a log-scale version inset.

parallel to each other. We take R_N to be the linear approximation of the resistance in this region, which is given by

$$R_N = \left| \frac{V_n - V_m}{I_n - I_m} \right|, \tag{4.5}$$

where V_n and I_n are the operating voltage and current, respectively, and V_m and I_m are the reference voltage and current as shown in Fig. 4.5. In a region of NDC, R_N is defined as positive. Using Kirchoff's voltage law (Eq. (4.4)) for the circuit gives:

$$V = L\frac{dI}{dt} + IR + V_n, \tag{4.6}$$

and around the circuit loop representing the device,

$$V_C = V_n \tag{4.7}$$

$$\frac{1}{C}\int I_c dt = I_n R_N. \tag{4.8}$$

Kirchoff's current law gives:

$$I = I_C + I_n. \tag{4.9}$$

Differentiating Eq. (4.6) and Eq. (4.8) with respect to time gives:

$$0 = L\frac{d^2I}{dt^2} + \frac{dI}{dt}R + \frac{dV_C}{dt} \tag{4.10}$$

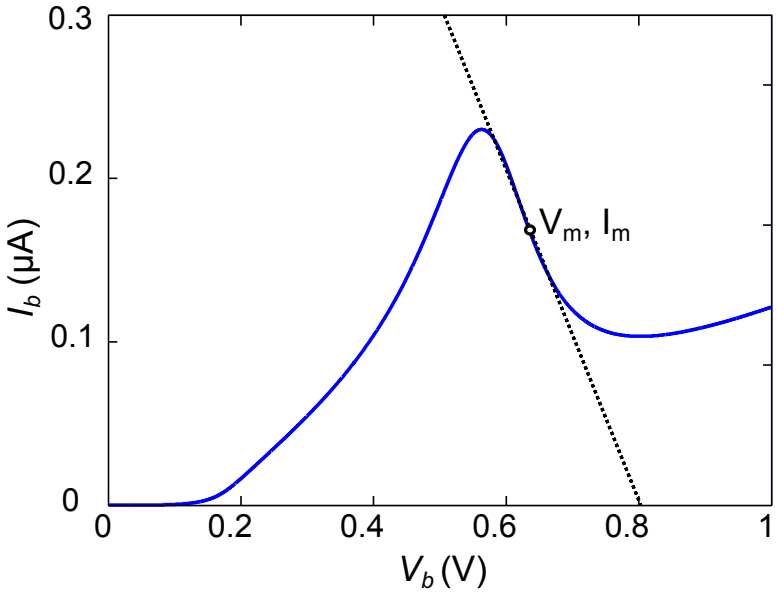

Figure 4.5: $I_b(V_b)$ characteristic calculated for the graphene-hBN-graphene diode (blue curve), with a linear approximation of the negative differential resistance (black dashed curve). The central voltage and current, V_m and I_m, in the linear region are marked by the circle.

and

$$\frac{I_C}{C} = \frac{dI_n}{dt} R_N. \tag{4.11}$$

Combining Eqs. (4.5),(4.6),(4.9), and (4.10), we obtain the relation:

$$-L\frac{d^2I}{dt^2} - \frac{dI}{dt}\left(\frac{L}{R_NC} + R\right) - I\frac{(R_N+R)}{R_NC} = \frac{1}{R_NC}(-I_mR_N - V_b - V_m). \tag{4.12}$$

This is a quadratic equation for I, for which a solution of the form:

$$I = A_1e^{\alpha_1 t} + A_2e^{\alpha_2 t} + D \tag{4.13}$$

can be assumed and inserted into Eq. (4.12), to give

$$-L\alpha^2 - \left(\frac{L}{R_NC} + R\right)\alpha - \frac{(R_N+R)}{R_NC}\alpha = 0. \tag{4.14}$$

The solution of this gives:

$$\alpha = -\frac{1}{2}\left(\frac{1}{R_NC} + \frac{R}{L}\right) \pm i\sqrt{\frac{1}{CL}\left(1 - \frac{R}{R_N}\right) - \frac{1}{4}\left(\frac{1}{R_NC} + \frac{R}{L}\right)^2}. \tag{4.15}$$

Therefore oscillations are damped by the decay term:

$$-\frac{1}{2}\left(\frac{1}{R_N C}+\frac{R}{L}\right) \tag{4.16}$$

and have frequency:

$$f^S=\frac{1}{2\pi}\sqrt{\frac{1}{CL}\left(1-\frac{R}{R_N}\right)-\frac{1}{4}\left(\frac{1}{R_N C}+\frac{R}{L}\right)^2}. \tag{4.17}$$

This can be written in terms of the natural frequency, $f_0 = 1/(2\pi\sqrt{CL})$, and a circuit factor, $Q_N = R_N\sqrt{C/L}$ (discussed in Section 4.4), to give:

$$f^s=f_0\sqrt{\left(1-\frac{R}{R_N}\right)-Q_N^{-2}\left(1-\frac{1}{4Q_N^2}\frac{R}{R_N}\right)^2}. \tag{4.18}$$

In the limit that the external resistance $R \to 0$, this reduces to:

$$f^S=\frac{1}{2\pi}\sqrt{\frac{1}{CL}-\left(\frac{1}{2R_N C}\right)^2} \tag{4.19}$$

$$=f_0\sqrt{1-Q_N^{-2}}. \tag{4.20}$$

In order for the device to oscillate, the decay term must be less than zero, i.e.

$$-\frac{1}{2}\left(\frac{1}{R_N C}+\frac{R}{L}\right)<0, \tag{4.21}$$

which rearranges to give $L > RR_N C$. Therefore, the minimum L for which oscillations occur is $L = RR_N C$. Inserting this into Eq. (4.20) gives:

$$f^S=\frac{1}{2\pi}\sqrt{\frac{1}{C^2 RR_N}-\left(\frac{1}{2R_N C}\right)^2}, \tag{4.22}$$

and, as $|R_N| >> |R|$, this reduces to the approximate dependence:

$$f^S_{max}=\frac{1}{2\pi C\sqrt{RR_N}}\propto R^{-0.5}. \tag{4.23}$$

For a more complete investigation into the conditions for oscillation and the maximum frequency available, a full signal analysis will be simulated.

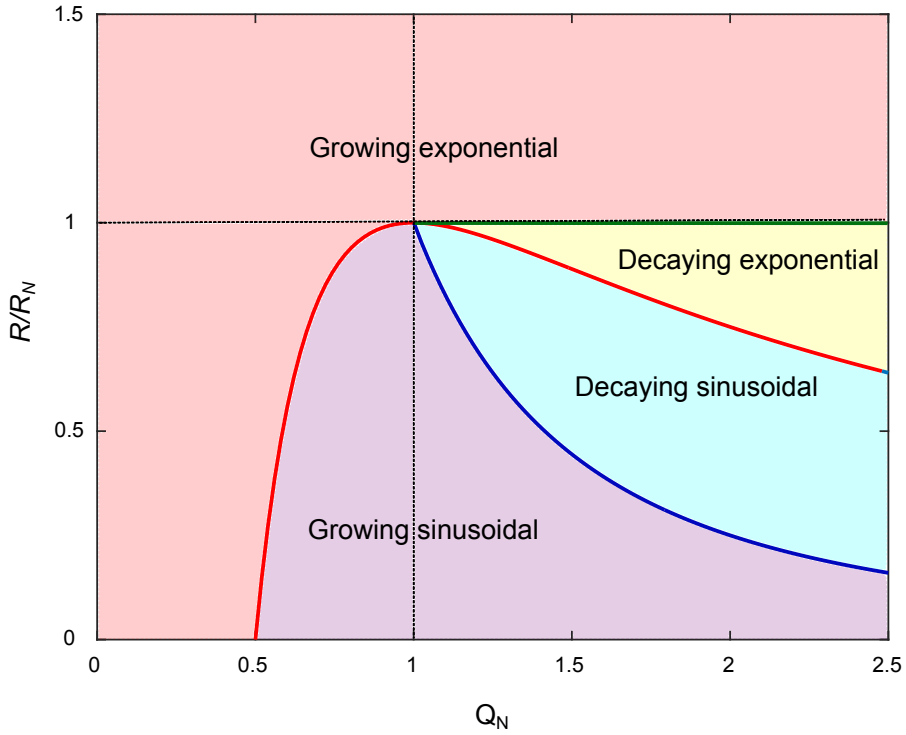

Figure 4.6: A stability chart showing the behavioural regions confined by the curve (red) $R/R_N = 2/Q_N - 1/{R_N}^2$ and curve (blue) $R/R_N = 1/{Q_N}^2$, as determined from Eq. (4.20). The growing sinusoidal region (purple) leads to the oscillations we will study here. Here, R_N is defined as positive when in a region of NDC.

This method removes the assumption of a linear R_N and allows the frequency to be calculated when biased on all parts of the $I_b(V_b)$ curve, thus providing a fuller picture of the behaviour. Later on in this chapter, we will compare the full-signal analysis results to those expected from the small-signal analysis.

4.4 Stability of Oscillations and the Q_N Factor

Following initial transient behavior, $I(t)$ either decays to a constant value or reaches stable oscillations. Fig. 4.6 shows the different regimes reached vs the resistance ratio and the Q_N factor. Three regimes result in a constant value of current after some time, t_{stable}; the growing exponent (pink), the decaying exponent (yellow), and the decaying sinusoidal (blue). The region of interest for the operation for our device lies in the growing sinusoidal (purple). We see that the circuit is unstable if the ratio of inductance to capacitance is too large, or if the ratio of R to R_N is either too small or too large.

In Fig. 4.7, the device is biased at three different voltages, points A-C as seen on the $I_b(V_b)$ curve in (a). At point A in Fig. 4.7(a), the differential resistance is positive and small, the system is stable but no oscillations occur as there is no negative resistance, which leads to the exponential decay shown in the $V(t)$ curve Fig. 4.7(e). At point B in Fig. 4.7(a), R_N is negative and large, thus leading to stable almost-sinusoidal current oscillations, as seen in Fig. 4.7(b). Finally, at C in Fig. 4.7(a), R_N is negative and small, thus leading to a stable oscillation regime, after an initial growth, as seen in Fig. 4.7(d). If a phase space diagram of the growing or decaying oscillations is constructed, i.e. plotting the $I_b(V_b)$ points in time, a spiral arises that grows inwards or outwards respectively if the oscillation is growing or decaying sinusoidally. It is also expected a region of instability exists between the growing and decaying sinusoidal regions.

4.4.1 Time-Development of Oscillations

When the device is operating within a regime leading to self-sustained oscillations, the oscillations can be defined by a frequency, f, and, time-averaged current, $\langle I(t)\rangle_t$. This time-averaged current is calculated after some

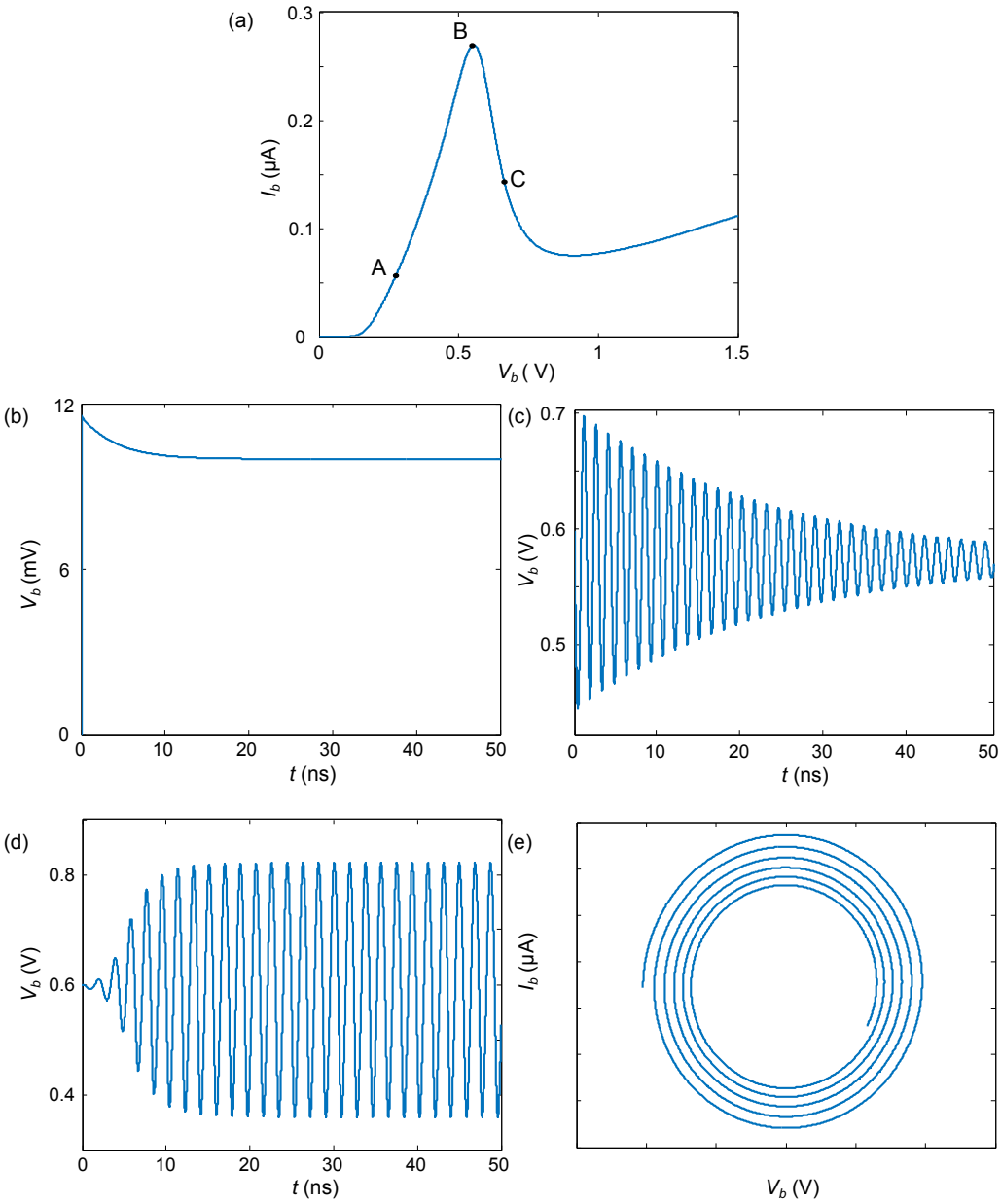

Figure 4.7: (a) Calculated $I_b(V_b)$ curve for a $\theta = 0.9°$, $N_L = 4$ device, with points A, B and C marking the V used to calculate the oscillations shown in (b-e). (b) $V(t)$ oscillations at point A show exponential decay. (c) $V(t)$ oscillations calculated at point B sinusoidally decay. (d) $V(t)$ oscillations calculated at point C show an initial growth followed by stabilization. (e) $I(V)$ points plotted in time show a spiral when sinusoidal oscillations occur, which will either spiral inwards or outwards, depending on if the oscillation is decaying or growing, respectively.

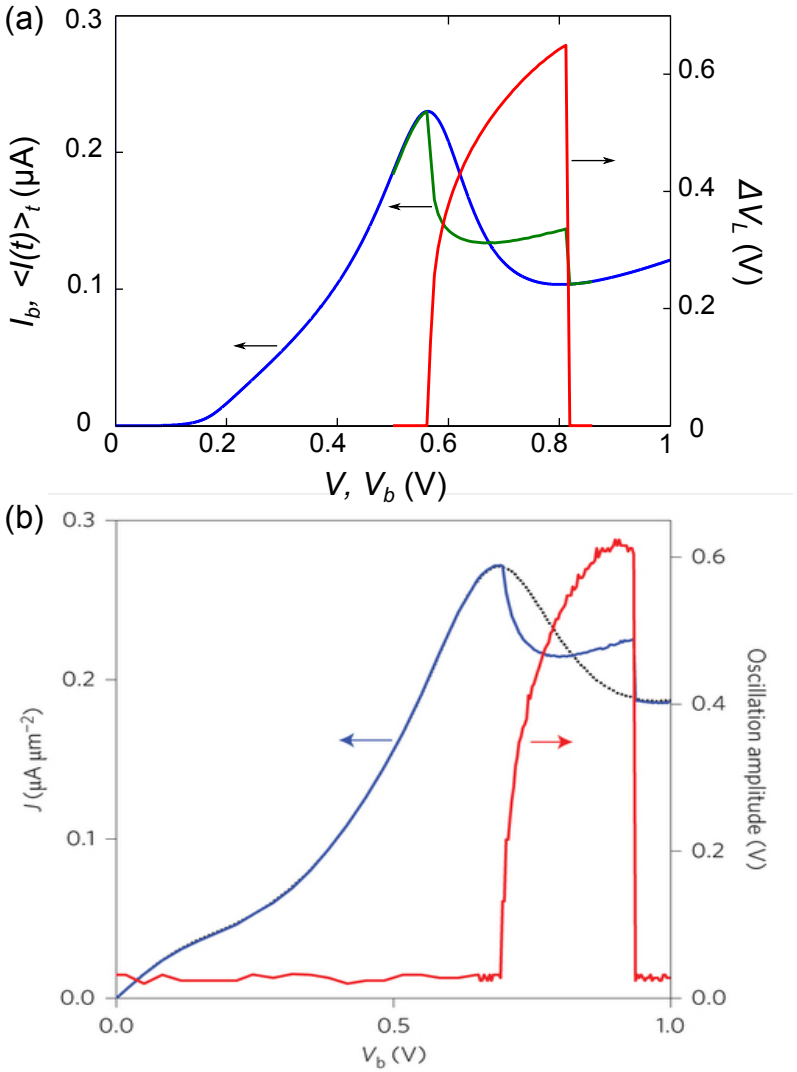

Figure 4.8: (a) Calculated equilibrium and non-equilibrium current-voltage characteristics when $\theta = 0.9°$, $L = 140$ nH and $R = 50\ \Omega$, with a $C = 65$ pF capacitor in series to represent the parasitic capacitance. Blue curve: equilibrium current-voltage characteristic $I_b(V_b)$ (left axis). Green curve: time-averaged current $\langle I(t)\rangle_t(V)$ (left axis). Red curve: peak-to-peak voltage amplitude, ΔV_L, (right axis) of the stable current oscillations. Inset: $I(t)$ plot, showing stable oscillations, with $f = 4.2$ GHz. (b) Measured experimental results from Manchester [20] from a similar resonant circuit with a GRTD device (blue curve: $\langle I(t)\rangle_t(V)$, dashed curve: static $I_b(V_b)$, red curve: ΔV_L.

time, t_{stable}, at which the magnitude of the oscillations becomes constant. In Fig. 4.8(a), we show $\langle I(t)\rangle_t$ versus V (green) and $I_b(V_b)$ (blue curve) for an undoped device, with $\theta = 0.9°$, placed in a resonant circuit with $R = 50\ \Omega$ and $L = 140$ nH. The plot reveals that when V is tuned in the NDC region ($0.55\ \text{V} < V < 0.8\ \text{V}$), $\Delta V_L = V_L^{\max} - V_L^{\min}$ (red curve) becomes non-zero indicating that self-sustained oscillations are induced. Here, $V_L^{\max/\min}$ is the maximum/minimum voltage dropped across the inductor during an oscillation period. Also, the $\langle I(t)\rangle_t$ versus V curve (green) diverges from the static current, $I_b(V_b)$, (blue) in the NDC region. This is due to asymmetric rectification of $I(t)$ in the strongly nonlinear NDC region of $I_b(V_b)$ and is typical of this type of device. When the device is biased in regions of positive differential conductance, i.e. $V < 0.55$ V or $V > 0.8$ V, oscillations are suppressed and $\langle I(t)\rangle_t$ converges to $I_b(V_b)$.

This behaviour is similar to that recently measured in a GRTD, where oscillations with $f \sim 2$ MHz were reported [20], the results from which are shown in Fig. 4.8(b). That device had high circuit capacitance due to large-area contact pads and coupling to the doped Si substrate (gate). This effect can be modelled by placing a capacitor in parallel with the GRTD. Including this large capacitance (65 pF) limits the maximum frequency, as observed [20]. When parasitic circuit capacitances are minimised, using the four contact geometry exemplified in Fig. 1.12, the only significant contribution to the total capacitance is from the graphene electrodes, as described by the charge-continuity equation. This enables us to investigate the potential of GRTDs optimised for high-frequency applications.

4.4.2 Model Validation

Measurements on the non-equilibrium behaviour of a device made in Manchester have been made [20], and here we validate our model by using the parameters of the experiment to comparing our simulated current curves with those measured. The device consisted 4 layers of hBN acting as the tunnel barrier, with the graphene electrodes misaligned by $\theta = 0.9°$. In order to model the parasitic capacitance, a 65 pF capacitor was placed in series with the GRTD to slow the oscillations down, so the effective circuit we model is represented in Fig. 4.9. From Kirchoff's and Ohm's Laws, we

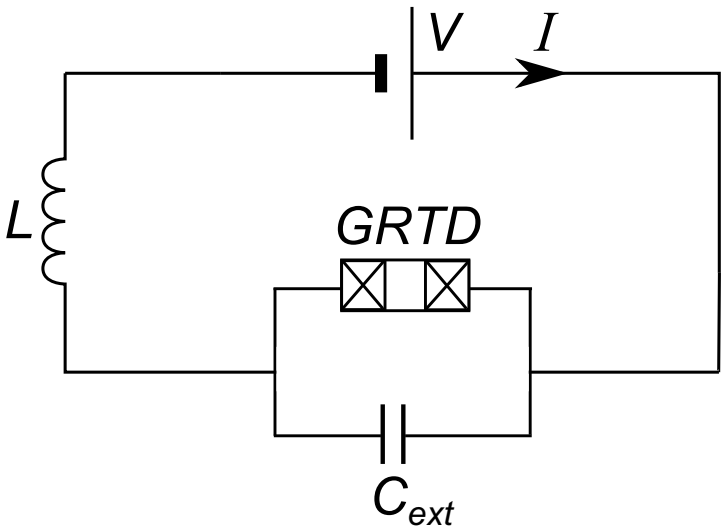

Figure 4.9: Circuit diagram of the GRTD in parallel with an external capacitor, C_{ext}. The GRTD is represented by the effective circuit in the dashed ellipse of Fig. 4.1, which contains the inherent capacitance from the graphene layer charge build up.

know:

$$V = V_C + V_L \tag{4.24}$$
$$= V_b + V_L, \tag{4.25}$$

where V_b (I_G) is the voltage (current) across the GRTD, and

$$I = I_C + I_G V_b = I_G R. \tag{4.26}$$

The time-evolution of the current and voltage:

$$I_{C_{ext}} = C_{ext}\frac{dV_{C_{ext}}}{dt}, \tag{4.27}$$
$$V_L = L\frac{dI_{C_{ext}}}{dt}, \tag{4.28}$$

can be combined with the charge continuity equations (4.1) (with I set to be I_b) to self-consistently solve for all currents, voltages and charge densities in time.

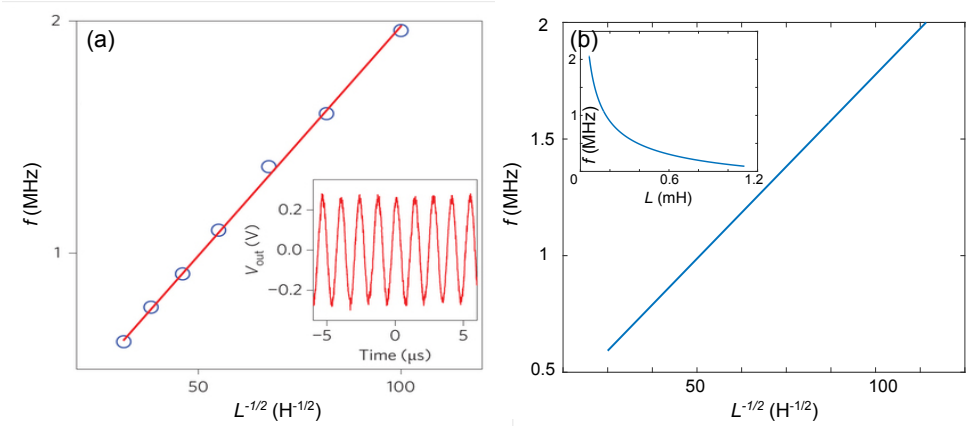

Figure 4.10: $f(L^{-1/2})$ from (a) experimental results by Mishchencko et. al [20], with an inset of measured $I(t)$ showing sinusoidal MHz oscillations. (b) Simulated results, with inset $f(L)$. Both results are for a $\theta = 0.9°$ device in series with a 65 pF capacitor and 100 Ω resistor.

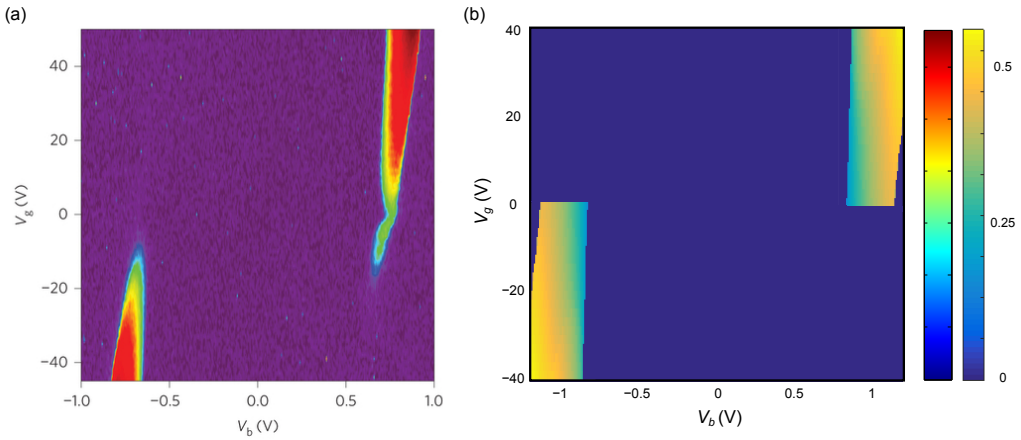

Figure 4.11: $\Delta V(V_b, V_g)$ from (a) experimental results by Mishchenko *et al.* [20] (red to yellow to violet, 0.5 V to 0.26 V to 0.03 V) (b) Simulated results for a similar device and resonant circuit.

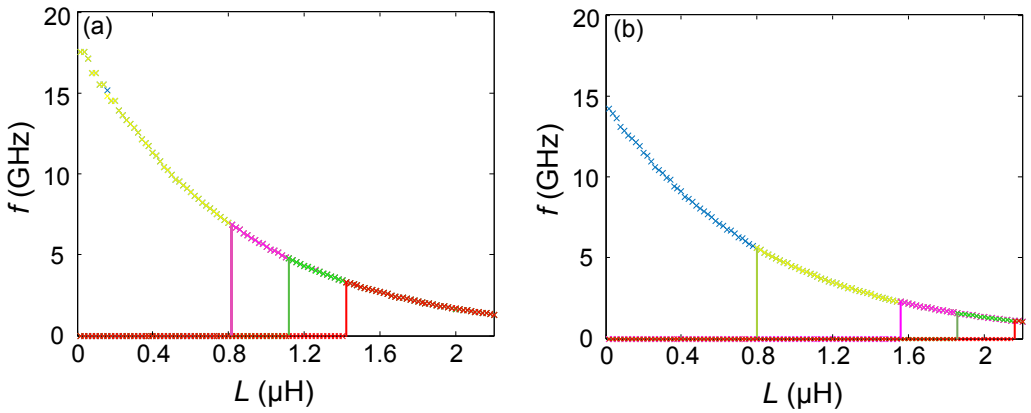

Figure 4.12: Calculated $f(L)$ for fixed values of R for (a) an aligned device, and (b) a $\theta = 0.9°$ device. $R = 1\ \Omega$ (blue), $R = 5\ \Omega$ (yellow), $R = 25\ \Omega$ (magenta), $R = 50\ \Omega$ (green) and $R = 100\ \Omega$ (red). Not all $L - R$ combinations lead to self-sustained oscillations, and these are marked by $f = 0$ GHz points.

4.5 Oscillations for an $N_L = 4$ Device

Oscillations in the MHz frequency range have been measured [20] in the current configuration, which includes an additional capacitor. But this external capacitor, introduced to the experimental set-up to slow the oscillations down to measurable frequencies, and to also represent the parasitic capacitance present within the device in the model, can be removed. The parasitic capacitance arises between the contact pads of the device and the underlying Si gate. Reducing this capacitance and that of the external circuit would allow much higher frequencies to be achieved. By constructing the device in a Maltese cross formation with four contacts, as opposed to the two initially used in [52], the capacitance can be reduced, such that the in-built capacitance from the charge densities in the Dirac cones dominates. The removal of the external capacitor allows GHz oscillations to be achieved, with the standard experimental device parameters. The highest frequencies could be achieved by fabricating the device in a slot antenna configuration, in which the slot acts as a resonator with the geometry of the slot determining the resonant frequency. Modifying the device further could potentially lead to THz oscillations, so here we investigate how best to reach this regime.

4.5.1 Circuit Parameter Investigation

Fig. 4.12 shows $f(L)$ curves calculated for $\theta =$ (a) 0°, (b) 0.9°, taking five fixed values of the dissipative resistance R. We see that the results agree well

with the expected $f \propto L^{-1/2}$ relation, and that also decreasing R unlocks the higher frequency oscillations. If the value of R is too high, the decay constant will become positive and thus the oscillations will decay; these regions are marked by the portions of the curves in Fig. 4.12 where $f = 0$ GHz. The aligned device leads to slightly higher f for the same R and L values (Fig. 4.12(a)), compared to the $\theta = 0.9°$ device (Fig. 4.12(b)), due to the change in R_N. The effects of R and L on f can be seen clearly in Figs. 4.13(a,b). Here, we see the aligned sample (a) can achieve self-sustained oscillations for a much higher range of R, and also at a slightly higher f for the same $R - L$ combination than when $\theta = 0.9°$ (b). The maximum frequency, $f_{max}(R)$ is obtained by calculating f for the smallest L for each R value that will lead to non-decaying oscillations.

Although preliminary devices are estimated to have $R \approx 100\ \Omega$, the quality of the graphene electrodes can be improved and modifications to the device design will enable even lower R to be achieved. Values of $\approx 50\ \Omega$ have recently been reported for graphene encapsulated by boron nitride [92], and also very high mobilities have been obtained in suspended graphene [93]. Therefore, the curves in Fig. 4.14 are plotted in solid for currently attainable values of R ($R >$50 Ω), and plotted in dashed for potentially achievable R. We note that modifications to the device which we will employ later, such as reducing the barrier width, lead to lower R [62] and thus allow the higher frequencies to be reached more readily.

From the small signal analysis, we see that $f_{max} \approx R^{-0.5}$. This is in close agreement with the full-signal analysis results shown in Figs. 4.13-4.14. Due to the non-linear $I_b(V_b)$ characteristics and the portion of oscillation period spent outside the central NDR region, full-signal analysis does however lead to a more reliable and accurate prediction of the frequency and current output. We therefore continue the full-signal analysis and consider the device modifications investigated in Chapter 3, to note how changes in the $I_b(V_b)$ characteristics, and thus R_N, affect the frequency output of future devices.

4.6 Barrier Thickness

In Section. 3.3, the effect of reducing the number of layers in the barrier on the static $I_b(V_b)$ characteristics was shown. It was found that the tunnel current significantly increases ($\sim 20\times$) for each atomic layer of boron nitride removed

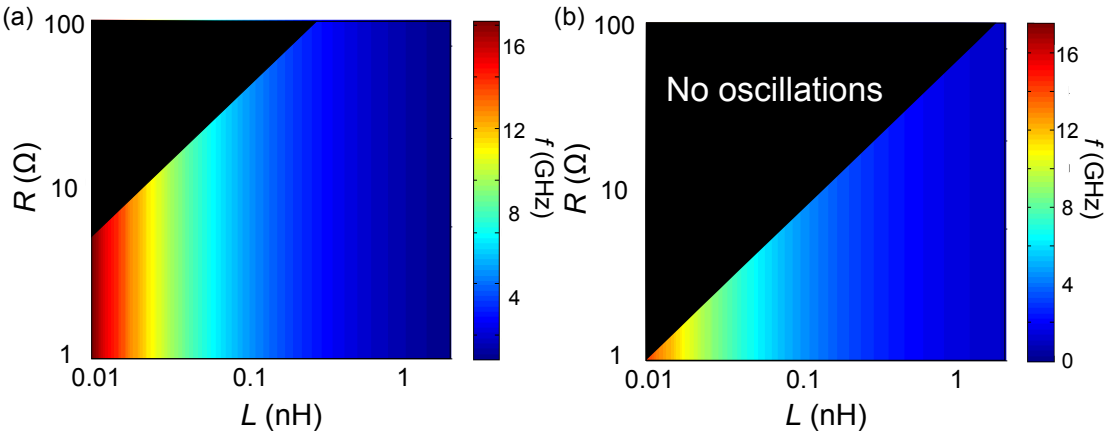

Figure 4.13: Calculated $f(L, R)$ colour maps for (a) an aligned device, and (b) a $\theta = 0.9°$ device. Black regions indicate $L - R$ combinations which do not lead to self-sustained current oscillations.

and the gradient of the $I_b(V_b)$ characteristics increased, thus decreasing the magnitude of R_N. From Eq. (4.23), we know that as R_N decreases, f^S_{max} increases. Another effect of decreasing d is the increase in geometric capacitance, $C_g = \epsilon_r \epsilon_0 A/d$. From the small signal analysis, we would therefore expect a decrease in frequency, as $f_{max} \propto 1/C$. Therefore, we have two opposing effects from the change in d. To quantify this, we can consider a change from $N_L = 4$ to $N_L = 2$. As the resonant peak occurs at almost the same voltage for both N_L values, R_N will change primarily due to the change in current peak, which, for such a barrier reduction, would be an increase of a factor of $\sim 20 \times 20 = 400$ times. Thus R_N would decrease by a factor of 400, and as $f_{max} \propto 1/\sqrt{R_N}$, f_{max} will be expected to increase by a factor of 20 due to the increase in current. The barrier width change will lead to a doubling of $C \propto 1/d$, which gives $\sim 2 \times f_{max}$ as $f_{max} \propto 1/C$. Therefore, overall, we expect a $\sim 10\times$ increase in f_{max}, with the change in current dominating over the change in capacitance.

To demonstrate the exact effect on the frequency, we calculate $f_{max}(R)$ for three barrier widths, $N_L = 2, 3, 4$, as shown in Fig. 4.15. Reducing d produces a large gain in f_{max} for all R. For example, f_{max} for a device with $N_L = 2$ is at least an order of magnitude higher than when $N_L = 4$, as expected, (e.g. for $R = 50\ \Omega$, f_{max}= 26 GHz when $N_L = 2$, compared to $f_{max} = 1.8$ GHz when $N_L = 4$).

In principle, any barrier width is attainable, but for $N_L = 1$, the wavefunctions overlap too much, such that the tunnelling effect is not the main

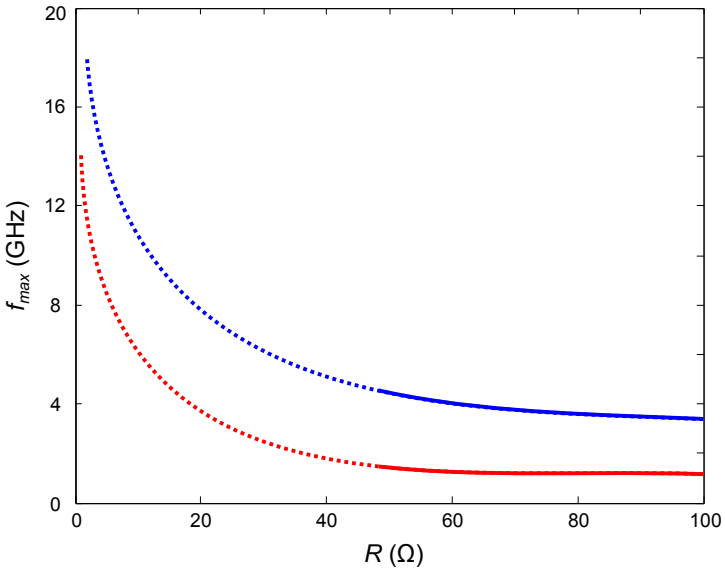

Figure 4.14: Calculated $f_{max}(R)$ curves for an aligned device (blue curve) and a $\theta = 0.9°$ device (blue curve), for currently-achievable (solid curve) and potentially-achievable (dashed curve) values of R.

contributing factor to the value of the current and thus the resonant tunnelling effect is lost. $N_L > 4$ can also be easily achieved, but the tunnelling current would be reduced again by a factor of 400 for each layer added, and would thus be too small for the desired operation and the resulting oscillation frequencies would be very low. As the 2-layer device offers the highest frequency and current output, we will continue to investigate the effect of other parameters on the $N_L = 2$ device only.

4.7 Chemical Doping of the Graphene Layers

In Section 3.7, we saw that doping the bottom graphene layer lead to an increase in current and a shift of the resonant peak to higher voltages, due to the shift in resonant conditions. Here, we investigate the effect of these changes on the frequency response of the device. As the magnitude of R_N decreases with increasing n_B^D, we expect from the small signal analysis that the frequency of oscillation will increase, as $f_{max} \propto 1/\sqrt{R_N}$.

The doping also affects the overall capacitance of the device, as seen by the introduction of the quantum capacitance term in Section 2.2. When $\mu_{B,T}$ passes through the Dirac point, $C_Q \to 0$ and, hence, $C \to 0$, suggesting

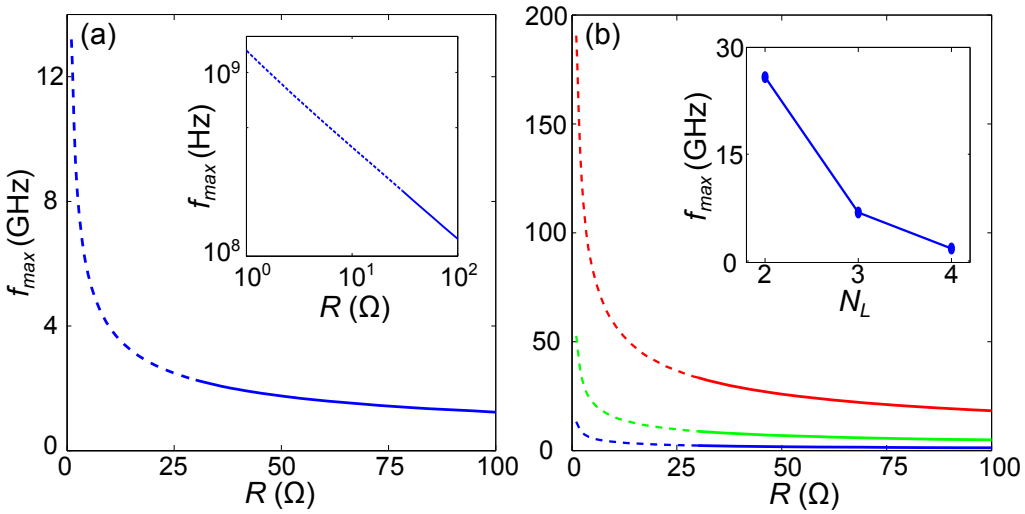

Figure 4.15: (a) $f_{max}(R)$ curves calculated for an undoped device with $N_L = 4$. The solid line represents the range of R obtainable in the current device design and the dashed line corresponds to R values which could be achieved by new device designs. Inset: $\log(f_{max})$ vs $\log(R)$ reveals a linear relationship. (b) Calculated $f_{max}(R)$ for an undoped device with number of barriers, $N_L = 2$ (red curve), 3 (green curve) and 4 (blue curve). Inset: $f_{max}(N_L)$ at 50 Ω for the undoped samples. All devices have $\theta = 0.9°$.

that the RC time constant of the device could be reduced. In practice, C_Q is small for only a small fraction of the oscillation period and so its effect on the fundamental frequency of $I(t)$ is negligible.

Fig. 4.16(a) shows the $I_b(V_b)$ curve calculated for undoped (red curve) and doped (green curve) devices and (b) shows the $f_{max}(R)$ curves, which reveal that the doped device is faster for all R. Fig. 4.16(b) inset shows that f_{max} increases monotonically with ρ_{BD}/e when $R = 50$ Ω; f_{max} increases by a factor of 1.3 when ρ_{BD}/e is increased to 10^{13} cm^{-2} (and $f = 32$ GHz) from $\rho_{BD}/e = 0$ ($f = 26$ GHz).

4.8 Misalignment of the Graphene Layers

In Section. 3.5, the effect of misalignment on the $I_b(V_b)$ characteristics was shown, and it was found that an increasing misalignment angle between the graphene layers leads to a decrease in current, and a shift of the resonant conditions to higher V_b. In Fig. 4.17(a), we show the $I_b(V_b)$ characteristics for a doped ($\rho_{BD}/e = 10^{13}$ cm^{-2}) device when $\theta = 0°$. For such doping levels, the valley current is close to 0 for all θ, thus the PVR is consistently large. Consequently, the increase in current magnitude, which results from

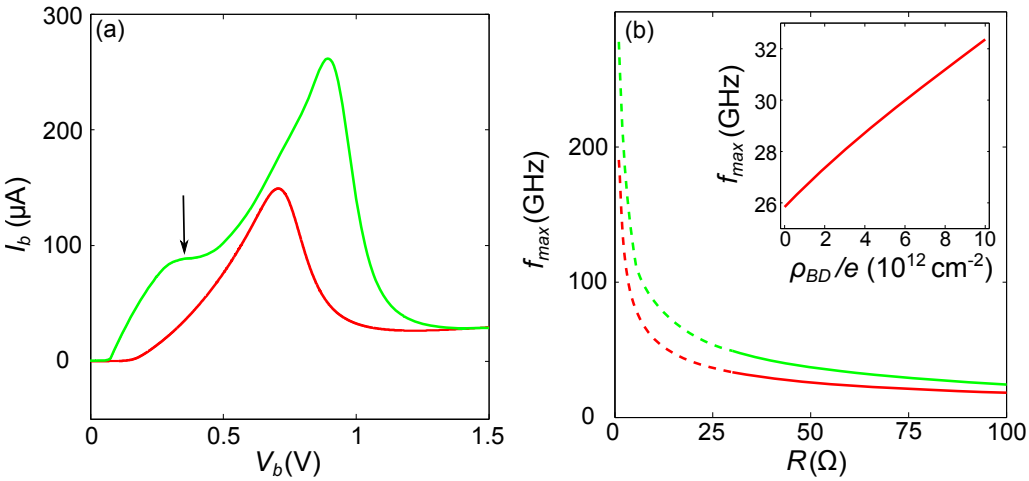

Figure 4.16: (a) Calculated $I_b(V_b)$ characteristics and (b) $f_{max}(R)$ curves for a doped device (green curve, $\rho_{BD}/e = 10^{13}$ cm^{-2}) and an undoped (red curve) device, with $N_L = 2$. The arrow in (a) shows the shoulder that arises due to the quantum capacitance effect. In (b), the solid part of the curves represents currently achievable resistances and thus frequencies, whereas the dashed part of the curve represents the f_{max} that could be achieved if the resistance can be reduced to that value. Inset in (b): $f_{max}(\rho_{BD}/e)$ calculated when $R = 50\Omega$.

alignment, leads to higher frequencies without the reduction of power that is associated with undoped samples. The $\theta = 0.9°$ device has a much lower current, leading to the $R_N(\theta)$ relations shown in Fig. 4.17(b). Here, we see the undoped device (cyan curve) has a much higher negative resistance for all misalignment angles than the doped device (magenta curve). From the small signal analysis in Eq. (4.23), we see that $f_{max} \propto R_N^{-1/2}$, and thus we can expect the doped devices to give higher frequency oscillations, and similarly for the aligned samples, as R_N is minimal at $\theta = 0°$. The full signal analysis results, shown in Fig. 4.17(c-d), agree with these predictions, showing that perfect alignment could increase f_{max} by a factor of ~ 2, i.e. for $R = 50\ \Omega$, $f_{max} = 65$ GHz when $\theta = 0°$ compared to 32 GHz when $\theta = 0.9°$. The numerical results diverge from the small signal analysis power law of $f_{max} \propto R^{-0.5}$, as seen in Fig. 4.17(d) (black curve). As R_N becomes small, as it becomes necessary to vary V to induce oscillations.

4.9 Barrier Composition

As seen in Section 3.8, reducing the barrier height, Δ, via a change in the barrier material, can lead to an increase in I_b. This reduces R_N and thus leads to higher frequencies. For the doped, misaligned 2-layer device, frequencies

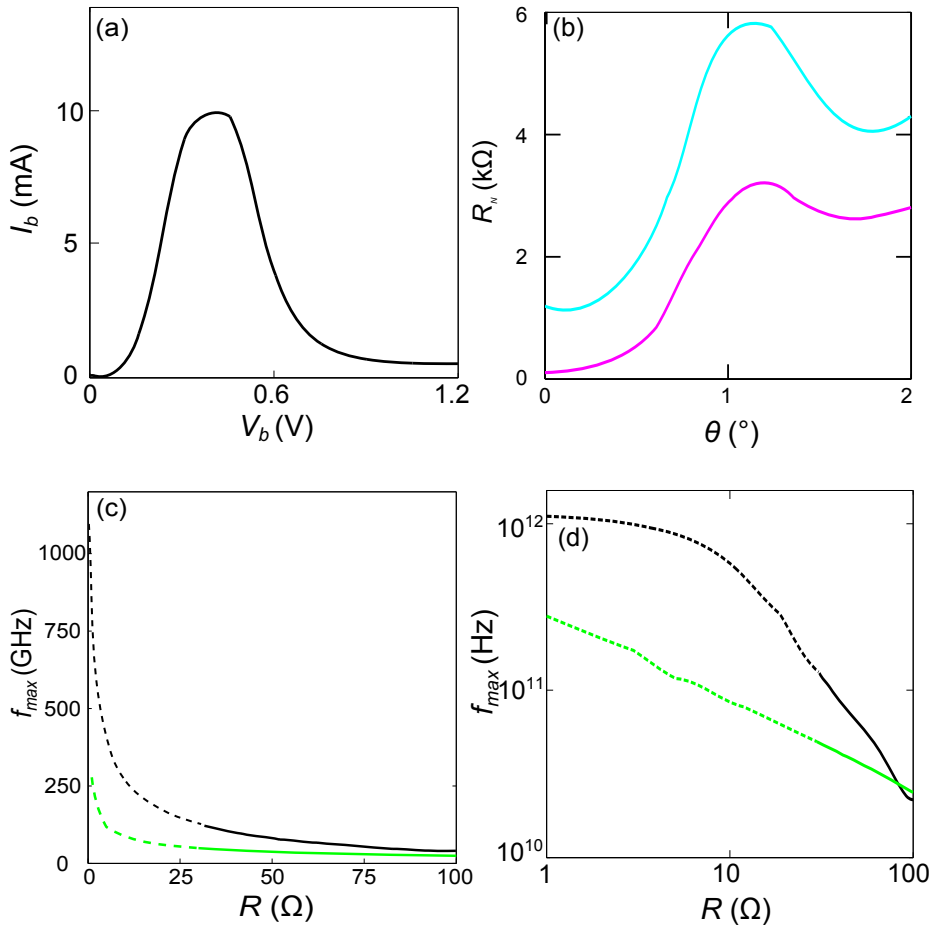

Figure 4.17: (a) $I_b(V_b)$ curve calculated for a device with $\theta = 0°$, $N_L = 2$ and $\rho_{BD}/e = 0\ \mathrm{cm}^{-2}$. (b) Calculated $R_N(\theta)$ curve for the device in (a) (magenta curve) and for the matching undoped device (cyan curve). (c-d) Calculated $f_{max}(R)$ and $log(f_{max}(R))$ for the doped (black curve) and undoped device (green curve) over ranges of R values corresponding to existing samples (solid parts of the curves) or attainable in future experiments (dashed curves).

are found to be over noticeably higher when the barrier is composed of WS_2 rather than hBN, as seen in Fig. 4.18. Changing the barrier material also changes C via the relative permitivity of the barrier layer, ϵ_r. However, this change will be small in comparison to the change in the current. The relative permitivity of WS_2 is 6.1 [94], as opposed to 3.9 for hBN. This is not implemented into the model below as there are no devices in which to compare the current with, and thus the scaling may no longer be correct.

Due to the lower barrier height in WS_2, care must be taken to avoid entering the conduction regime, i.e. electrons passing over the barrier rather than tunnelling. If this happens, the effect of resonant tunnelling and thus NDC is lost. With a lower barrier height, the effect of tilting due the field

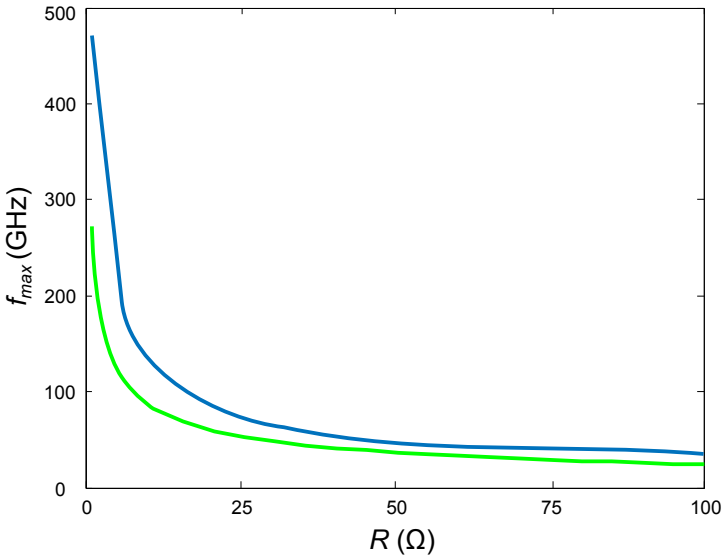

Figure 4.18: Calculated $f_{max}(R)$ curve for a $N_L = 2$, $\rho_{BD}/e = 0$ cm^{-2}, $\theta = 0.9°$ device with a barrier composed of hBN (green) and WS_2 (blue) layers.

will affect the $I_b(V_b)$ characteristics more also. We will therefore continue to consider hBN rather than WS_2 to ensure the current across the barrier is arising due to tunnelling.

4.10 Conclusion

We find the highest frequencies occur when the current across the barrier is increased, thus reducing R_N. This is achieved by minimizing the barrier width, i.e. to $N_L = 2$, and by aligning the graphene layers. The use of chemical doping to shift the resonant conditions to allow more electrons to tunnel resonantly also maximizes the frequency. THz oscillations are achievable with an optimized device design to reduce lossy resistance and external capacitance, for example, by having four contacts in a Maltese cross arrangement rather than two overlapping contacts with long leads. The use of doped, high-quality graphene in combination with careful alignment of the graphene lattices, will lead to the highest frequency output with a good output current magnitude. The device area could also be reduced to further increase the frequency, as $f_{max} \approx 1/C$ and reducing the area would reduce $C = \epsilon_0 \epsilon_r A/d$. However, this also leads to a loss in current. This compromise could be overcome by having an array of GRTDs in series to increase the output power.

Chapter 5

Moiré Patterns from Graphene on Hexagonal-Boron Nitride

Due to the lattice constant mismatch between the crystalline lattice of graphene and that of hexagonal boron nitride, an angle-dependent moiré pattern can arise when a layer of graphene is placed on top of a layer of hBN [95]. In this chapter, the effect of this additional moiré potential electron tunnelling is investigated. It is found that secondary Dirac points emerge in the band structure, and their effect on the $I_b(V_b)$ characteristics is analysed.

5.1 Moiré Patterns

During fabrication of early GRTDs, the hBN layers making up the barrier and the substrate of the device, and the graphene layers were intentionally misaligned, such that the graphene and hBN layers are effectively decoupled and moiré pattern effects are negligible. However, care can be taken to bring the layers into alignment [35, 36, 96]. Here, we consider a bottom graphene layer that is misaligned by an angle $\phi_M < 5°$ relative to the base hBN layer, and the effect of the moiré potential this will induce. For these small ϕ_M values, we enter into a regime where the electrons will be significantly affected by the arising moiré potential, and by small changes in ϕ_M, as seen in Fig. 5.1. In Fig. 5.1(a), the lattices are aligned and we see a clear moiré potential arising. Rotating the layers with respect to each other by $\phi_M = 3°$ causes a complete rotation of the moiré plaquette, see Fig. 5.1(b), which marks out the repeatable component of the potential. Further rotation to 6° causes a smaller change in the potential, Fig. 5.1(c), and when the lattices

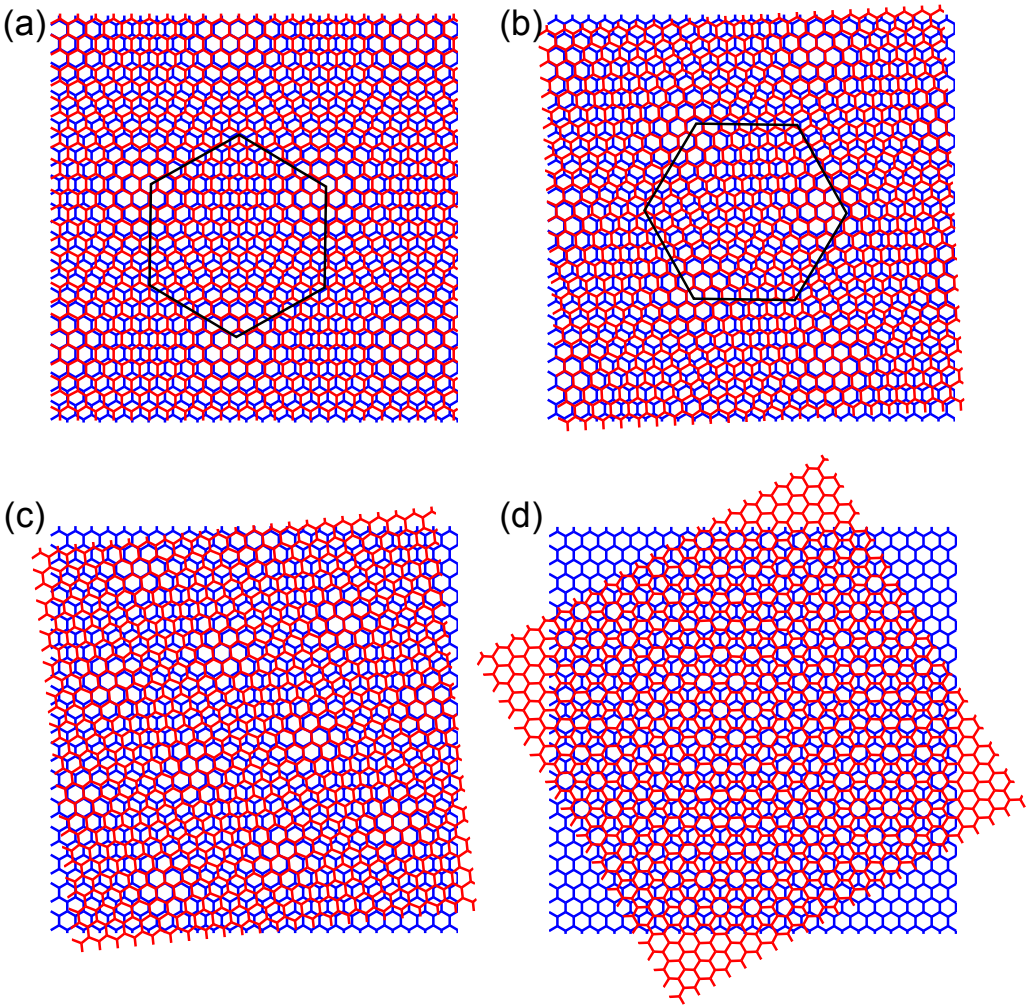

Figure 5.1: Moiré pattern from hexagonal-boron nitride (red) on graphene (blue), with an exaggerated lattice constant difference (10%) for (a) $\phi_M = 0°$, (b) $\phi_M = 3°$, (c) $\phi_M = 6°$, and (d) $\phi_M = 30°$. The black hexagons mark the Moiré plaquette.

are highly misaligned (30°, Fig. 5.1d), the potential is negligible. Recent experiments have demonstrated well-defined moiré patterns in graphene on crystalline lattices [68, 96, 97].

It is known from the Schrödinger equation that when nearly free electrons propagate through a weak periodic potential, a bandgap opens near the reciprocal lattice points, i.e. the edge of the Brillouin Zone [98]. However, due to the chirality of the massless Dirac fermions in graphene, the opening of the bandgap is prevented, and instead a new Dirac point appears in the band structure [99–102], at an energy determined by the moiré wavelength [96]. These additional points are known as *superlattice Dirac points*.

5.1.1 Moiré Wavelength and Angle

The lattice constant of hBN is 1.8% larger than that of graphene and thus, for certain angles, a noticeable moiré pattern will emerge [96]. Here, we construct an expression for the moiré pattern wavelength, λ, in terms of the relative rotation between the hBN and graphene layers, ϕ_M. If we take the reciprocal lattice vector of graphene along the x-axis to be:

$$\mathbf{g} = \frac{2\pi}{a}(1, 0), \tag{5.1}$$

where a is the lattice constant of graphene, then the corresponding reciprocal lattice vector for hBN is:

$$\mathbf{b} = \frac{2\pi}{(1+\delta)a}(\cos\phi_M, \sin\phi_M), \tag{5.2}$$

where $\delta = 0.018$ is the lattice mismatch. A vector, $\mathbf{m}$, connecting the hBN reciprocal lattice vector to the graphene reciprocal lattice vector can be constructed as:

$$\begin{aligned} \mathbf{m} &= \mathbf{g} - \mathbf{b} \\ &= \frac{2\pi}{a}\left(1 - \frac{\cos\phi_M}{1+\delta}, \frac{-\sin\phi_M}{1+\delta}\right). \end{aligned} \tag{5.3}$$

Therefore, the wavelength of the moiré pattern, $\lambda = \frac{2\pi}{|\mathbf{k}|}$, can be calculated as:

$$|\mathbf{k}| = \frac{2\pi}{a}\sqrt{\left(1 - \frac{1-\cos\phi_M}{1+\delta}\right)^2 + \left(\frac{\sin\phi_M}{1+\delta}\right)^2} \tag{5.4}$$

to give:

$$\lambda = \frac{(1+\delta)a}{\sqrt{2(1+\delta)(1-\cos\phi_M) + \delta^2}}. \tag{5.5}$$

From Eq. (5.3), we can see that the relative rotation angle, θ_M, of the moiré pattern with respect to the graphene lattice is given by:

$$\tan\theta_M = -\frac{m_y}{m_x} = \frac{\frac{\sin\phi_M}{1+\delta}}{1 - \frac{\cos\phi_M}{1+\delta}}, \tag{5.6}$$

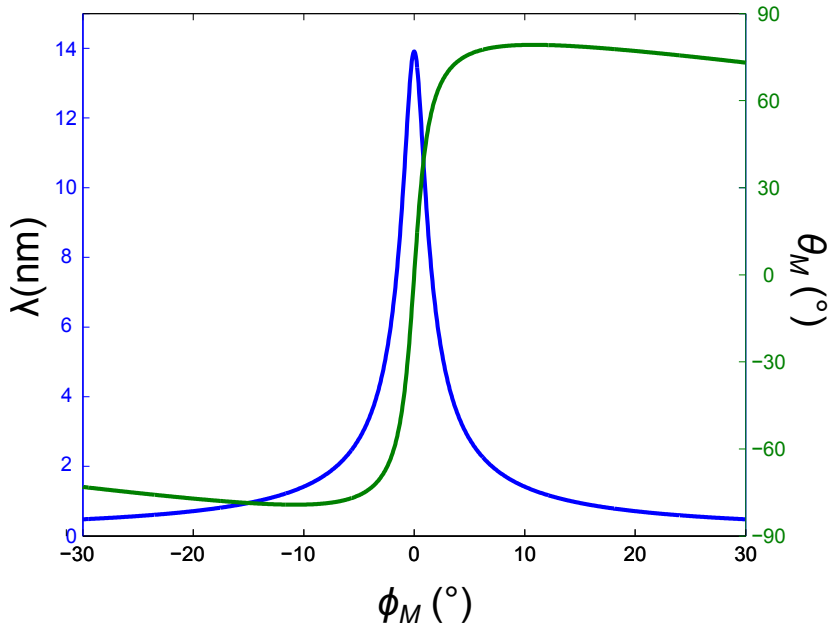

Figure 5.2: Wavelength, λ, of the moiré pattern (blue curve, left axis) and relative rotation angle, θ_M, (green curve, right axis) as functions of the angle between the graphene and the hBN.

which can be simplified to:

$$\tan\theta_M = \frac{\sin\phi_M}{(1+\delta) - \cos\phi_M}. \tag{5.7}$$

5.1.2 Moiré Pattern Properties

The moiré pattern depends on the rotational angle between the boron nitride and the graphene layers, ϕ_M. In Fig. 5.2, we see the effect of ϕ_M on the moiré wavelength, λ, and the relative rotation angle, θ_M. The maximum value of $\theta_M = 80°$ occurs when $\phi_M = 11°$, and the maximum possible moiré wavelength is ~ 14 nm, which occurs when $\phi_M = 0°$. The moiré pattern depends on the substrate material used, as the lattice constant will affect λ. Here, all calculations are performed for hBN.

5.2 Construction of the Brillouin Zones of Graphene

In order to calculate the $I_b(V_b)$ characteristics for a device with a moiré pattern, we must calculate the perturbed density of states and the band

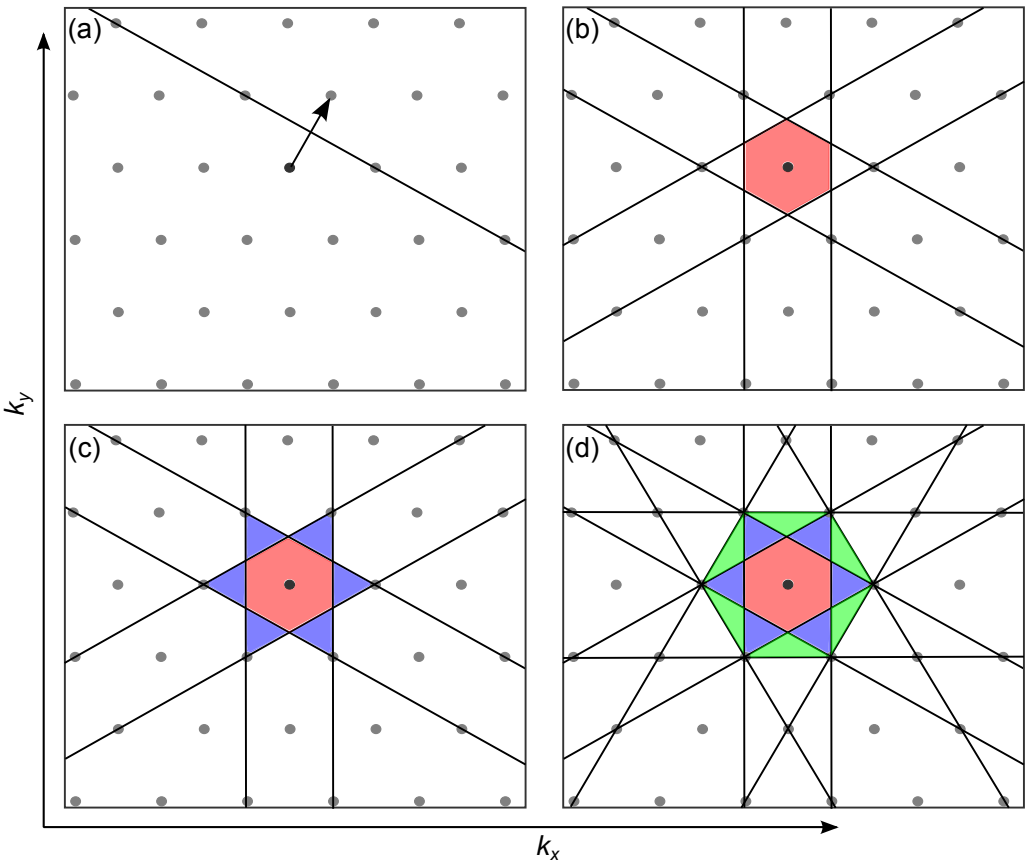

Figure 5.3: The construction of the first three Brillouin Zones in reciprocal space. (a) A Bragg vector is drawn between two sites, which are shown as dots. (b) The first Brillouin Zone (red) lies between the first six Bragg vectors. (c) The second Brillouin Zone (blue). (d) The third Brillouin Zone (green).

structure. To do this, the Brillouin zones must be defined, which can be done geometrically as described below.

Firstly, the reciprocal lattice must be constructed from the reciprocal lattice vectors, found from the real space vectors. Choosing a reciprocal lattice point (all are equivalent), we construct the first Brillouin Zone by drawing arrows from this point to all its nearest neighbours (which is the reciprocal lattice vector itself), then drawing lines to bisect these arrows. This perpendicular bisector is the Bragg Plane, Fig. 5.3(a). The first Brillouin Zone, shaded in red in Fig. 5.3(b), is the space enclosed by the first six Bragg planes. The second Brillouin Zone (blue, Fig. 5.3(c)) is the remaining area encompassed by the first set of Bragg planes. The third Brillouin Zone (green, Fig. 5.3(d)) is then constructed by drawing the Bragg planes corresponding to the next-nearest neighbours and so on.

The construction of the first six Brillouin Zones is plotted in Fig. 5.4(a-

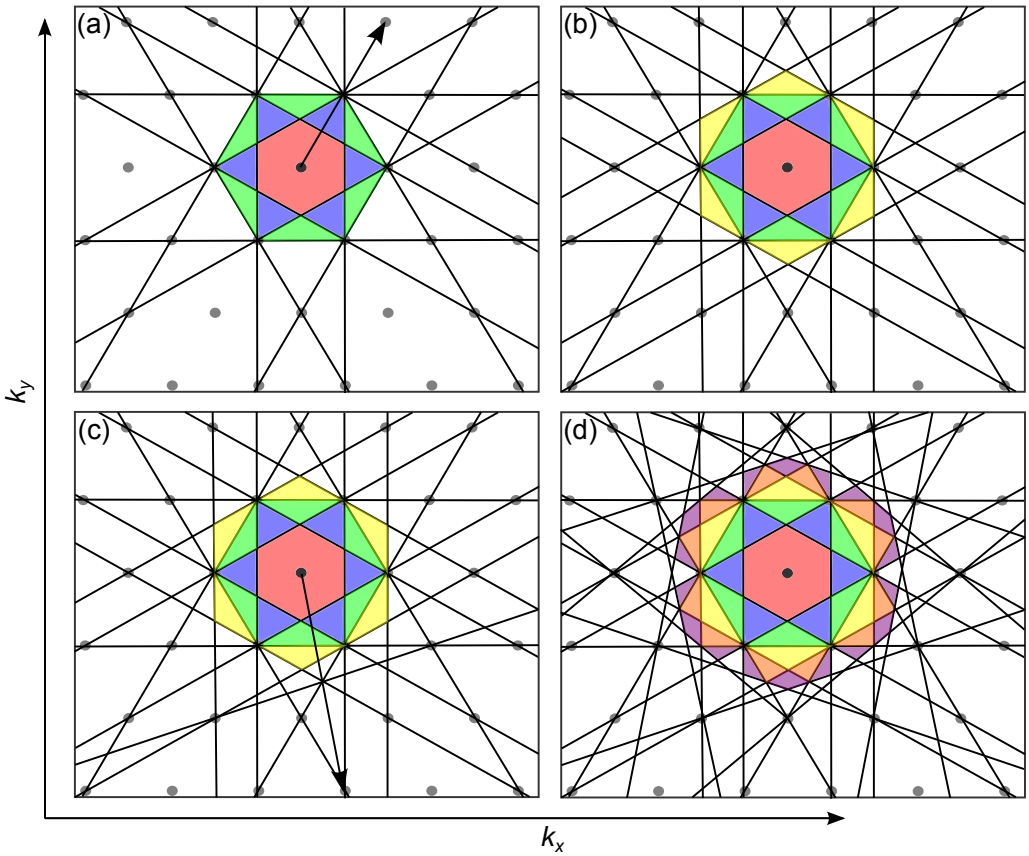

Figure 5.4: The next Brillouin Zones are constructed by drawing more perpendicular bisector lines to construct the next set of Bragg planes. (b) The fourth Brillouin Zone (yellow). (c) The fifth Brillouin Zone (orange). (d) The sixth Brillouin Zone (purple).

d). In order to calculate further Brillouin zones, and thus higher energies in the band structure, the next-nearest neighbours and beyond can be considered. However, the geometrical approach to constructing the Brillouin zones becomes time-consuming and difficult to perform computationally. It is found that the central equation, discussed further in the next section, offers a much easier alternative.

An interesting point to note is that, as the reciprocal lattice is periodic, there exists for any point outside of the first Brillouin Zone, an equivalent point within the first Brillouin Zone, with the two being related by a unique translational reciprocal lattice vector. Each zone contains every single physically distinguishable point that is contained in the first zone, and each zone has the same total area. Therefore, each zone can thus be translated (folded) back into the first Brillouin Zone, as demonstrated in Fig. 5.5(a-d).

5.3 The Central Equation

As in Chapter 1, the electrons in the device can be described by the Schrödinger equation,

$$H\psi_n(\mathbf{r},\mathbf{k}) = \left[-\frac{\hbar^2}{2m}\nabla^2 + U(\mathbf{r})\right]\psi(\mathbf{r},\mathbf{k}) = E_n\psi_n(\mathbf{r},\mathbf{k}), \tag{5.8}$$

for a given wavevector, $\mathbf{k}$, and band index, n. Here, $U(\mathbf{r}) = U(\mathbf{r}+\mathbf{T})$ is a periodic moiré potential, with $\mathbf{T}$ being the lattice vector over which the potential repeats. This can be written as a Fourier transform,

$$U(\mathbf{r}) = \sum_{\mathbf{G}_\alpha} U_{\mathbf{G}_\alpha} e^{i\mathbf{G}_\alpha\cdot\mathbf{r}}, \tag{5.9}$$

in terms of reciprocal lattice vectors, $\mathbf{G}_\alpha$.

The effective Hamiltonian at low energies is:

$$H_0(\mathbf{k}) = \hbar v_F \left(k_x\sigma_x + k_y\sigma_y\right), \tag{5.10}$$

where $\sigma_{x,y}$ are Pauli matrices. This gives the unperturbed eigenstates and

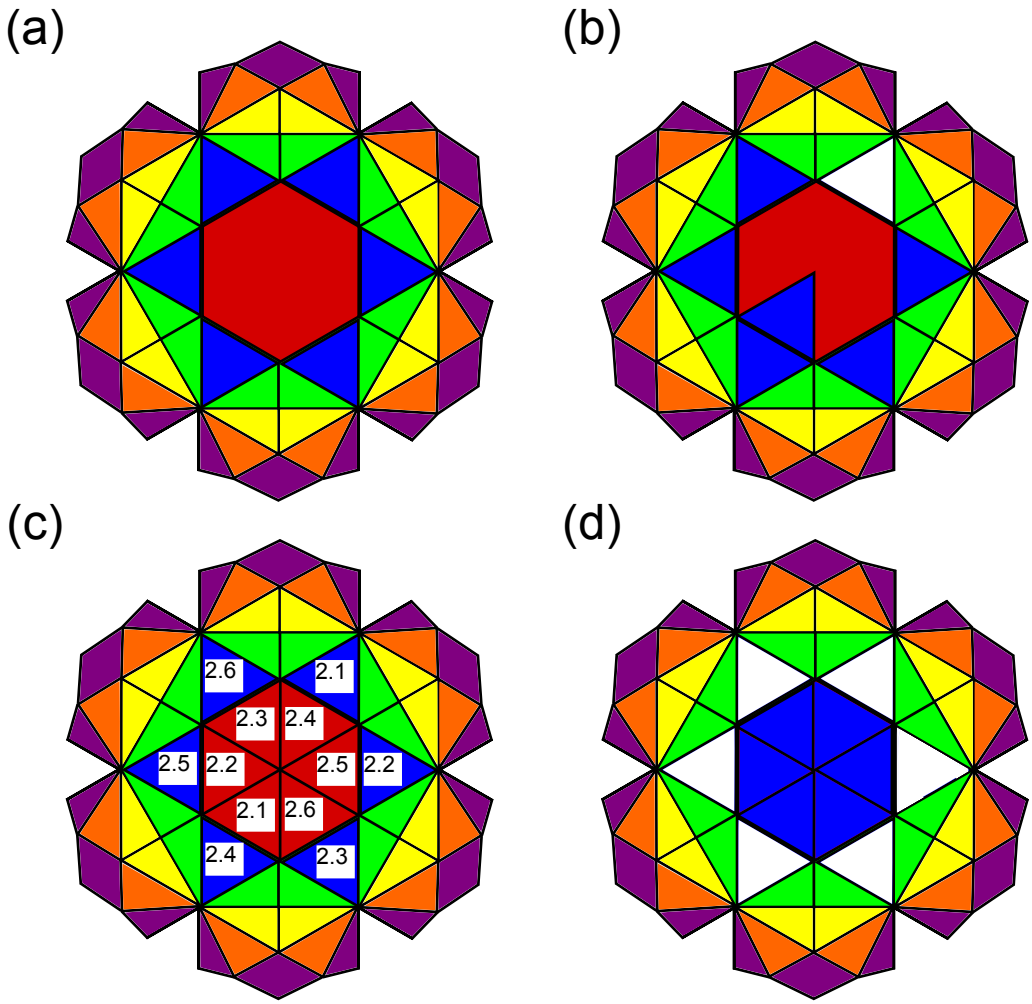

Figure 5.5: (a) The first six Brillouin Zones (BZ) of graphene. (b) Folding the 2nd BZ (blue) into the 1st BZ (red) requires each segment to be transposed by its corresponding reciprocal lattice vector, $\mathbf{G}$. In this case, we see a segment (labeled 2.1) from the 2nd BZ which is related to a point in the 1st BZ by $\mathbf{G}_1$, which when transposed by this lattice vector, sits inside the 1st BZ. (c) The segments can be folded to their corresponding area within the 1st BZ. (d) Once folded, the 2nd BZ fits exactly into the 1st BZ.

eigenvalues,

$$\psi_0(\mathbf{k}, s) = \frac{1}{\sqrt{2\Omega}} e^{i\mathbf{k}\cdot\mathbf{r}} \begin{bmatrix} 1 \\ s e^{i\theta_{\mathbf{k}}} \end{bmatrix}, \tag{5.11}$$

$$E_0(\mathbf{k}, s) = s\hbar v_F k, \tag{5.12}$$

where $s = \pm 1$ denotes the conduction and valence band, respectively, and Ω is the cell area.

The first six $\mathbf{G}_\alpha$ vectors describe the potential in Eq. (5.8), so, the perturbed Hamiltonian can be approximated as:

$$H(\mathbf{k}) = \hbar v_F \left(k_x \sigma_x + k_y \sigma_y\right) + \sum_{\alpha=1}^{6} U_{\mathbf{G}_\alpha} e^{i\mathbf{G}_\alpha \cdot \mathbf{r}} \mathrm{I}, \tag{5.13}$$

where I is the identity matrix. The amplitude of the periodic potential, $U_{\mathbf{G}_\alpha}$, can be obtained using second-order perturbation theory. Using the unperturbed eigenstates, we find:

$$\langle \psi_0(\mathbf{k}, s) | U(\mathbf{r}) | \psi_0(\mathbf{k}', s) \rangle = \sum_{\alpha=1}^{6} \frac{1}{2} U_{\mathbf{G}_\alpha} e^{i\mathbf{G}_\alpha \cdot \mathbf{r}} \left(1 + e^{i(\theta_{\mathbf{k}'} - \theta_{\mathbf{k}})} \delta_{\mathbf{k}, \mathbf{k}'+\mathbf{G}}\right). \tag{5.14}$$

As the wavefunction can be written as an expansion of plane waves,

$$\psi(\mathbf{r}, \mathbf{k}) = \sum_{\mathbf{k}} C_{\mathbf{k}} e^{i\mathbf{k}\cdot\mathbf{r}}, \tag{5.15}$$

with coefficients $C_{\mathbf{k}}$, we can arrive at the central equation:

$$(E^0_{\mathbf{k}-\mathbf{G}} - E_{\mathbf{k}}) C_{\mathbf{k}}(\mathbf{G}) + \sum_{\mathbf{G}} U_{\mathbf{G}'-\mathbf{G}} C_{\mathbf{k}}(\mathbf{G}') = 0. \tag{5.16}$$

For the six reciprocal lattice vectors and the central point, we must therefore solve:

$$\begin{bmatrix} \epsilon_k^0 - \epsilon_k & U_1 & U_2 & U_3 & U_4 & U_5 & U_6 \\ U_{-1} & \epsilon_{k-G_1}^0 - \epsilon_k & U_1 & U_2 & U_3 & U_4 & U_5 \\ U_{-2} & U_{-1} & \epsilon_{k-G_2}^0 - \epsilon_k & U_1 & U_2 & U_3 & U_4 \\ U_{-3} & U_{-2} & U_{-1} & \epsilon_{k-G_3}^0 - \epsilon_k & U_1 & U_2 & U_3 \\ U_{-4} & U_{-3} & U_{-2} & U_{-1} & \epsilon_{k-G_4}^0 - \epsilon_k & U_1 & U_2 \\ U_{-5} & U_{-4} & U_{-3} & U_{-2} & U_{-1} & \epsilon_{k-G_5}^0 - \epsilon_k & U_1 \\ U_{-6} & U_{-5} & U_{-4} & U_{-3} & U_{-2} & U_{-1} & \epsilon_{k-G_6}^0 - \epsilon_k \end{bmatrix} \times \begin{bmatrix} C_k(0) \\ C_k(G_1) \\ C_k(G_2) \\ C_k(G_3) \\ C_k(G_4) \\ C_k(G_5) \\ C_k(G_6) \end{bmatrix} = \mathbf{0}. \quad (5.17)$$

Here, $U_{G_\alpha} = \frac{U}{2}(1 + e^{i(\theta_{k-G_\alpha} - \theta_k)})$, for all G_α, which becomes $U_{G_\alpha} = U$ if a simple, non-chiral case is considered. This can be solved to give the eigenvectors, C_k, and eigenenergies, ϵ_k. The eigenvectors, when calculated for $U = 0$, reveal the bandnumber for each point in k-space. This is a far more efficient way to determine where the Brillouin zones are than geometrically constructing them, particularly when including next-nearest neighbours and beyond. This bandnumber is then used to construct the band structure of both the $U = 0$ and the $U \neq 0$ cases. The bandnumber indicates which eigenenergy to select for each point in k-space and thus reveals the overall, perturbed band structure. The potential strength, $U = 0.06$ eV, is estimated from numerical second-order perturbation theory [96]. When $U = 0$ eV, Eq. (5.17) becomes a simple diagonal matrix and the result reduces to the linear band structure.

5.4 Band Structure of Graphene on hBN

In Fig. 5.6(a), we plot a point in k-space with the surrounding six nearest-neighbours (marked by the hexagon), and also the 44 neighbours that we will use in a later calculation. The eigenvectors, C_k, in Eq. (5.17) with $U = 0$ eV, reveal the band index and location of the bands as seen in Fig.

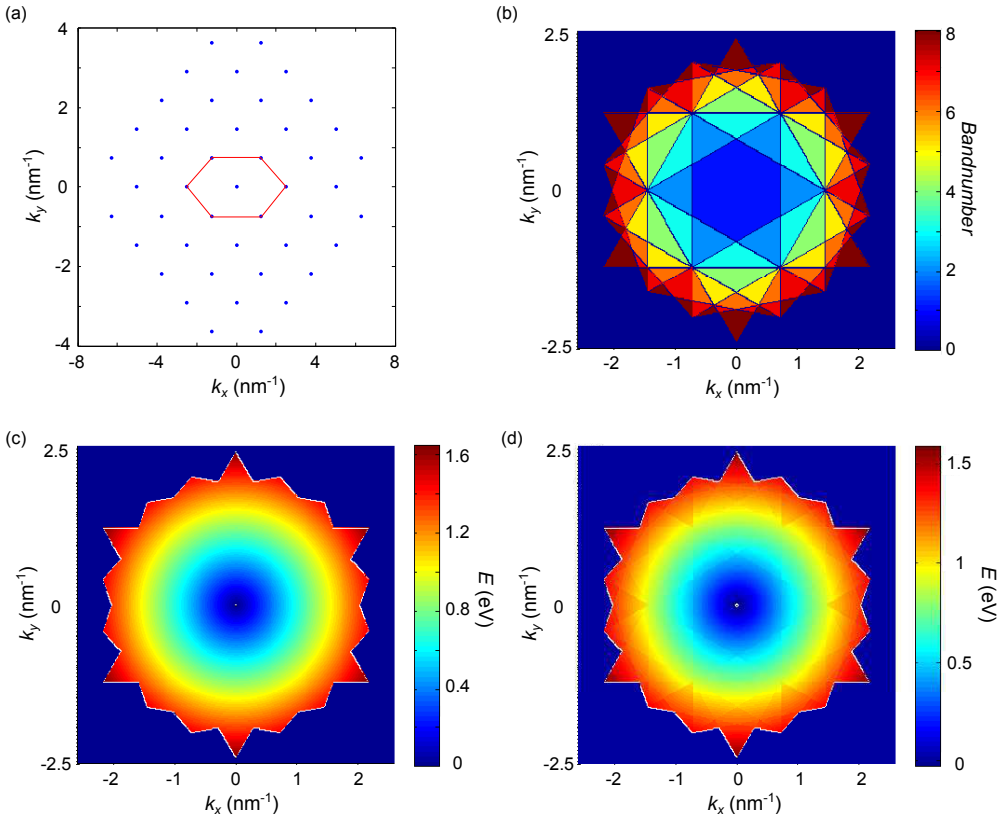

Figure 5.6: (a) A point in k-space surrounded by the six nearest neighbours (joined by the red hexagon) and other neighbours. (b) The first eight Brillouin Zones calculated via the eigenvalues of the central equation. (c) Calculated $E(k_x, k_y)$ in the first seven BZs for $U = 0$ eV and $\phi = 0°$. (d) Calculated $E(k_x, k_y)$ in the first seven BZs for $U = 0.06$ eV and $\phi = 0°$.

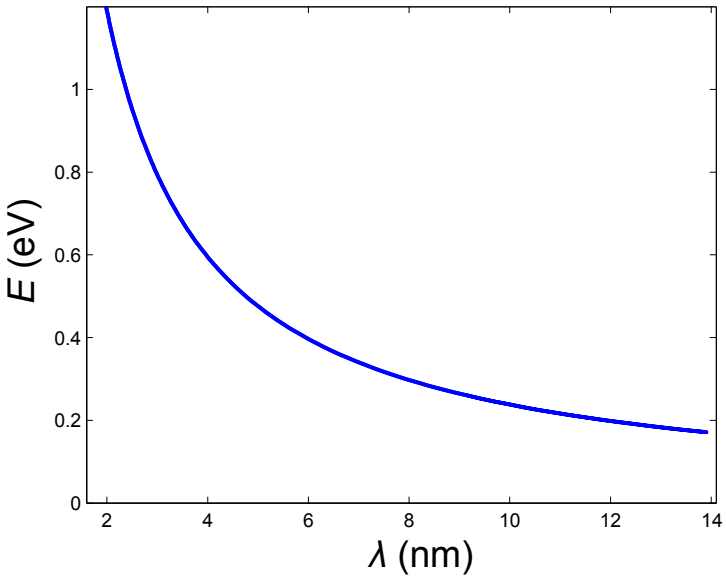

Figure 5.7: Energy, E, at which the secondary Dirac point occurs, relative to the Dirac point of ordinary graphene, calculated as a function of wavelength, λ, of the moiré pattern. The smaller ϕ_M, and thus larger λ_M lead to the superlattice Dirac point occurring at lower energies.

5.6(b). The eigenvalues for these bands are given by the corresponding eigenenergies, as shown in Fig. 5.6(c), which reveals that the band structure is linear in E. In comparison, when a moiré potential of $U = 0.06$ eV is applied, via Eq. (5.17), the $E(k_x, k_y)$ plot (Fig. 5.6(d)) is no longer linear. Discontinuities in E arise at the reciprocal lattice vector points, where the bandnumber changes. This is a fascinating feature due to the potential felt by the electrons in the hBN-graphene superlattice. An even larger surface of $E(k_x, k_y)$ can be calculated by expanding the matrix in Eq. (5.17) to include many more neighbours. Fig. 5.9(a) shows the bandnumbers calculated for a larger region of k-space.

A corresponding plot of $E(k_x, k_y)$, Fig. 5.9(b), reveals the effect of the moiré potential on the band structure over this larger k-space region. Here, $\theta = 0°$, $\phi_M = 0°$, and chirality effects are turned off for simplicity, i.e. $U = U_G = 0.06$ eV and $g = 1$. We note that, at low E, the band structure remains linear. As E approaches $E = \hbar v_F G/2$, the $E(k_x, k_y)$ looses linearity and the electron and hole bands come together again to form a supplementary Dirac point. In Fig. 5.9(c), we see six additional Dirac points arising at an energy of $-\hbar v_F|\mathbf{G}|/2$, and would also get six more at $E = +\hbar v_F|\mathbf{G}|/2$. These points occur at the edge of the first Brillouin Zone, and are where the electron and hole bands meet. We note that, at even higher magnitudes of

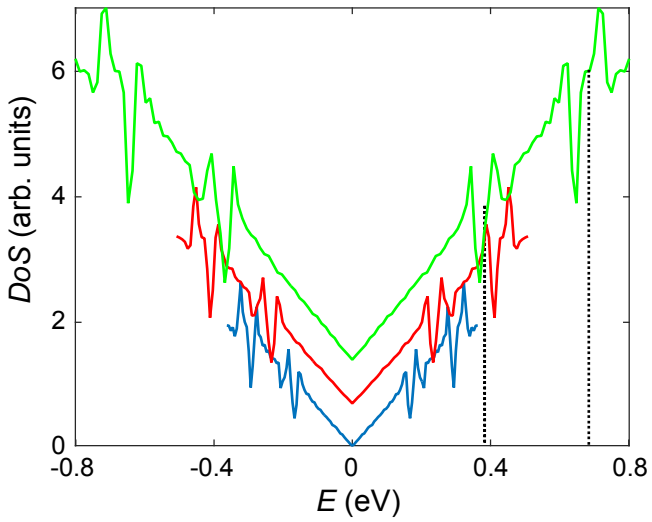

Figure 5.8: The density of states, DoS, calculated for three different rotation angles between the hBN and the graphene; $\phi_M = 0°$ (blue curve), $\phi_M = 1°$ (red curve), and $\phi_M = 2°$ (green curve). The curves are vertically offset for clarity and go up to energies just after the second superlattice Dirac points. The dashed lines mark the energies at which the first and second superlattice Dirac points occur in the conduction band when $\phi_M = 2°$. For this case, these energies are at $E = \hbar v_F|\mathbf{G}|/2 = 0.35$ eV and $E = \hbar v_F|\mathbf{G}| = 0.7$ eV

energy, the phenomenon reoccurs, and we see additional superlattice Dirac points.

The density of states (DoS) can be calculated by taking energy contours of the dispersion relation, which reveals the number of states at that energy. Fig. 5.8 shows the decrease in density of states as the electron and hole bands cross over each other, resulting in the additional Dirac point, where the DoS decreases.

The position of the secondary Dirac point depends on the rotation angle between the hBN and the graphene layers, ϕ_M, which, in turn, affects the "superlattice" wavelength, λ. In Fig. 5.7, we see that increasing the superlattice wavelength, i.e. aligning the hBN and graphene lattices, causes the secondary Dirac point to occur at lower energies. Experimental results [96] have confirmed this relationship between the energy and the reciprocal lattice vector, i.e. for the first superlattice Dirac point:

$$E = \frac{\hbar v_F|\mathbf{G}|}{2} = \frac{2\pi\hbar v_F}{3\lambda}. \tag{5.18}$$

In Fig. 5.8, $DoS(E)$ is plotted for $\phi_M = 0°, 1°$ and $2°$, up to energies just

past the second superlattice Dirac point in each case. We note the dip in the DoS is greater for higher ϕ_M values and would thus have a larger effect on the tunnelling. However, the increase in ϕ_M also increases the energy at which the superlattice Dirac points occur. This is expected, as $|\mathbf{G}| \approx 2\pi/\mathbf{g}$ will increase with ϕ_M, and thus the number of energetic states in the first Brillouin zone will also increase. By increasing ϕ_M from 0° to 2°, the energy at which the first superlattice Dirac point occurs more than doubles, i.e. the green curve in Fig. 5.8 has more than twice the energy span as the blue. As we want to avoid entering the over-the-barrier conduction regime, which arises at E approaches the energy of the barrier, we will investigate lower ϕ_M values. In [95, 96], it is noted that the dip in the density of states is much more pronounced in the valence band, compared to the conduction band, due to the electron-hole symmetry breaking produced by the superlattice perturbation. However, as we also want to investigate chirality, which is expected to lead to further asymmetry, we keep the DoS symmetric about zero. Fig. 5.9(a) shows the additional Brillouin zone locations calculated from Eq. (5.17), which allows the dispersion relation for the energies in Fig. 5.9(b) to be calculated. Here, we see six additional Dirac points appearing in the valence band due to the moiré potential.

5.5 Modelling Electrostatics with Moiré Effects

The electrostatics for a GRTD on a hBN substrate brought into relative alignment with the lattice of the bottom graphene electrode can now be considered. The perturbed DoS and band structure now replace the linear alternatives, for the bottom graphene electrode only, in the calculation of I_b. The hBN barrier is assumed to be misaligned such that no moiré pattern effects occur due to the barrier layers, and the top graphene layer is assumed to maintain the linear dispersion, as it is much further away from the substrate.

The chirality term for the system is calculated from the wavefunction overlap between the perturbed wavefunction from the bottom layer, and the

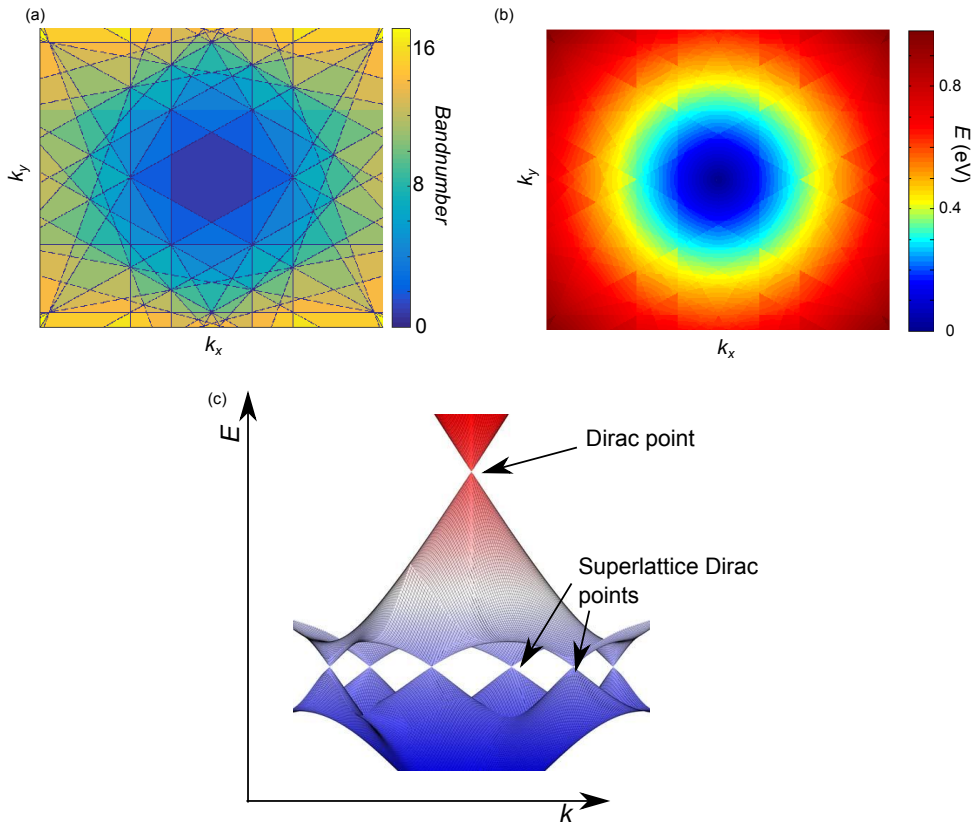

Figure 5.9: (a) Further Brillouin zones calculated from Eq. (5.17). (b) $E(k_x, k_y)$ calculated with $U = 0.06$ eV for a larger k-space region. This potential leads to regions of non-linear dispersion. Scale, right, modified to enhance energies around the superlattice Dirac points. (c) Figure adapted from [96]. The band structure of graphene under a weak superlattice potential, showing the original Dirac point at $E = 0$ eV, and the emerging superlattice Dirac points.

unperturbed wavefunction in the top layer:

$$\int dxdy\langle\psi_B|\psi_T\rangle = \frac{1}{2\Omega}\int dxdy\langle e^{i\mathbf{k}_T\cdot\mathbf{r}}(1+s_Te^{-i\theta_{k_T}})|\sum_k c(k)e^{-i\mathbf{k}_B\cdot\mathbf{r}}(1+se^{i\theta_k})\rangle, \tag{5.19}$$

which gives:

$$\begin{aligned} g &= c(k)\delta(k_T,k_B)[1+s_Be^{i\theta_{k_B}}+s_Te^{i\theta_{k_T}}+s_Bs_Te^{i(\theta_{k_B}-\theta_{k_T}}] \\ &+\sum_G c(k-G_\alpha)\delta(k_T,k_B-G_\alpha)[1+s_Be^{i\theta_{k_B-G_\alpha}}+s_Te^{i\theta_{k_T}}+s_Bs_Te^{i(\theta_{k_B-G_\alpha}-\theta_{k_T})}], \end{aligned} \tag{5.20}$$

when integrated over all space. Many neighbours can be included in this model by expanding Eq. (5.17), which allows higher eigenenergies to be calculated. In our simulation, we take 44 of the neighbours to a central point, which covers all the energies reached in the dispersion relation for the tunnelling events that actually contribute to the current.

5.6 Analysis of Moiré Effects

To understand the effect of a moiré potential, and the resulting change in the DoS, on the tunnelling, the conductance, $dI_b(\mu_B,\mu_T)/dV_b$, can be calculated. Here, $dI_b/dV_b = (I(1\text{ meV}) - I(\text{-}1\text{ meV}))/2$ meV is the difference in conductance when a small bias-voltage is applied in the forward and reverse directions. By scanning through all combinations of μ_B and μ_T, the tunnelling for a range of different Dirac cone alignments and fillings can be probed. The currents $I(\mu_B,\mu_T)$ at $\pm$ 1 meV are not individually symmetric over (μ_B,μ_T), but, when averaged, become symmetric for the non-chiral case. We will later consider the inclusion of chirality, but for simplicity, we first understand the system without it.

We begin the investigation with the aligned device, i.e. $\theta = 0^\circ$ and $\phi_M = 0^\circ$. In Fig. 5.10(a), with $U = 0$ eV, we see that dI_b/dV_b is high when $|\mu_B| \approx |\mu_T|$. The magnitude of dI_b/dV_b increases with increasing $|\mu_{B,T}|$. When $|\mu_B|$ and $|\mu_T|$ are not alike, the tunnel current, and thus dI_b/dV_b, goes to 0. The same occurs in Fig. 5.10(b) when the moiré potential is turned on, $U = 0.06$ eV, however, lines of low current occur. To understand these results, it is useful to plot DoS(E) in the two cones along with the relative

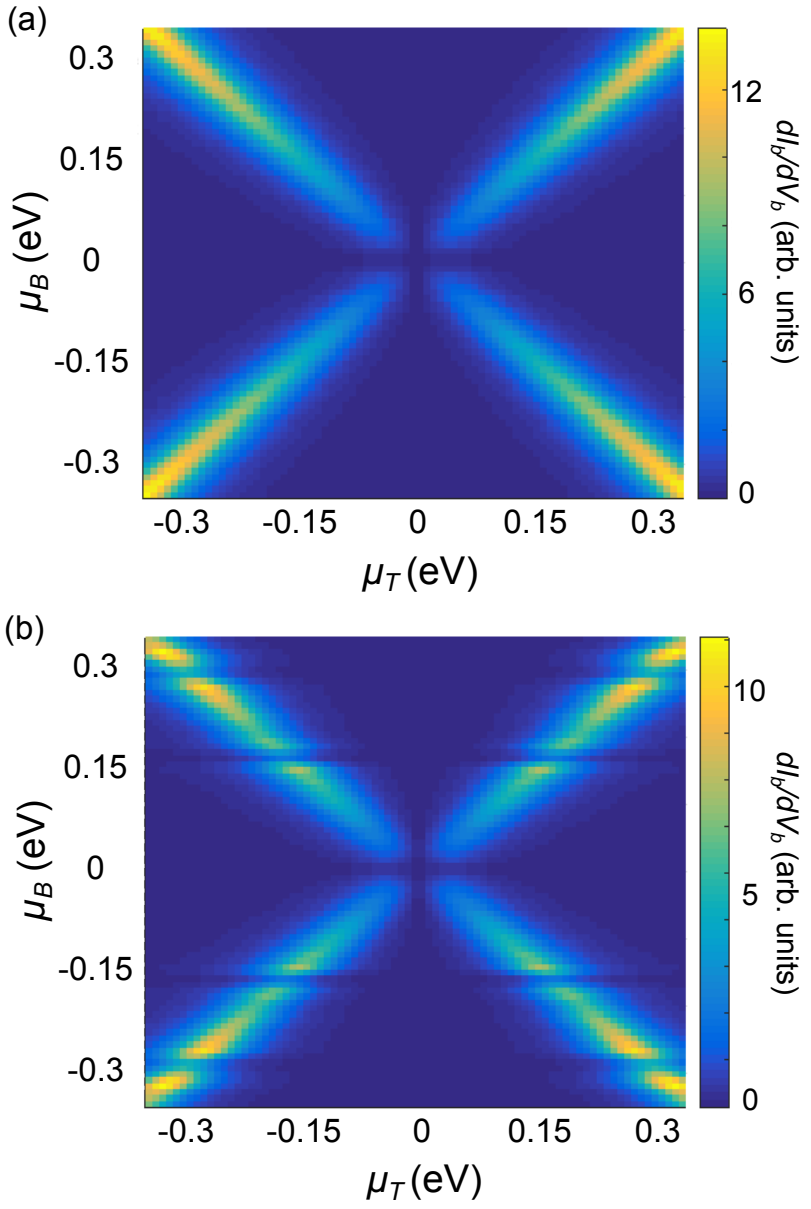

Figure 5.10: Calculated $dI_b(\mu_B, \mu_T)/dV_b$ colour maps (scales, right) for (a) $U = 0$ eV and (b) $U = 0.06$ eV, where $\theta = 0°$ and $\phi_M = 0°$. The perturbed density of states leads to lines of low conductance in (b).

alignment and Fermi levels, for a small bias voltage, $V_b = 1$ meV. It is also enlightening to plot the $E(k_x, k_y)$ contours in both cones at $E = \mu_B$. For the $U = 0$ eV case, these are shown in Figs. 5.11(a-h). In Fig. 5.11(a,b), $\mu_B = \mu_T = 0$ eV. If we return to the equation for the voltage dropped across the device,

$$eV_b = \mu_B - \mu_T - eF_b d, \tag{5.21}$$

we can see that, for the undoped case, the voltage drop across the barrier $eF_b d = -1$ meV. The neutrality point and Fermi level of the bottom electrode will be at $E = 0$ eV, whilst the Fermi level in the top electrode, relative to the Dirac point of the bottom electrode, will be $\mu_T' = \mu_T + eF_b d = -1$ meV. Since this is a very small drop compared to energies reached with non-zero levels of doping, in Fig. 5.11(a), the Dirac cones appear aligned and filled up to the neutrality points only. The $k_{B,T}(k_x, k_y)$ plotted for this doping reveals $k_B = 0$ nm^{-1} and k_T is very small compared to the doped cases in Fig. 5.11(d,f,h). As no states are available to tunnel from the bottom cone, and there are very few empty states available to tunnel into in the top cone, the current here is 0. This is the central point in Fig. 5.10(a).

We can also analyse the peak in current in Fig. 5.10(a), for example, looking at the top right corner where $\mu_B = \mu_T = 0.35$ eV. The alignment of the Dirac cones in this case is shown in Fig. 5.11(c), where we see both cones are filled with conduction electrons up to their respective Fermi levels. As the Fermi levels are high, the DoS is high at this point, thus, many electron states are available for tunnelling to a large number of empty electron states in the top electrode, due to the small V_b which energetically shifts the cones by -1 meV. Fig. 5.11(d) shows the k states and we note the change in momentum required for tunnelling is low. Consequently, we expect a high current, and, thus, conductance.

Away from the symmetric values of μ_B and μ_T, in Fig. 5.10(a), we note the current is low. For example, at $\mu_B = 0.35$ eV and $\mu_T = 0$ eV, we plot the alignment in Fig. 5.11(e). Here, the Fermi level in the bottom electrode is high, and thus shows a large number of states in Fig. 5.11(f). However, the energetic states in the top electrode are far from energetic alignment, and no empty states are available to accept tunnelling electrons.

It is also interesting to observe a point just off-centre from the diagonal current peak in Fig. 5.10(a), such as $\mu_B = 0.25$ eV and $\mu_T = 0.32$ eV, the

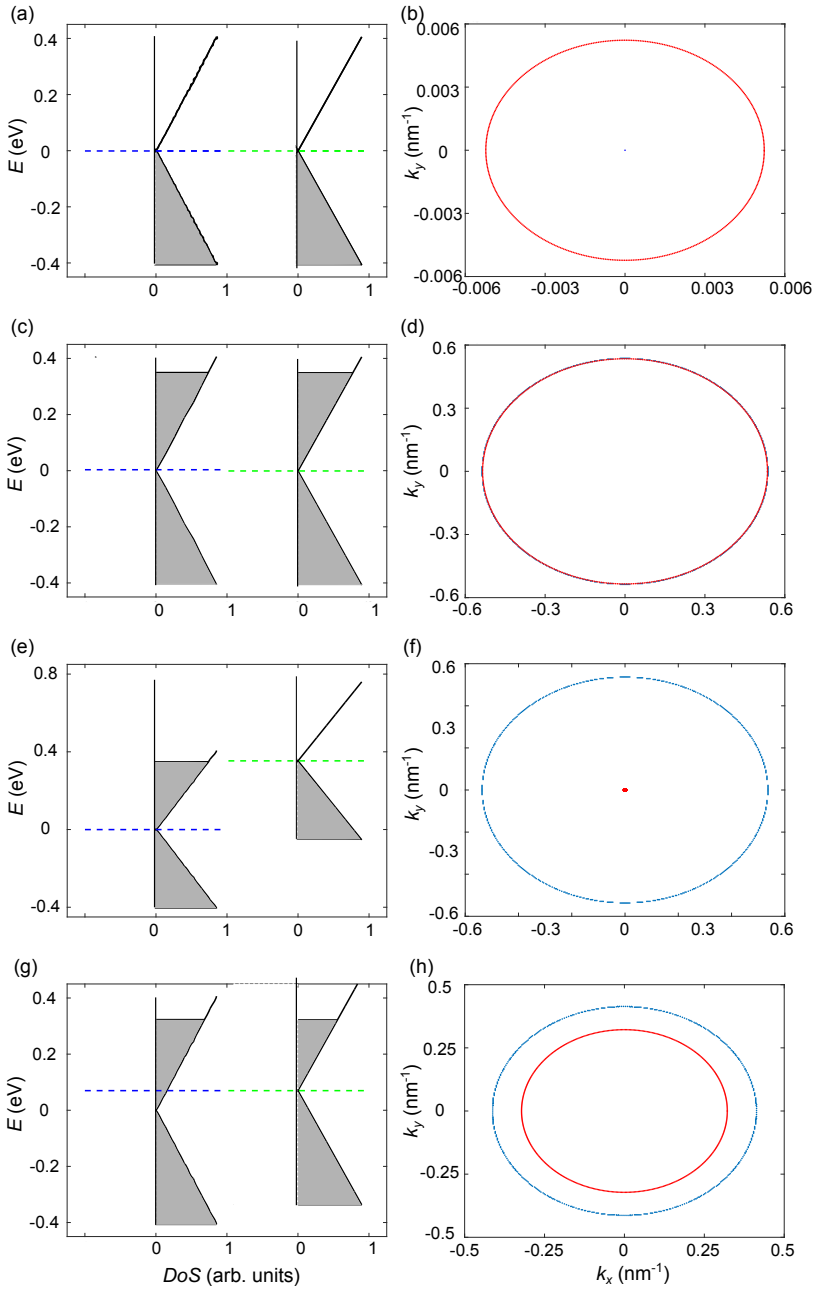

Figure 5.11: Electronic states in the graphene electrodes calculated for $U = 0$ eV, $\theta = 0°$ and $\phi_M = 0°$. Panels (a,c,e,g) show $DoS(E)$ in the bottom (left) and top (right) graphene electrodes for four sets of doping, explained in the text, with $V_b = 1$ meV. The energy states are filled up (coloured grey) to the Fermi level in each electrode, and the neutrality points in the bottom and top electrodes are plotted by the dashed blue and green lines, respectively. Panels (b,d,f,h) show energy contours in k-space at $E = \mu_B$ in the bottom electrode (blue) and top electrode (red).

results of which are seen in Fig. 5.11(g-h). Here, we see that although both electrodes are positively-doped like in Fig. 5.11(c-d), the Dirac cones are more energetically misaligned, and thus the current is lower than on the diagonals of Fig. 5.10(a), as a larger change in momentum is required for tunnelling transitions.

Now that the results of Fig. 5.10(a) are fully understood, we can analyse the system with the moiré potential on, with $U = 0.06$ eV. In Fig. 5.10(b), regions of low dI_b/dV_b appear at certain energetic alignments. The DoS(E) and $k_{B,T}(k_x, k_y)$ contours in Fig. 5.12(a-b) reveal where, in the $U = 0$ eV case, we would expect the current to be high, e.g. when $\mu_B = \mu_T = 0.22$ eV. In the $U = 0.06$ eV case, the DoS is lower at this point. This is because the energetic alignment has reached the first superlattice Dirac point, as seen by the Fermi level in Fig. 5.12(a). Consequently, although there is the same number of states available to tunnel into in the top graphene electrode, there is a reduced number available to tunnel from the bottom graphene electrode, compared to in the linear dispersion, and so the current is reduced. Fig. 5.12(b) shows the location of states in k-space in each electrode at $E = \mu_B$. At higher doping levels ($\mu_B = \mu_T = 0.28$ eV), a maximum in current is achieved, which corresponds to the alignments and energy contours plotted in Fig. 5.12(c). Here, the tunnel current benefits from an increase in the number of states available for tunnelling, as seen in Fig. 5.12(d), just before the second supplementary Dirac point is reached. Increasing the doping further ($\mu_B = \mu_T = 0.30$ eV) brings the chemical potentials into alignment with this superlattice Dirac point, and thus reduces the current.

Note, the lines of low differential conductance in Fig. 5.10(b) occur only horizontally. This is due to the fact that only the bottom electrode has a perturbed band structure in the arrangement considered here.

The conductivity, $dI_b(\mu_B, \mu_T)/dV_b$ can also be plotted versus μ_B and μ_T for the $\theta = 0.9°$ case, with $\phi_M = 0°$, as shown in Fig. 5.13(a) for $U = 0$ and in (b) for $U = 0.06$ eV. We note that compared to the $\theta = 0°$, the overall conductance is lower, and there is a larger region of zero conductance around $\mu_B = \mu_T = 0$. This is due to the decrease in overlap of states in k-space, as seen in Figs. 5.14(b,d,f). As a result, thus the Fermi levels need to reach a higher magnitude before a significant tunnel current arises. In the regions where $|\mu_B| \neq |\mu_T|$, the device with $\theta = 0°$ still has higher conductance, but the difference from the $|\mu_B| = |\mu_T|$ case is greater, thus the scale of the colour maps gives the appearance that the conductance flows

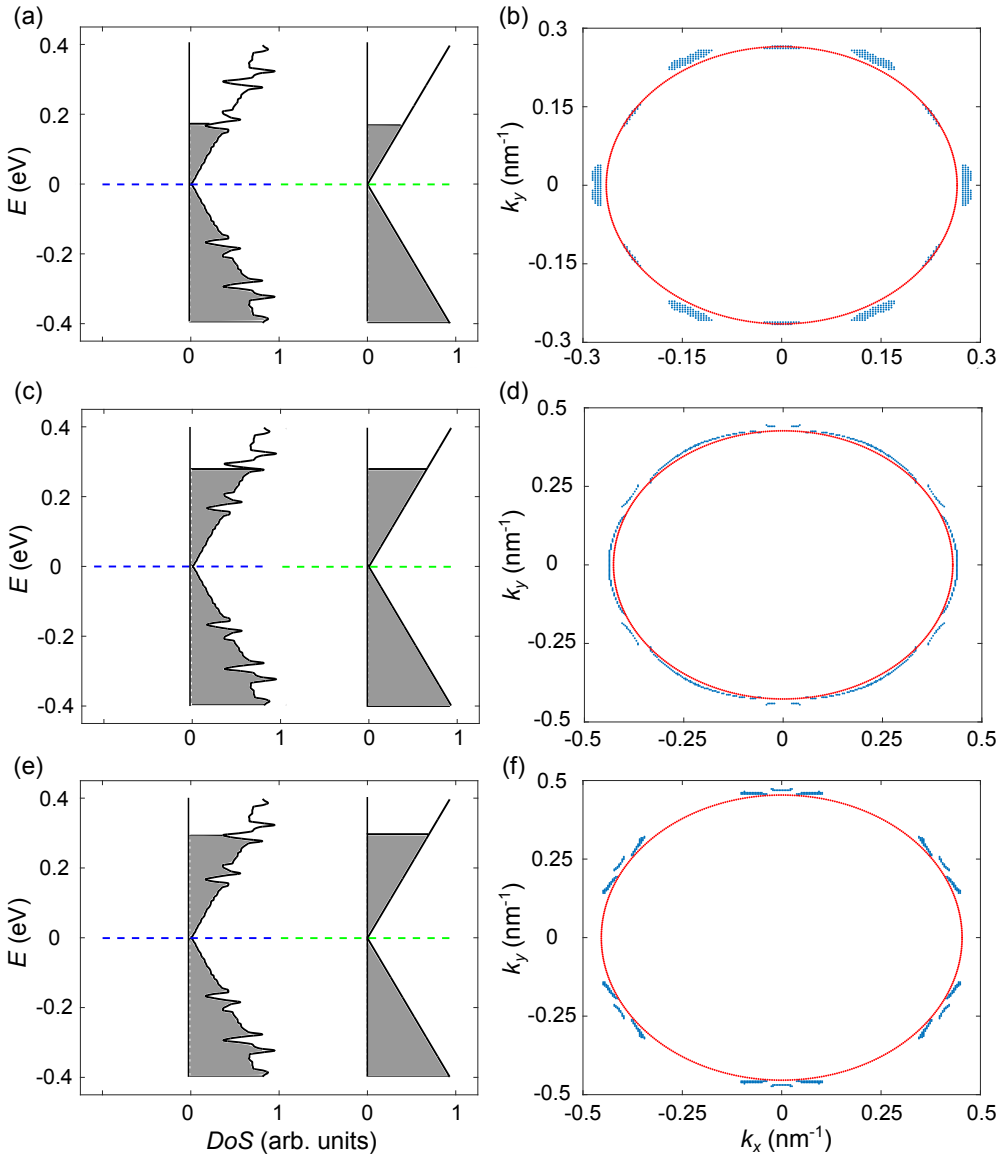

Figure 5.12: Electronic states in the graphene electrodes calculated for $U = 0.06$ eV, $\theta = 0°$ and $\phi_M = 0°$. Panels (a,c,e) show $DoS(E)$ in the bottom (left) and top (right) graphene electrodes for three sets of doping, explained in the text, with $V_b = 1$ meV. The energy states are filled up (coloured grey) to the Fermi level in each electrode, and the neutrality points in the bottom and top electrodes are plotted by the dashed blue and green lines, respectively. Panels (b,d,f) show energy contours in k-space at $E = \mu_B$ in the bottom electrode (blue) and top electrode (red).

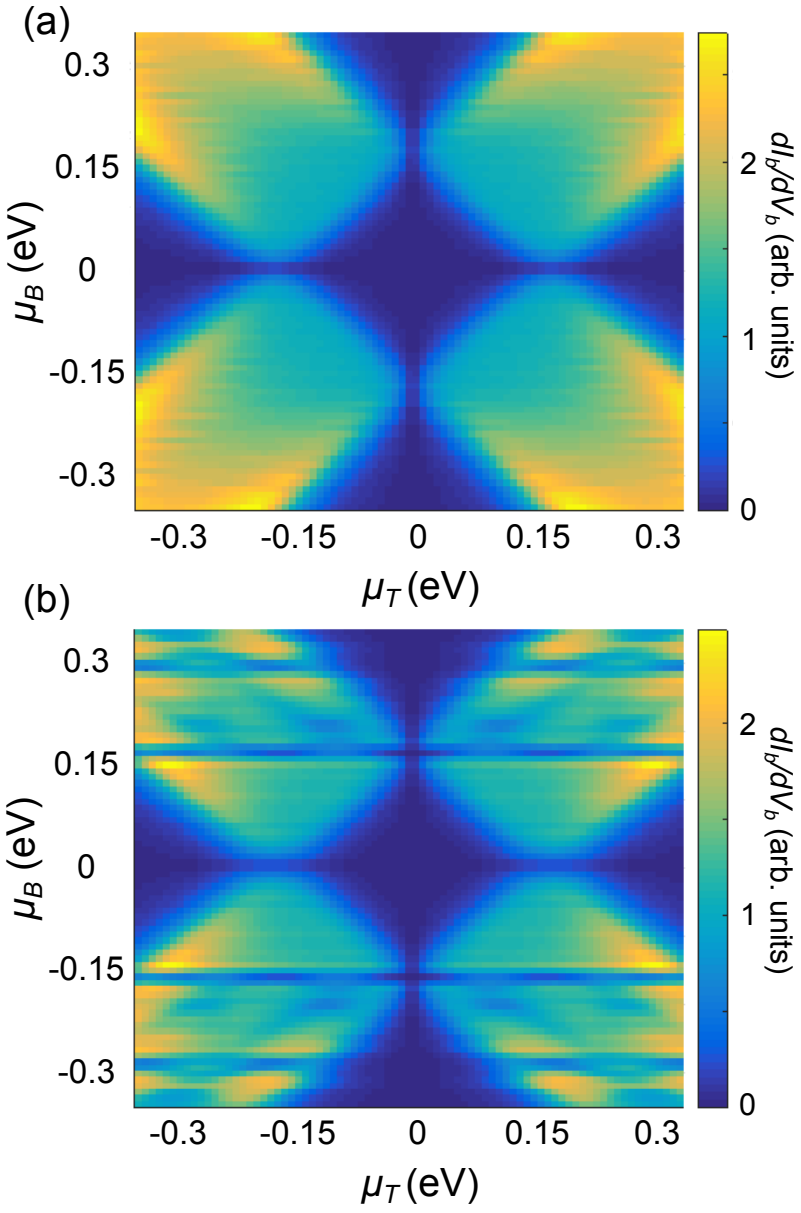

Figure 5.13: Calculated $dI_b(\mu_B, \mu_T)/dV_b$ for (a) $U = 0$ eV and (b) $U = 0.06$ eV, where $\theta = 0.9°$ and $\phi_M = 0°$. The perturbed density of states leads to lines of low conductance in (b).

for a larger range of μ_B, μ_T, when $\theta = 0.9°$, which is actually not true. The moiré potential again leads to lines of low conductance corresponding to the Fermi levels approaching the superlattice Dirac points.

In Figs. 5.14(a-f), $U = 0.06$ eV, $\theta = 0.9°$ and $\phi_M = 2°$. Here, we can see all of the effects considered above. The moiré potential gives the non-linear dispersion relation in the bottom cone, ϕ_M shifts the superlattice Dirac points in energy, and θ shifts the energy states in k-space. Figs. 5.14(a-b) are plotted for $\mu_B = 0.35$ eV and $\mu_T = 0.22$ eV, Figs. 5.14(c-d) are plotted for $\mu_B = \mu_T = 0.29$ eV, and Figs. 5.14(c-d) are plotted for $\mu_B = 0.32$ eV and $\mu_T = 0.26$ eV. The corresponding conductance colour maps are shown in Fig. 5.15(b), with the $\theta = 0°$ case in Fig. 5.15(a).

5.7 Chirality Effects

The two-component form of the electron wavefunction in graphene is expected to affect the tunnelling current [103, 104]. The chirality leads to two terms in the form of the tunnel current. Firstly, the overlap of the basis wavefunctions in the graphene electrodes gives rise, as shown in Eq. (5.20) to the factor g. This describes the interference of the A and B sublattices. Secondly, in Eq. (5.17), the term of $U_G = \frac{U}{2}(1 + e^{i(\theta_{k-G} - \theta_k)})$ lead to an asymmetry in the perturbed $E(k_x, k_y)$ surface [95]. For simplicity, we first investigate the effect of including the g term, and quantify its influence on the conductance.

Fig. 5.16 shows $dI_b/dV_b(\mu_B, \mu_T)$ surfaces calculated for $U = 0$ eV with $\phi_M = 0°$ and (a) $\theta = 0°$ and (b)$\theta = 0.9°$. We see regions of high current in the $\mathrm{sgn}(\mu_B) = \mathrm{sgn}(\mu_T)$ regions (lower left and upper right quadrants, Fig. 5.16), where tunnelling is between like bands, i.e. valence band to valence band, and conduction band to conduction band. Here, the tunnelling is enhanced as the electron conserves chirality by tunnelling to an equivalent pseudospin branch. By contrast, when $\mathrm{sgn}(\mu_B) = -\mathrm{sgn}(\mu_T)$, the current is suppressed, due to the change in chirality. In comparison, without g included, we return to the results of 5.10(a) and 5.12(a), respectively, where all four quadrants have equivalent tunnelling.

Similarly, when $U = 0.06$ eV, as in Fig. 5.17 for (a) $\theta = 0°$ and (b) $\theta = 0.9°$, the tunnelling between like bands is enhanced, whilst the tunnelling between unlike bands is suppressed. The lines of low conductance due to the perturbed DoS in the bottom graphene electrode remain the same as in the respective $U = U_G$ cases in Fig. 5.10(b) and Fig. 5.13(b).

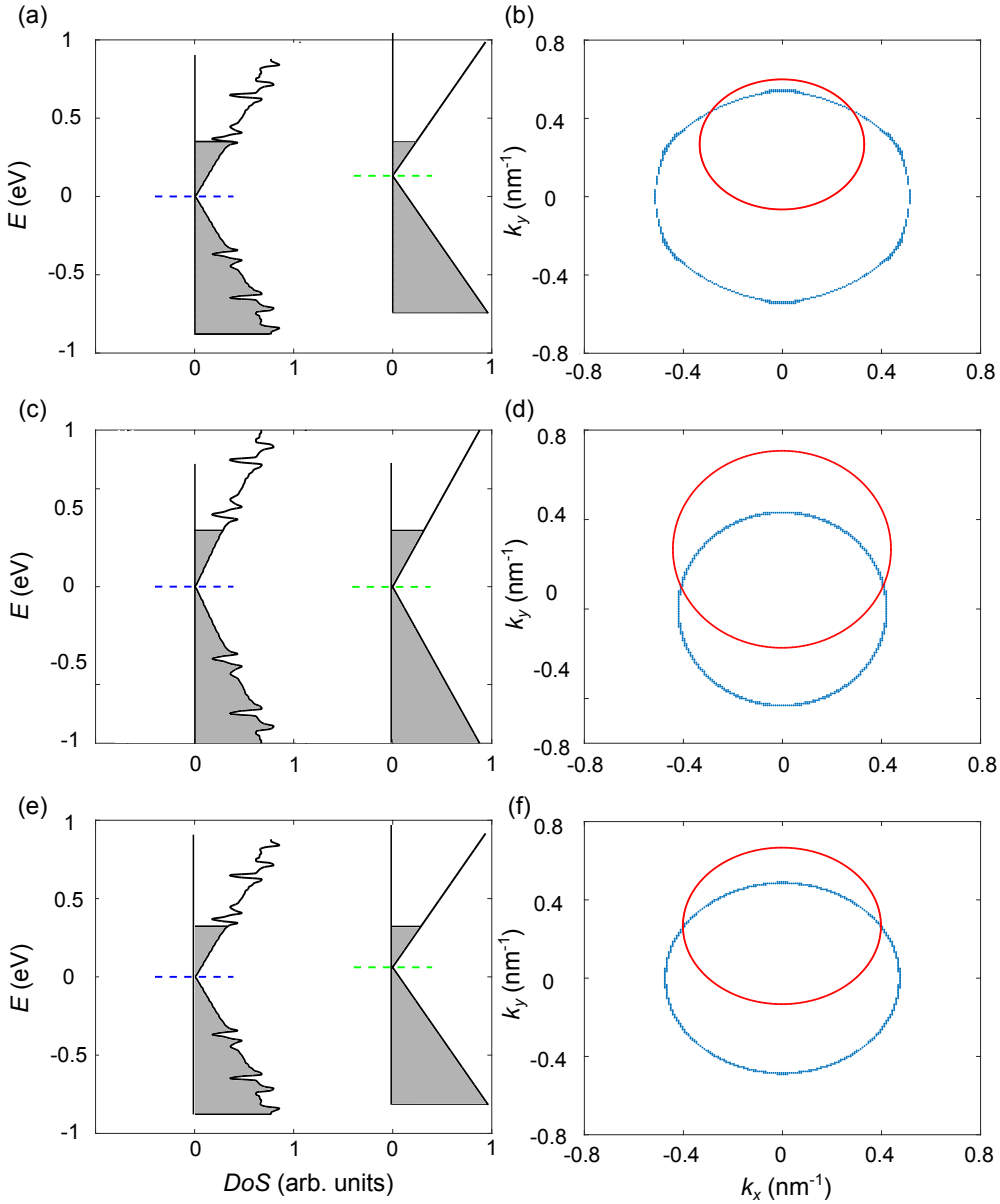

Figure 5.14: Electronic states in the graphene electrodes calculated for $U = 0.06$ eV, $\theta = 0.9°$ and $\phi_M = 2°$. Panels (a,c,e) show $DoS(E)$ in the bottom (left) and top (right) graphene electrodes for three sets of doping, explained in the text, with $V_b = 1$ meV. The energy states are filled up (coloured grey) to the Fermi level in each electrode, and the neutrality points in the bottom and top electrodes are plotted by the dashed blue and green lines, respectively. Panels (b,d,f) show energy contours in k-space at $E = \mu_B$ in the bottom electrode (blue) and top electrode (red). The energy states are shifted in k due to the the misalignment, θ.

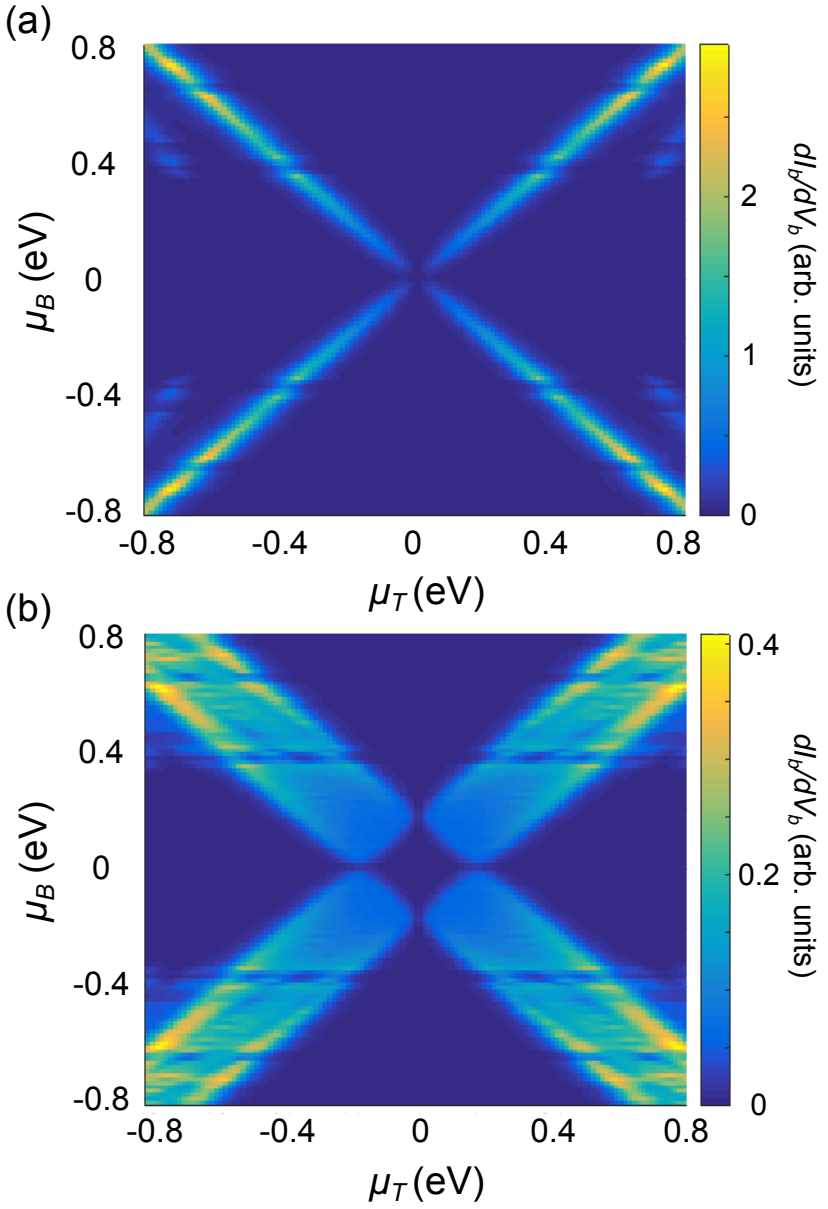

Figure 5.15: Colour maps of $dI_b(\mu_B, \mu_T)/dV_b$ (scale, right) calculated versus μ_B and μ_T for (a) $\theta = 0°$ and (b) $\theta = 0.9°$, where $U = 0.06$ eV and $\phi_M = 2°$. We note, with $\phi_M = 2°$, the features exist at higher energies, and thus the $\mu_{B,T}$ axes are larger than those for $\phi_M = 0°$ colour maps.

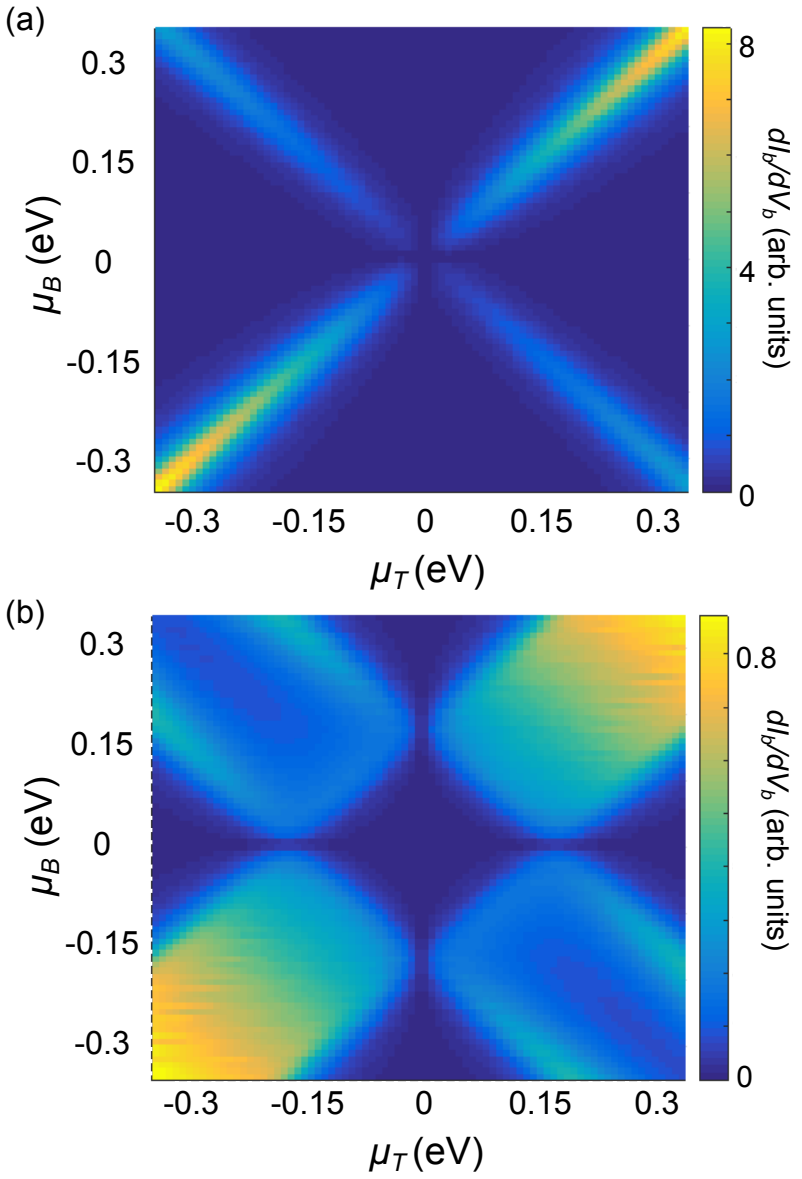

Figure 5.16: Colour maps of $dI_b(\mu_B, \mu_T)/dV_b$ (scale, right) versus μ_B and μ_T calculated for (a) $\theta = 0°$ and (b) $\theta = 0.9°$, where $U = 0$ eV and $\phi_M = 0°$ and the g term in Eq. (5.20) is turned on. Chirality enhances the tunnelling between alike bands, and suppresses tunnelling between unlike bands.

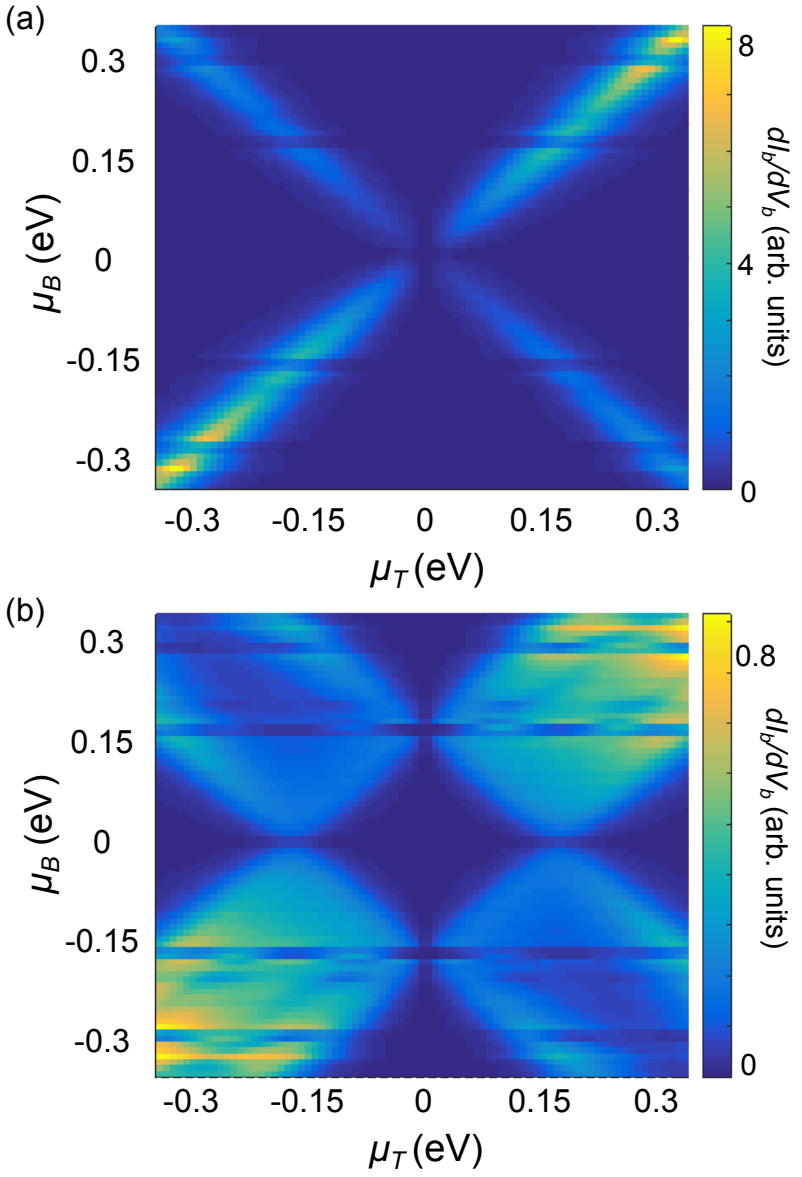

Figure 5.17: Colour maps of $dI_b(\mu_B, \mu_T)/dV_b$ (scale, right) versus μ_B and μ_T calculated for (a) $\theta = 0°$ and (b) $\theta = 0.9°$, where $U = 0.06$ eV and $\phi_M = 0°$ and the g term in Eq. (5.20) is turned on. We note the enhancement and suppression of like band and unlike band tunnelling. The lines of low conductance remain.

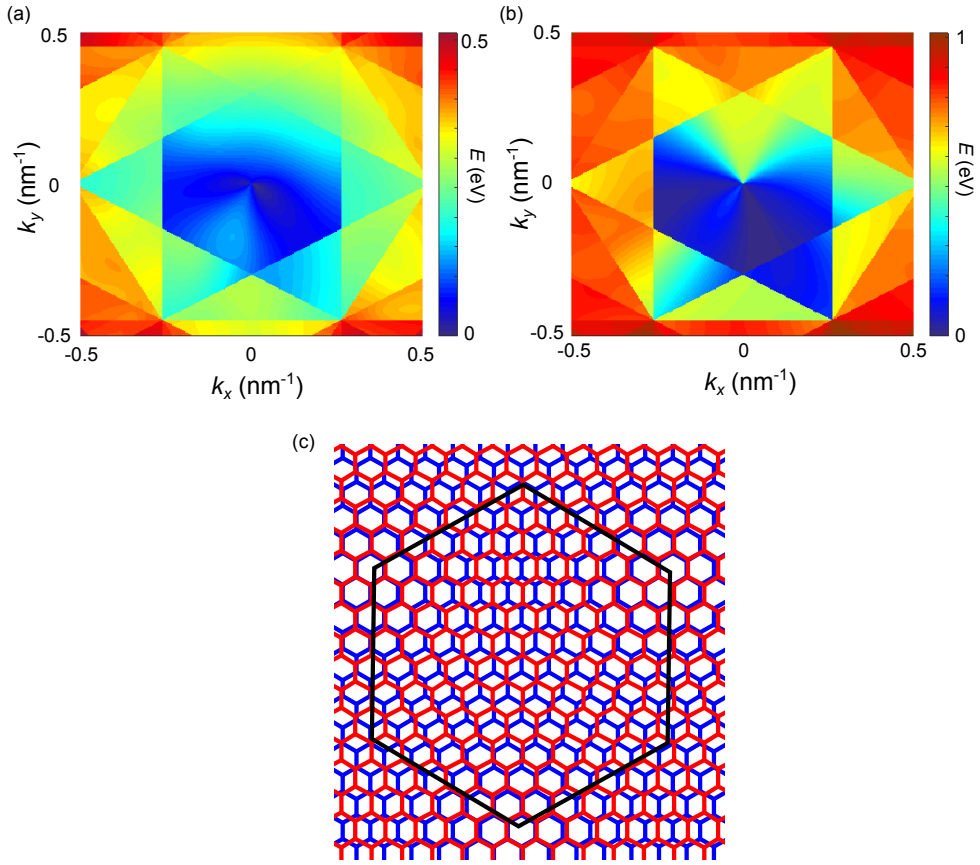

Figure 5.18: $E(k_x, k_y)$ colour maps calculated with chirality effects included in U for (a) $U_G = 0.06$ eV, and (b) $U_G = 0.12$ eV, for $\phi_M = 0°$. Asymmetry arises due to the lattice mismatch between the hBN and graphene hexagonal crystal lattices, as seen in (c). Here, individual hexagons within the moiré plaquette will experience a different superlattice potential.

Including the two-component form of the electron wavefunction in the Eq. (5.17) leads to asymmetric $E(k_x, k_y)$ surfaces, as seen in Fig. 5.18. Here, the asymmetry becomes more pronounced when the strength of the potential, U_G, is increased, as seen by comparing Fig. 5.18(a), where $U = 0.06$ eV, and Fig. 5.18(b), where $U = 0.12$ eV. The asymmetry can be understood by considering the moiré plaquette, as seen in Fig. 5.18(c). Even when $\phi_M = 0°$, due to the lattice mismatch between the hBN and graphene layers, the majority of lattice unit cells will experience an asymmetric potential, as the distance to their nearest neighbour varies in all six directions of the lattice vectors. This behaviour will vary locally, and with the overall strength of the potential, as well as with ϕ_M. The analysis is therefore complicated to perform, and made even more complex by the large parameter space from the device. Here, we take a brief look at the effect of including chirality into U, for $U_G = 0.06$ eV, $\phi_M = 0°$ and $\theta = 0°$ and $\theta = 0.9°$, with the wavefunction overlap chirality, g, included.

The conductance colour maps shown in Fig. 5.19, now also exhibit asymmetric behaviour in the valence-valence band quadrant (bottom left), and the conduction-conduction band quadrant (top right). In this specific simulation, we see that the conduction band to conduction band current is enhanced, whilst the valence band to valence band current is suppressed. This is in addition to the chirality effect from g which would enhance both of these regions. The regions that are affected and the magnitude of the effect may completely change and be very sensitive to location or misalignment angles. Further work could help quantify the effects arising from this additional chirality term by analysing how they influence the $E(k_x, k_y)$ surfaces, by analysing specific points to look at the alignments, and by looking at the evolution of features as U, θ and ϕ_M are applied.

5.8 $I_b(V_b)$ Characteristics with Moiré Effects

The modified $I_b(V_b)$ characteristics can now be explored to understand the effects of the moiré patterns on the shapes of the curves, the position of the current peak, and the magnitude of the current. These, in turn, may affect the power and frequency output. Initial simulations calculated $I_b(V_b)$ for $\theta = 0°$ and $\theta = 0.9°$ for an undoped device without consideration of chirality, and with $\phi_M = 0°$. For these cases, the effect on the $I_b(V_b)$ curves was negligible. This is because although there is a measurable effect in

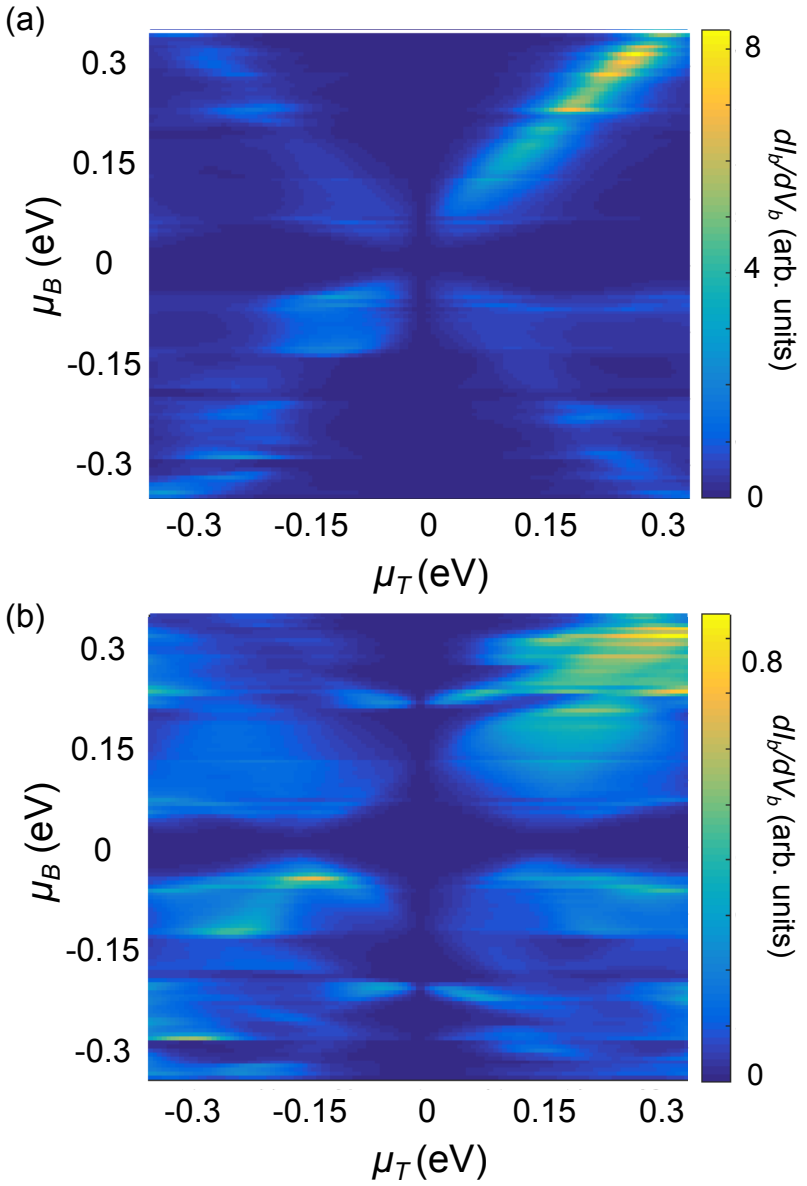

Figure 5.19: Calculated $dI_b(\mu_B, \mu_T)/dV_b$ for (a) $\theta = 0°$ and (b) $\theta = 0.9°$, where $U_G = 0.06$ eV and $\phi_M = 0°$ and the g term in Eq. (5.20) is turned on.

$dI_b(\mu_B, \mu_T)/dV_b$ as investigated in Section. 5.6, when integrating over a range of energies, as in Eq. (2.2), the tunnelling will be dominated by transport between states not at the superlattice Dirac points. It would be possible, in future work, to dope the electrodes to control the energetic region of tunnelling, and thus enhance the contribution of tunnelling events at the superlattice Dirac points.

In future work, it would be interesting to include novel $I_b(V_b)$ characteristics into the dynamic model to analyse the effect of any additional features, which may result in new frequency components in the current-time oscillations. It would also be interesting to analyse tunnelling between two perturbed Dirac cones, which are either perturbed in the same way, or by a different potential, determined by the alignments of the hBN barrier layers and the hBN substrate, and to also include the effects of chirality.

Chapter 6

Conclusion

Graphene offers novel properties for high-frequency electronics, which, combined with the ability to stack layers of 2D materials makes vertical van der Waals heterostructures very attractive from this perspective. The performance of GRTDs as the active element in RLC oscillators has been investigated, and it was shown that high GHz (∼100 GHz) and, possibly, THz oscillations seem achievable in appropriately-designed devices. Control of the misalignment angle, electrostatic environment and barrier thickness/composition, which have a dramatic effect on the ac collective electron dynamics, can be used to fine-tune the device characteristics. Advances in production techniques, such as molecular beam expitaxy, will allow more control over the multi-layer van der Waals heterostructures than the existing layer-by-layer stacking methods. Aligning the lattice layers, controlling the barrier thickness and designing the dimensions of the graphene electrodes are all becoming more achievable. We have demonstrated that all of these will allow higher operating frequencies to be reached. An additional gate electrode can be added to make a field-effect transistor in which tunnelling can be controlled via the gate voltage.

Within this thesis, the effect of changing parameters on the current-voltage and current-time tunnelling characteristics of GRTDs has been quantified. For example, reducing the barrier width (a modest change to the structure of existing devices) increases the tunnel current, and thus raises the oscillation frequency by an order of magnitude. Adjusting the doping of the electrodes can enhance the frequency, and can be achieved by adsorbing molecules onto the surface of graphene. The effect of misalignment of the graphene electrodes was also considered and showed that, in devices

with aligned lattices, frequencies approaching 1 THz may be attainable. GaAsInAs/AlAs RTDs [18] with two layer-thick barriers have similar peak currents and voltages to the GRTD reported here. We therefore expect that the GRTD will produce similar EM emission power ($\sim$10 μW). Our results illustrate the potential of graphene tunnel structures in HF graphene electronics, and we predict that in future devices, higher frequencies can be obtained by altering the design of the device in order to minimise the parasitic reactance. We note the current work of [105] where 55 μW 1 THz was achieved in an InP-based RTD array [105] integrated with patch antennas, and the recent work of [106] in which 2 THz was reached.

By mounting the graphene/barrier/graphene layers on hBN, moiré patterns can be induced at small misalignment angles. This leads to supplementary Dirac points forming in the band structure. The energy at which these occur depends on the misalignment angle, which therefore offers control of not only the position of the non-linear region, but also the intensity of the dip in the density of states. Consequently, experiments to probe the band structure via tunnelling measurements could be performed. The effect of the moiré potential on the $I_b(V_b)$ characteristics of the GRTD was investigated, although for the parameters investigated the overall effect was negligible, some interesting features in small voltage probing were found. The inclusion of doping may allow more features from the chemical potential aligning with the density of states to become more prominent in the overall current.

Further work could include investigating different barrier, substrate and contact materials. Crystals with a slightly different lattice constant would lead to different superlattice wavelengths. In addition, the hBN barrier layers could be brought into alignment with the top or bottom graphene electrode to further investigate novel tunnelling between non-linear band structures. The scattering potential, V_S, can be modified by etching potentials on to the surface of the device, which would change the $I_b(V_b)$ characteristics. Devices consisting of bi- and tri-layer graphene could also be investigated, or novel arrangements of graphene and other crystals to form large superlattices.

Bibliography

[1] L. L. Chang, E. E. Mendez, and C. Tejedor, *Resonant Tunneling in Semiconductors: Physics and Applications* (Springer, 1990).

[2] E. R. Brown, T. C. L. G. Sollner, C. D. Parker, W. D. Goodhue, and C. L. Chen, *Appl. Phys. Lett.* **55**, 1777 (1989).

[3] K. S. Novoselov, V. I. Falko, L. Colombo, P. R. Gellert, M. G. Schwab, and K. Kim, *Nature* **490**, 192 (2012).

[4] F. Mandl, *Quantum Mechanics* (Wiley, 1992).

[5] S. M. Sze and K. K. Ng, *Physics of Semiconductor Devices* (Wiley, 2006).

[6] L. Esaki, *Phys. Rev.* **109**, 2, 603 (1958).

[7] B. K. Ridley, *Proc. Phys. Soc.* **82** 954 (1963).

[8] C. Hilsum, *Proc. IRE* **50**, 185 (1962).

[9] J. B. Gunn, *Solid State Commun.* **1**, 88 (1963).

[10] L. Esaki and R. Tsu, *IBM Journal of Research and Development* **14**, 61 (1970).

[11] R. F. Kazarinov and R. A. Suris, *Sov. Phys. Semicond. USSR* **5**, 707 (1971).

[12] L. L. Chang, L. Esaki and R. Tsu, *Appl. Phys. Lett.* **24**, 593 (1974).

[13] M. Asada, S.Suzuki, and N. Kishimoto, *Jpn. J. Appl. Phys.* **47**, 4375 (2008).

[14] S. Suzuki, M. Asada, A. Teranishi, H. Asugiyama, and H. Yokoyama, *Appl. Phys. Lett.* **97**, 242102 (2010).

[15] E. E. Vdovin, A. Levin, A. Patane, L. Eaves, P. C. Main, Yu. N. Khanin, Yu. V. Dubrovskii, M. Henini, and G. Hill, *Science* **290**(5489), 122 (2000).

[16] M. Feiginov, C. Sydlo, O. Cojocari, and P. Meissner *Appl. Phys. Lett.* **99**, 233506 (2011).

[17] M. Feiginov, H. Kanaya, S. Suzuki and M. Asada, *Appl. Phys. Lett.* **104**, 243509 (2014).

[18] S. Suzuki, M. Asada, A. Teranishi, H. Asugiyama, and H. Yokoyama, *Appl. Phys. Lett.* **97**, 242102 (2010).

[19] Y. Koyama, R. Sekiguchi, and T. Ouchi, *Appl. Phys. Express* **6**, 064102 (2013).

[20] A. Mishchenko, J. S. Tu, Y. Cao, R. V. Gorbachev, J. R. Wallbank, M. T. Greenaway, V. E. Morozov, S. V. Morozov, M. J. Zhu, S. L. Wong, F. Withers, C. R. Woods, Y-J. Kim, K. Watanabe, T. Taniguchi, E. E. Vdovin, O. Makarovsky, T. M. Fromhold, V. I. Fal'ko, A. K. Geim, L. Eaves, and K. S. Novoselov, *Nat. Nano.* **9**, 808 (2014).

[21] P. R. Wallace, *Phys. Rev.* **71** 662 (1947).

[22] J. W. McClure, *Phys. Rev.* **104**, 666 (1956).

[23] G. W. Semenoff, *Phys. Rev. Lett.* **53**, 2449 (1984).

[24] D. P. DiVencenzo and E. J. Mele, *Phys. Rev. B* **29**, 1685 (1984).

[25] K. S. Novoselov, A. K. Geim, S. V. Morozov, D. Jiang, Y. Zhang, S. V. Dubonos, I. V. Grigorieva, and A. A. Firsov, *Science* **306**, 666 (2004).

[26] K. S. Novoselov, D. Jiang, F. Schedin, T. J. Booth, V. V. Khotkevich, S. V. Morozov, and A. K. Geim, *Proceedings of the National Academy of Sciences of the United States of America* **102**, 10451 (2005).

[27] Y.-M. Lin, C. Dimitrakopoulos, K. A. Jenkins, D. B. Farmer, H.-Y. Chiu, A. Grill, and P. Avouris, *Science* **327**, 662 (2010).

[28] K. S. Kim, Y. Zhao, H. Jang, S. Y. Lee, J. M. Kim, K. S. Kim, J.-H. Ahn, P. Kim, J.-Y. Choi, and B. H. Hong, *Nature* **457**, 706 (2009).

[29] L. G. De Arco, Y. Zhang, C. W. Schlenker, K. Ryu, M. E. Thompson, C. Zhou, *ACS Nano.* **4**, 2865 (2010).

[30] N. Yang, J. Zhai, D. Wang, Y. Chen, and L. Jiang, *ACS Nano.* **4**, 887 (2010).

[31] A. Tzalenchuk, S. Lara-Avila, A. Kalaboukhov, S. Paolillo, M. Syvajarvi, R. Yakimova, O. Kazakova, T. J. B. M. Janssen, V. Fal'ko, and S. Kubatkin, *Nature Nanotechnol.* **5**, 186 (2010).

[32] T. J. B. M. Janssen, S. Rozhko, I. Antonov, A. Tzalenchuk, J. M. Williams, Z. Melhem, H. He, S. Lara-Avila, S. Kubatkin, and R. Yakimova, *2D Mater.* **2** 035015 (2015).

[33] K. S. Novoselov, Z. Jiang, Y. Zhang, S. V. Morozov, H. L. Stormer, U. Zeitler, J. C. Maan, G. S. Boebinger, P. Kim, and A. K. Geim, *Science* **315** (5817) 1379 (2007).

[34] B. Jeckelmann and B. Jeanneret, *Rep. Prog. Phys.* **64**, 1603 (2001).

[35] C. R. Dean, L. Wang, P. Maher, C. Forsythe, F. Ghahari, Y. Gao, J. Katoch, M. Ishigami, P. Moon, M. Koshino, T. Taniguchi, K. Watanabe, K. L. Shepard, J. Hone, and P. Kim, *Nature* **497**, 598 (2013).

[36] L. A. Ponomarenko, R. V. Gorbachev, G. L. Yu, D. C. Elias, R. Jalil, A. A. Patel, A. Mishchenko, A. S. Mayorov, C. R. Woods, J. R. Wallbank, M. Mucha-Kruczynski, B. A. Piot, M. Potemski, I. V. Grigorieva, K. S. Novoselov, F. Guinea, V. I. Fal'ko, and A. K. Geim, *Nature* **497**, 594 (2013).

[37] F. Withers, O. Del Pozo-Zamudio, A. Mishchenko, A. P. Rooney, A. Gholinia, K. Watanabe, T. Taniguchi, S. J. Haigh, A. K. Geim, A. I. Tartakovskii, and K. S. Novoselov, *Nature Mater.* **14**, 301 (2015).

[38] E. McCann, *Electronic properties of monolayer and bilayer graphene Graphene Nanoelectronics* (Berlin: Springer, 2012).

[39] R. Saito, M. S. Dresselhaus, and G. Dresselhaus, *Physical Properties of Carbon Nanotubes* (Imperial College Press, 1998).

[40] T. O. Wehling, K. S. Novoselov, S. V. Morozov, E. E. Vdovin, M. I. Katsnelson, A. K. Geim, and A. I. Lichtenstein, *Nano. Lett.* **8**(1), 173 (2008).

[41] F. D. M. Haldane, *Phys. Rev. Lett.* **61**, 2015 (1988).

[42] X. Xu, W. Yao, D. Xiao, and T. F. Heinz, *Nature Physics* **10**, 343 (2014).

[43] O. Klein, *Z. Phys.* **53**, 157 (1929).

[44] M. I. Katsnelson, K. S. Novoselov, and A. K. Geim, *Nat. Phys.* **2**, 620 (2006).

[45] A. F. Young and P. Kim, *Nat. Phys.* **5**, 222 (2009).

[46] C. R. Dean, A. F. Young, I. Meric, C. Lee, L. Wang, S. Sorgenfrei, K. Watanabe, T. Taniguchi, P. Kim, K. L. Shepard, and J. Hone, *Nature Nanotechnol.* **5**, 722 (2010).

[47] G. Fiori, A. Betti, S. Bruzzone, P. DAmico, G. Iannaccone, *Electron Devices Meeting (IEDM), 2011 IEEE International* DOI: 10.1109/IEDM.2011.6131533.

[48] X. Blase, A. Rubio, S. G. Louie, and M. L. Cohen, *Europhys. Lett.* **28** 51, 335 (1994).

[49] G. Giovannetti, P. A. Khomyakov, G. Brocks, P. J. Kelly, and J. van den Brink, *Phys. Rev. B* **76**, 073103 (2007).

[50] A. K. Geim and I. V. Grigorieva, *Nature* **499**, 419425 (2013).

[51] L. Britnell, R. V. Gorbachev, R. Jalil, B. D. Belle, F. Schedin, A. Mischenko, T. Georgiou, M. I. Katsnelson, L. Eaves, S. V. Morozov, N. M. R. Peres, J. Leist, A. K. Geim, K. S. Novoselov, and L. A. Ponomarenko, *Science* **335**, 947 (2012).

[52] L. Britnell, R.V. Gorbachev, A.K. Geim, L.A. Ponomarenko, A. Mishchenko, M.T. Greenaway, T.M. Fromhold, K.S. Novoselov, and L. Eaves, *Nat. Commun.* **4**, 1794 (2013).

[53] S. Kang, B. Fallahazad, L. Kayoung, H. Movva, K. Kyounghwan, C. M. Corbet, T. Taniguchi, K. Watanabe, L. Colombo, L. F. Register, E. Tutuc, and S. K. Banerjee, *IEEE Electron Device Lett.* **36**(4), 405 (2015).

[54] R.M. Feenstra, D. Jena, and G. Gu, *J. Appl. Phys.* **111**, 043711 (2012).

[55] T. Georgiou, R. Jalil, B. D. Belle, L. Britnell, R. V. Gorbachev, S. V. Morozov, Y. J. Kim, A. Gholinia, S. J. Haigh, O. Makarovsky, L. Eaves, L. A. Ponomarenko, A. K. Geim, K. S. Novoselov, and A. Mishchenko, *Nat. Nano.* **2**, 100 (2013).

[56] B. Fallahazad, K. Lee, S. Kang, J. Xue, S. Larentis, C. Corbet, K. Kim, H. C. P. Movva, T. Taniguchi, K. Watanabe, L. F. Register, S. K. Banerjee, and E. Tutuc, *Nano. Lett.* **15**, 428 (2015).

[57] L. Brey, *Phys. Rev. Appl.* **2**, 014003 (2014).

[58] F. T. Vasko, *Phys. Rev. B* **87**, 075424 (2013).

[59] P. Zhao, R. M. Feenstra, G. Gu, and D. Jena, *IEEE Trans. Electron Devices* **60**, 951 (2013).

[60] V. Ryzhii, A. A. Dubinov, V. Y. Aleshkin, M. Ryzhii and T. Otsuji, *Appl. Phys. Lett.* **103**, 163507 (2013).

[61] V. Ryzhii, A. Satou, T. Otsuji, M. Ryzhii, V. Mitin and M. S. Shur, *J. Phys. D: Appl. Phys.* **46** 315107 (2013).

[62] L. Britnell, R. V. Gorbachev, R. Jalil, B. D. Belle, F. Schedin, M. I. Katsnelson, L. Eaves, S. V. Morozov, A. S. Mayorov, N. M. R. Peres, A. H. Castro Neto, J. Leist, A. K. Geim, L. A. Ponomarenko, and K. S. Novoselov, *Nano. Lett.* **12**(3), 1707 (2012).

[63] J. Nilsson and S. Riedel, *Electric Circuits* (Prentice Hall, 2008).

[64] D. L. Nika and A. A. Balandin, *J. Phys.: Condens. Matter* **24** 233203 (2012).

[65] J. Bardeen, Phys. Rev. Lett. **6**, 57 (1961).

[66] J. Tersoff and D. R. Hamann, *Phys. Rev. B* **31**, 805 (1985).

[67] A. H. Castro Neto, F. Guinea, N. M. R. Peres, K. S. Novoselov, and A. K. Geim, *Rev. Mod. Phys.* **81**, 109 (2009).

[68] C. R. Woods, L. Britnell, A. Eckmann, R. S. Ma, J. C. Lu, H. M. Guo, X. Lin, G. L. Yu, Y. Cao, R. V. Gorbachev, A. V. Kretinin, J. Park, L. A. Ponomarenko, M. I. Katsnelson, Yu. N. Gornostyrev, K. Watanabe, T. Taniguchi, C. Casiraghi, H-J. Gao, A. K. Geim, and K. S. Novoselov, *Nat. Phys.* **10**, 451 (2014).

[69] A. Eckmann, J. Park, H. Yang, D. Elias, A. S. Mayorov, G. Yu, R. Jalil, K. S. Novoselov, R. V. Gorbachev, M. Lazzeri, A. K. Geim, and C. Casiraghi, *Nano. Lett.* **13**, 5242 (2013).

[70] E. J. Mele, *Phys. Rev. B* **81**, 161405, (2010).

[71] R. Bistritzer and A. H. MacDonald, *Phys. Rev. B* **81**(24), 245412 (2010).

[72] C. B. Duke, *Tunneling in Solids* (Academic, New York 1969).

[73] T. Roy, L. Liu, S. de la Barrera, B. Chakrabarti, Z. R. Hesabi, C. A. Joiner, R. M. Feenstra, G. Gu and E. M. Vogel, *Appl. Phys. Lett.* **104**, 123506 (2014);

[74] S. Luryi, *Appl. Phys. Lett*, **52**(6), 501 (1988).

[75] L. Chang, L. Esaki, and R. Tsu, *Appl. Phys. Lett.* **24**, 593 (1974).

[76] H. Mizuto and T. Tanoue, *The Physics and Applications of Resonant Tunnelling Diodes* (Cambridge University Press, 1996).

[77] Q. Li, E. H. Hwang, E. Rossi, and S. Das Sarma, *Phys. Rev. Lett.* **107**, 156601 (2011).

[78] C. Dean, A. F. Young, L. Wang, I. Meric, G-H. Lee, K. Watanabe, T. Taniguchi, K. Shepard, P. Kim, and J. Hone, *Solid State Comm.* **152**, 1275 (2012).

[79] L. A. Ponomarenko, A. K. Geim, A. A. Zhukov, R. Jalil, S. V. Morozov, K. S. Novoselov, I. V. Grigorieva, E. H. Hill, V. V. Cheianov, V. I. Falko, K. Watanabe, T. Taniguchi, and R. V. Gorbachev, *Nat. Phys.* **7**, 968 (2011).

[80] S. Adam, E. H. Hwang, E. Rossi, and S. Das Sarma, *Solid State Commun.* **149**(27), 1072 (2009).

[81] A. Das, S. Pisana, B. Chakraborty, S. Piscanec, S. K. Saha, U. V. Waghmare, K. S. Novoselov, H. R. Krishnamurthy, A. K. Geim, A. C. Ferrari, and A. K. Sood, *Nat. Nano.* **3**, 210 (2008).

[82] L. Hongtao, L. Yunqi, and Z. Daoben, *J. Mat. Chem.* **21**(10), 3253 (2011).

[83] N. Kharche and S. K. Nayak, *Nano. Lett.* **11** (12), 5274 (2011).

[84] Y. Xu and W. Y. Ching, *Phys. Rev. B* **44**, 7787 (1991).

[85] V. Ryzhii, A. Satou, T. Otsuji, M. Ryzhii, V. Mitin, and M. S. Shur, *Journal of Physics D: Appl. Physics* **46**(31), 315107 (2013).

[86] J. Faist, F. Capasso, D. L. Sivco; C. Sirtori, A. L. Hutchinson, and A. Y. Cho, *Science* **264** (5158), 553 (1994).

[87] E. R. Brown, J. R. Söderström, C. D. Parker, L. J. Mahoney, K. M. Molvar, and T. C. McGill, *Appl. Phys. Lett.* **58**, 2291 (1991).

[88] M. Asada, S. Suzuki, and N. Kishimoto, *Japanese Journal of Appl. Phys.* **47**, 6 (2008).

[89] K. Kim, A. Hsu, X. Jia, S. Kim, Y. Shi, M. Dresselhaus, T. Palacios, and J. Kong, *ACS Nano.* **6**(10), 8583 (2012).

[90] E. M. Purcell and D. J. Morin, *Electricity and Magnetism.* (Cambridge Univ. Press, 2013).

[91] M. E. Hines, *Bell System Technical Journal* **39**, 477 (1960).

[92] A. V. Kretinin, Y. Cao, J-S. Tu, G. L. Yu, R. Jalil, K. S. Novoselov, S. J. Haigh, A. Gholinia, A. Mishchenko, M. Lozada, T. Georgiou, C. R. Woods, F. Withers, P. Blake, G. Eda, A. Wirsig, C. Hucho, K. Watanabe, T. Taniguchi, A. K. Geim, and R. V. Gorbachev, *Nano. Lett.* **14**, 3270 (2014).

[93] K. I. Bolotin, K. J. Sikes, Z. Jiang, M. Klima, G. Fudenberg, J. Hone, P. Kim, H. L. Stormer, *Solid State Commun.* **146**, 351 (2008).

[94] K. Chen, X. Wan, J. Wen, W. Xie, Z. Kang, X. Zeng, H. Chen, and J. Xu, *ACS Nano.* **9**(10), 9868 (2015).

[95] J. R. Wallbank, A. A. Patel, M. Mucha-Kruczynski, A. K. Geim, and V. I. Fal'ko, *Phys. Rev. B* **87**, 245408 (2013).

[96] M. Yankowitz, J. Xue, D. Cormode, J. D. Sanchez-Yamagishi, K. Watanabe, T. Taniguchi, P. Jarillo-Herreo, P. Jacquod, and B. J. LeRoy, *Nat. Phys.* **8**, 382 (2012).

[97] M. Yankowitz, J. Xue, and B. J. LeRoy, *Journal of Physics: Condensed Matter* **26** (30), 303201 (2014).

[98] N. W. Ashcroft and N. D. Mermin, *Solid State Physics* (Brooks Cole, 1976).

[99] C-H. Park, L. Yang, Y-W. Son, M. L. Cohen, and S. G. Louie, *Nature Phys.* **4**, 213 (2008).

[100] C-H. Park, L. Yang, Y-W. Son, M. L. Cohen, and S. G. Louie, *Phys. Rev. Lett.* **101**, 126804 (2008).

[101] J. R. Wallbank, A. A. Patel, M. Mucha-Kruczyski, A. K. Geim, and V. I. Fal'ko, *Phys. Rev. B* **87**, 245408 (2013).

[102] J. R. Wallbank, M. Mucha-Kruczynski, X. Chen, and V. I. Fal'ko, *Annalen der Physik* **527**(5-6), 359 (2015).

[103] Y. Liu, G. Bian, T. Miller, and T.-C. Chiang *Phys. Rev. Letts.* **107**, 166803 (2011).

[104] M. T. Greenaway, E. E. Vdovin, A. Mishchenko, O. Makarovsky, A. Patané, J. R. Wallbank, Y. Cao, A. V. Kretinin, M. J. Zhu, S. V. Morozov, V. I. Fal'ko, K. S. Novoselov, A. K. Geim, T. M. Fromhold, and L. Eaves, *Nat. Phys.* **11**, 1057 (2015).

[105] K. Kasagi, N. Oshima, S. Suzuki, and M. Asada *IEICE TRANSACTIONS on Electronics* **98**(12) 1131 (2015).

[106] T. Maekawa, H. Kanaya, S. Suzuki, and M. Asada *IEICE Electronics Express* **8**(14) 1110 (2016).